

بِسْمِ اللَّهِ الرَّحْمَنِ الرَّحِيمِ

Investigation of Unsteady Stagnation point flow of nanofluids



By

Arif Ullah Khan

**Department of Mathematics
Quaid-i-Azam University
Islamabad, Pakistan
2018**

Investigation of Unsteady Stagnation point flow of nanofluids



By

Arif Ullah Khan

Supervised By

Prof. Dr. Sohail Nadeem

**Department of Mathematics
Quaid-i-Azam University
Islamabad, Pakistan
2018**

Investigation of Unsteady Stagnation point flow of nanofluids



By

Arif Ullah Khan

*A Dissertation Submitted in the Partial Fulfillment of
the requirements for the degree of*

DOCTOR OF PHILOSOPHY

IN

MATHEMATICS

Supervised By

Prof. Dr. Sohail Nadeem

**Department of Mathematics
Quaid-i-Azam University
Islamabad, Pakistan
2018**

Turnitin Originality Report

Investigation of Unsteady Stagnation point flow of nanofluids
From Theses (QAU theses)

by Arif Ullah Khan .



- Processed on 12-Sep-2018 08:28 PKT
- ID: 1000483359
- Word Count: 23971

Similarity Index

15%

Similarity by Source

Internet Sources:

10%

Publications:

11%

Student Papers:

3%

sources:

- 1 1% match (publications)
A. Borrelli, G. Giamtesio, M.C. Patria, N.C. Rosca, A.V. Rosca, I. Pop, "Buoyancy effects on the 3D MHD stagnation-point flow of a Newtonian fluid". Communications in Nonlinear Science and Numerical Simulation, 2017
- 2 1% match (Internet from 04-Dec-2015)
http://www16.us.archive.org/stream/nasa_techdoc_19930018537/19930018537_djvu.txt
- 3 < 1% match (publications)
Nadeem Abbas, S. Saleem, S. Nadeem, A.A. Alderremy, A.U. Khan, "On stagnation point flow of a micro polar nanofluid past a circular cylinder with velocity and thermal slip". Results in Physics, 2018
- 4 < 1% match (publications)
Y. Y. Lok, J. H. Merkin, I. Pop, "Mixed convection non-axisymmetric Homann stagnation-point flow". Journal of Fluid Mechanics, 2017
- 5 < 1% match (Internet from 29-Jul-2017)
<http://polen.itu.edu.tr/xmlui/bitstream/handle/11527/4743/2260.pdf?isAllowed=y&sequence=1>
- 6 < 1% match (publications)
Nadeem, S., Bushra Tahir, Fotini Labropulu, and Noreen Sher Akbar, "Unsteady Oscillatory Stagnation Point Flow of a Jeffrey Fluid". Journal of Aerospace Engineering, 2014.
- 7 < 1% match (student papers from 27-Jan-2015)
Submitted to Higher Education Commission Pakistan on 2015-01-27
- 8 < 1% match (Internet from 29-Jan-2016) .
<http://eprints.unife.it/802/1/Giamtesio.pdf>
- 9 < 1% match (Internet from 11-Aug-2018)
<https://ourspace.uregina.ca/handle/10294/3625>
- 10 < 1% match (publications)
Weidman, P. D., "Non-axisymmetric Homann stagnation-point flows". Journal of Fluid Mechanics, 2012.
- 11 < 1% match (Internet from 19-May-2018)
<https://d-nb.info/1149517964/34>
- 12 < 1% match (student papers from 26-Sep-2016)
Submitted to Higher Education Commission Pakistan on 2016-09-26
- 13 < 1% match ()
<http://www.tarotconway.co.uk/music/quin3tr.mus>

Focal Person (Turnitin)
Quaid-i-Azam University
Islamabad

Author's Declaration

I Arif Ullah Khan hereby state that my Ph.D. thesis titled Investigation of Unsteady Stagnation point flow of nanofluids is my own work and has not been submitted previously by me for taking any degree from the Quaid-i-Azam University Islamabad, Pakistan or anywhere else in the country/world.

At any time if my statement is found to be incorrect even after my graduate the university has the right to withdraw my PhD degree.

Name of Student:  Arif Ullah Khan

Date: 03-09-2018

Plagiarism Undertaking

I solemnly declare that research work presented in the thesis titled "Investigation of Unsteady Stagnation point flow of nanofluids" is solely my research work with no significant contribution from any other person. Small contribution/help wherever taken has been duly acknowledged and that complete thesis has been written by me.

I understand the zero tolerance policy of the HEC and Quaid-i-Azam University towards plagiarism. Therefore, I as an Author of the above titled thesis declare that no portion of my thesis has been plagiarized and any material used as reference is properly referred/cited.

I undertake that if I am found guilty of any formal plagiarism in the above titled thesis even afterward of PhD degree, the University reserves the rights to withdraw/revoke my PhD degree and that HEC and the University has the right to publish my name on the HEC/University Website on which names of students are placed who submitted plagiarized thesis.

Student/Author Signature: _____

Name: _____

Arif Ullah Khan

Investigation of Unsteady Stagnation point flow of nanofluids

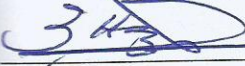
By

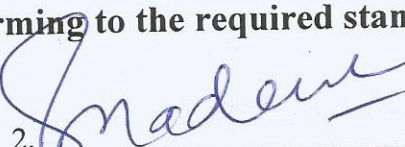
Arif Ullah Khan


CERTIFICATE


A DISSERTATION SUBMITTED IN THE PARTIAL FULFILLMENT OF THE
REQUIREMENTS FOR THE DEGREE OF THE DOCTOR OF
PHILOSOPHY

We accept this dissertation as conforming to the required standard

1. 
Prof. Dr. Tasawar Hayat
(Chairman)

2. 
Prof. Dr. Sohail Nadeem
(Supervisor)

3. 
Dr. Khalid Hanif
Associate Professor
Post-graduate Federal Govt.
College (Men), H-8,
Islamabad.
(External Examiner)

4. 
Dr. Tanvir Akbar Kiani
Assistant Professor
Department of Mathematics
COMSATS, Park Road,
Chak Shahzad, Islamabad.
(External Examiner)

Department of Mathematics
Quaid-i-Azam University
Islamabad, Pakistan
2018

DEPARTMENT OF MATHEMATICS
Quaid-i-Azam University
Islamabad

Certificate of Approval

This is to certify that the research work presented in this thesis entitled **Investigation of Unsteady Stagnation point flow of nanofluids** was conducted by Mr. **Arif Ullah Khan** under the kind supervision of **Prof. Dr. Sohail Nadeem**. No part of this thesis has been submitted anywhere else for any other degree. This thesis is submitted to the Department of Mathematics, Quaid-i-Azam University, Islamabad in partial fulfillment of the requirements for the degree of Doctor of Philosophy in field of Mathematics from Department of Mathematics, Quaid-i-Azam University Islamabad, Pakistan.

Student Name: **Arif Ullah Khan**

Signature: 


External committee:

a) **External Examiner 1:**

Name: **Dr. Khalid Hanif**

Designation: Associate Professor

Office Address: Post-graduate Federal Govt. College (Men), H-8, Islamabad.

Signature: 

b) **External Examiner 2:**

Name: **Dr. Tanvir Akbar Kiani**

Designation: Associate Professor

Office Address: Department of Mathematics, COMSATS, Park Road, Chak Shahzad, Islamabad.

Signature: 

c) **Internal Examiner**

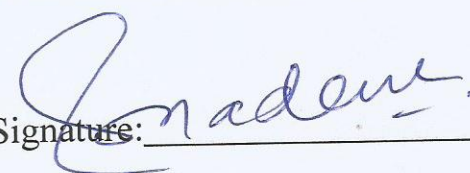
Name: **Dr. Sohail Nadeem**

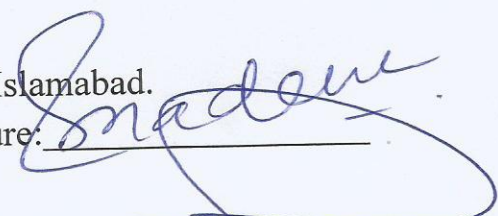
Designation: Professor

Office Address: Department of Mathematics, QAU Islamabad.

Supervisor Name:

Prof. Dr. Sohail Nadeem

Signature: 

Signature: 

Name of Dean/ HOD

Prof. Dr. Tasawar Hayat

Signature: 

Preface

This study is motivated to understand the time dependent stagnation point flow of nanofluids. Basically, stagnation flow occurs due to the impact of fluid on the solid objects. Near the stagnation point, the flow exhibits the highest heat transfer rate, pressure (static pressure), and mass deposition. According to Bernoulli's equation when fluid velocity comes to zero it experiences a maximum pressure. It is because kinetic energy of the fluid is converted into pressure known as stagnation pressure (static pressure). Stagnation flows of nanofluids are significant in transpiration cooling (e.g. cooling of a nuclear reactor), reduce friction, and many other industrial and hydrodynamic activities. In this thesis we study the unsteady stagnation point flow of a Newtonian and micropolar nanofluids by considering different types of base fluids and different nanoparticles in two as well as in three dimensions. Also, we studied three types of unsteady stagnation point flow of incompressible nanofluids: plane orthogonal, plane oblique and three dimensional non-axisymmetric by considering different geometries such as two-dimensional horizontal plate, two-dimensional curved shrinking surface and three-dimensional vertical surface. All of the above mention physical problems are transformed into mathematical model using the governing equations of the fluid flow. These equations are then transformed into the set of nonlinear ordinary differential equations. The solutions of transformed equations are obtained via homotopy analysis method, midpoint method with Richardson extrapolation enhancement, shooting mechanism with fifth order R-K Fehlberg technique, bvp4c package in MATLAB, some analytical and perturbation solutions. In order to check the accuracy of the solution methods, comparison is made with the previous results. Also, different observations are made using graph and tables for all the problems under consideration.

Table of Content

List of Figures	i
List of Tables	vi
Nomenclature	viii
0 Introduction	1
1 A comparative study of different nanofluid models for the oscillatory stagnation point flow	9
1.1 Introduction	9
1.2 Mathematical formulation for two-phase model:	9
1.2.1 Fixed frame of reference:	10
1.2.2 Moving frame of reference:	12
1.2.3 Energy Equation:	14
1.3 Mathematical formulation for Buongiorno model:	15
1.4 Homotopy Analysis method:	17
1.5 Results and Discussion:	18
1.6 Conclusion	28
2 Phase flow study of MHD nanofluid with slip effects on oscillatory oblique stagnation point flow in view of inclined magnetic field	29
2.1 Introduction	29
2.2 Problem description and governing equations	30
2.3 Solution procedure	36
2.4 Results and Discussion	37

2.5	Conclusion	51
3	Impact of external magnetic field and metallic particles on oscillatory oblique stagnation point flow of a micropolar fluid	52
3.1	Introduction	52
3.2	Problem description and governing equations:	53
3.3	Solution procedure:.....	59
3.4	Results and Discussion:	61
3.5	Conclusion	76
4	Model based study of SWCNT and MWCNT thermal conductivities effect on the heat transfer due to the oscillating wall conditions.....	77
4.1	Introduction	77
4.2	Problem description and governing equations:	78
4.2.1	Hamilton and Crosser model [59]:	80
4.2.2	Yamada and Ota model [60]:	81
4.2.3	Xue model [62]:.....	81
4.3	Solution procedure:.....	82
4.4	Results and Discussion:	84
4.5	Conclusion	97
5	Unsteady stagnation point flow of viscous nanofluids over the curved shrinking sheet: Existence of multiple solution	99
5.1	Introduction	99
5.2	Problem description and governing equations:	100

5.2.1	Steady-state case.....	101
5.3	Stability analysis.....	103
5.4	Results and discussion.....	106
5.5	Conclusion.....	119
6	Analysis of unsteady non-axisymmetric Homann stagnation point flow of nanofluid and possible existence of multiple solutions	121
6.1	Introduction.....	121
6.2	Problem formulation.....	122
6.2.1	The flow of an inviscid fluid.....	123
6.2.2	Newtonian nanofluids: analysis of the flow.....	124
6.3	Results.....	129
6.3.1	Forced convection, $\lambda = 0$	129
6.3.2	Numerical results.....	131
6.3.3	Free convection limit, λ large.....	139
6.3.4	Asymptotic for large γ	141
6.4	Conclusion.....	144
7	Bibliography.....	146

List of Figures

Fig. 1. 1. Normal component of velocity profile $f'(y)$ against M and φ	20
Fig. 1. 2. Steady part of shear velocity $g_0'(y)$ against M and φ	20
Fig. 1. 3. Temporal parts of shear velocity in fixed frame $g_1'(y)$ and moving frame $h'(y)$ against M and φ	21
Fig. 1. 4. Time dependent flow $g_y(y, t)$ at different locations from the surface when $\Omega = 1, \gamma = 1, M = 0.5, \varepsilon = 0.2$. (a) fixed frame of reference (b) moving frame of reference.....	21
Fig. 1. 5. Streamlines pattern when $\Omega = 1, M = 0.5, t = \pi 2, \varepsilon = 0.2$ (a) fixed frame of reference (b) moving frame of reference.	22
Fig. 1. 6. Influence of concentration and temperature profiles for different values of the involving parameters.	23
Fig. 1. 7. Comparison of two-phase model and Buongiorno model against Pr when $\Omega = 1, M = 0.5, t = \pi 2, \varepsilon = 0.2$	24
Fig. 1. 8. Variation of skin friction coefficient (a) fixed frame of reference (b) moving frame of reference.....	24
Fig. 1. 9. Variation of Nusselt number (a) Nt, Nb and φ (b) Ω (c) Pr	25
Fig. 1. 10. Sherwood number for different value of Nt and Nb	26
Fig. 2. 1. Geometry of the problem	29
Fig. 2. 2. $f(y), f'(y), f''(y)$ when $M = 2, N1 = 0.0, \varphi = 0.0$,.....	40
Fig. 2. 3. $g_0(y), g_0'(y)$ for different $\mathbb{B} - \mathbb{A}$ when $M = 2, N1 = 0.0, \varphi = 0.0$	40
Fig. 2. 4. Influence of $f'(y)$, (a) $\varphi = 0.0, N1 = 0.0$ and (b) $M = 0, \varphi = 0.0$	41
Fig. 2. 5. Influence of $g_0(y)$ and $g_0'(y)$ (a)-(b) $\varphi = 0.0, N1 = 0.0$ and (c)-(d) $\varphi = 0.0, M = 0.0$	42

Fig. 2. 6. Time dependent flow $u(y, t)$ at different locations from the surface when $\varphi = 0.1, N1 = 0.0, M = 1.0, \varepsilon = 0.2, \Omega = 0.2, \mathbb{B} - \mathbb{A} = -\mathbb{A}, x = 1$.	43
Fig. 2. 7. Variation of $\theta(y, t)$ (a) $\varphi = 0.1, N2 = 0.0, N1 = 0.5, \varepsilon = 0.0$ and (b) $\varphi = 0.1, M = 2.0, N1 = 0.5, \varepsilon = 0.0$.	43
Fig. 2.8. Streamlines pattern for $Cu - Water$ nanofluid when $t = 0, b/a = 1, \Omega = 0.5, N1 = 0.5, \varepsilon = 0.2$ for $\mathbb{B} - \mathbb{A} = -5\mathbb{A}, 0, 5\mathbb{A}$ respectively. (a), (b), (c) for $M = 1$ and (d), (e), (f) for $M = 5$.	44
Fig. 2. 9. Bar graph comparison of various nanoparticles.	45
Fig. 3. 1. Flow description of the problem.	52
Fig. 3. 2. $f(y), f'(y), f''(y)$ when $M = 10 - 7, \varphi = 0.0, K = 0.0$	63
Fig. 3. 3. $Fy, F'y$ when $M = 10 - 7, \varphi = 0.0, K = 1.0$.	63
Fig. 3. 4. Plots showing $f'y$ when $M = 10 - 7$ (a) $\varphi = 0.0, n = 0, M = 10 - 7,$ (b) $n = 0.1, K = 0.0$ and (c) $K = 0, \varphi = 0.0$ (d) $n = 0, K = 0, \varphi = 0.1$.	64
Fig. 3. 5. Influence of $g_0y,$ (a) for various M when $\varphi = 0.0, K = 0.0$ and (b) for various n when $M = 10 - 7, \varphi = 0.0, K = 0$.	65
Fig. 3. 6. Time dependent flow $u(y, t)$ at different locations from the surface when $Cu - Water, \varphi = 0.1, K = 0.0, M = 10 - 7, \varepsilon = 0.2, \Omega = 0.2, \mathbb{B} - \mathbb{A} = -\mathbb{A}, x = 1$.	65
Fig. 3. 7. Influence of $\theta y, t$ for various parameters when (a) $\varphi = 0.0, K = 0.0$ and (b) $M = 10 - 7, K = 0.0$.	66
Fig. 3. 8. Time dependent flow $\theta(y, t)$ at different locations from the surface when $Cu - Water, \varphi = 0.1, K = 0.0, M = 10 - 7, \varepsilon = 0.2, \Omega = 0.2, x = 1$.	66
Fig. 3. 9. Shows the streamlines for $Cu - Water$ nanofluid when $ba = 1, M = 10 - 7, K = 1, \Omega = 0.5, \varepsilon = 0.2, t = \pi$. (a) $\mathbb{B} - \mathbb{A} = -5 - \mathbb{A}$, (b) $\mathbb{B} - \mathbb{A} = 0$, (c) $\mathbb{B} - \mathbb{A} = 5 - \mathbb{A}$.	67

Fig. 3. 10. Shows the streamlines for <i>Cu – Water</i> nanofluid when $ba = 1, \mathbb{B} - \mathbb{A} = -5 - \mathbb{A}, K = 1, \Omega = 0.5, \varepsilon = 0.2, t = \pi$. (a) $M = 10 - 7$, (b) $M = 10 - 6$, (c) $M = 10 - 5$	67
Fig. 3. 11. Shows the streamlines of <i>Cu – Water</i> nanofluid when $ba = 1, \mathbb{B} - \mathbb{A} = -5 - \mathbb{A}, K = 1, \Omega = 0.5, \varepsilon = 0.2, t = 0$. (a) $t = 0$, (b) $t = \pi/2$, (c) $t = \pi$, (d) $t = 3\pi/2$	68
Fig. 3. 12. Bar graph comparison of two nanoparticles concentrations 5%, 15% and 20% respectively.....	69
Fig. 4. 1. Functional Diagram.....	77
Fig. 4. 2. Time dependent flow of the velocity field $u(y, t)$ at different locations from the wall. The time period is $t \in [0, 10\pi]$ for (a) <i>SWCNT – Water</i> . (b) <i>MWCNT – Water</i>	87
Fig. 4. 3. streamlines pattern for <i>SWCNT – Water</i> nanofluid. (a) $\mathbb{B} - \mathbb{A} = -6\mathbb{A}$, (b) $\mathbb{B} - \mathbb{A} = 0$, (c) $\mathbb{B} - \mathbb{A} = 4\mathbb{A}$	87
Fig. 4. 4. Streamlines pattern for nanofluids when $\mathbb{B} - \mathbb{A} = -2\mathbb{A}$. (a) <i>SWCNT – Water</i> , (b) <i>SWCNT – Engine Oil</i> , (c) <i>SWCNT – Ethylene Glycol</i> (d) <i>MWCNT – Water</i> , (e) <i>MWCNT – Engine Oil</i> , (f) <i>MWCNT – Ethylene Glycol</i>	88
Fig. 4. 5. Streamlines of <i>SWCNT – Water</i> nanofluid when $\mathbb{B} - \mathbb{A} = 0$. (a) $t = 0$, (b) $t = \pi/2$, (c) $t = \pi$ (d) $t = 3\pi/2$	89
Fig. 4. 6. Variation of isotherms for different nanofluid models, (a) <i>SWCNT</i> , Hamilton & Crosser model, (b) <i>SWCNT</i> , Xue model, (c) <i>SWCNT</i> , Yamada & Otta model, (d) <i>MWCNT</i> , Hamilton & Crosser model, (e) <i>MWCNT</i> , Xue model, (f) <i>MWCNT</i> , Yamada & Otta.....	90
Fig. 4. 7. Shows the skin friction coefficient vs time for different value of <i>SWCNT – Water</i> nanofluid, (a) $\mathbb{B} - \mathbb{A} = -5\mathbb{A}$, (b) $\mathbb{B} - \mathbb{A} = \mathbb{A}$, (c) $\mathbb{B} - \mathbb{A} = 5\mathbb{A}$. Solid lines for <i>MWCNT</i> and dotted lines for <i>SWCNT</i>	91

Fig. 4. 8. Shows the Nusselt number vs time for, (a) Ethylene Glycol, (b) Engine Oil, when $\Omega = 0.5, \varepsilon = 0.2$. <i>SWCNT</i> as nanoparticles.	92
Fig. 4. 9. Comparison of different thermal conductivities models for CNT's nanofluids. (a) <i>SWCNT</i> -Water nanofluid, (b) <i>MWCNT</i> -Water nanofluid.	92
Fig. 4. 10. Bar graph comparison of various models for <i>SWCNTs</i> -water nanofluids when $t = \pi/2$	93
Fig. 5. 1. Geometry of the surfaces (a) Curved surface (b) Boundary layer shrinking surface.	99
Fig. 5. 2. Plot showing the behaviour of $f'(r)$ & $f''(r)$ with respect to β	109
Fig. 5. 3. Plot showing the behaviour of $f'(r)$ & $f''(r)$ with respect to φ	109
Fig. 5. 4. Plot showing the behaviour of $f'(r)$ & $f''(r)$ with respect to S	110
Fig. 5. 5. Plot showing the behaviour of $\theta(r)$ with respect to Ω & S	110
Fig. 5. 6. Variation of C_f with respect to β for several values of S	111
Fig. 5. 7. Variation of C_f with respect to β for several values of Ω	111
Fig. 5. 8. Variation of C_f with respect to β for several values of φ	112
Fig. 5. 9. Variation of C_f with respect to Ω for several values of S	112
Fig. 5. 10. Variation of C_f with respect to K for several values of β	113
Fig. 5. 11. Variation of Nu with respect to β for several values of φ	113
Fig. 5. 12. Variation of Nu with respect to Ω for several values of S	114
Fig. 5. 13. Variation of Nu with respect to K for several values of β	114
Fig. 5. 14. Stream lines pateren for several values of β when $S = 2, K = 50, \varphi = 0.2, \Omega = -2$	115
Fig. 5. 15. Isotherms for several values of K when $S = 2, \beta = -1.5, \varphi = 0.2, \Omega = -2, Pr = 6.2$	116

Fig. 6. 1. Forced convection: Plots (a) $f''(0)$ and (b) $g''(0)$ against γ for different ω obtained from the numerical integration of (6.34)-(6.36).....	131
Fig. 6. 2. Plots (a) $f''(0)$, (b) $g''(0)$ and (c) $-\theta'(0)$ against λ for different γ obtained from the numerical integration of (6.22)-(6.25).....	133
Fig. 6. 3. Critical values: a plot of λc against γ	134
Fig. 6. 4. Plots (a) $f''(0)$, (b) $g''(0)$ and $-\theta'(0)$ against λ for different ω obtained from the numerical integration of (6.22)-(6.25).....	135
Fig. 6. 5. Critical values: a plot of λc against ω	136
Fig. 6. 6. Plots (a) $f''(0)$, (b) $g''(0)$ and $-\theta'(0)$ against λ for different φ obtained from the numerical integration of (6.22)-(6.25).....	137
Fig. 6. 7. Variation of the displacement thickness A, B and C with γ when $\varphi = 0.2, \lambda = -2, \omega = -0.5, M = 10^{-7}$, obtained from (6.26)-(6.27).....	138

List of Tables

Table. 1. 1. Effective thermophysical quantities of nanofluids [72]	26
Table. 1. 2. Thermophysical properties of nanoparticles and base fluids [72].	27
Table. 1. 3. Validation of results for $f''(0)$	27
Table. 2. 1. Validation of results for $f''(0)$ when $\varphi = 0$ and $N_1 = 0$	46
Table. 2. 2. Validation of results for $g_0'(0)$ when $\varphi = 0$ and $N_1 = 0$	46
Table. 2. 3. $f''(0)$ and \mathbb{A} for different values N_1, M, φ and nanoparticles.	47
Table. 2. 4. $g_0'(0)$ and $\mathbb{B} - \mathbb{A}$ for different values of N_1, φ, M and nanoparticles.....	47
Table. 2. 5(a). Numerical values of $-\phi_0'(0), \phi_2'(0)$ and $\phi_4'(0)$	49
Table. 2. 6(a). $-\theta_0'(0), \theta_{12}'(0)$ and $\theta_{14}'(0)$ when $N_1 = 0.5$	50
Table. 3. 1. Validation of results for $f''(0)$ when $\varphi = 0$ and $K = 0$	70
Table. 3. 2. Validation of results for $g_0'(0)$ when $\varphi = 0$ and $K = 0$	70
Table. 3. 3(a). Numerical value of \mathbb{A} and $f''(0)$	71
Table. 3. 4(a). Numerical value of $g_0'(0)$	72
Table. 3. 5(a). Numerical value of $-\Phi_0'(0), \Phi_2'(0)$ and $\Phi_4'(0)$	74
Table. 3. 6(a). Numerical value of $-\theta_0'(0), \Theta_{12}'(0)$ and $\Theta_{14}'(0)$	75
Table. 4. 1. Validation of results for $f''(0)$	94
Table. 4. 2. Validation of results for $g_0'(0)$	94
Table. 4. 3. Skin friction variation when $\varepsilon = 0.5, \Omega = 0.5, t = 0, \mathbb{B} - \mathbb{A} = -\mathbb{A}$	95
Table. 4. 4 Numerical values of \mathbb{A} when $\varepsilon = 0.5, \Omega = 0.5, t = 0, \mathbb{B} - \mathbb{A} = -\mathbb{A}$	95

Table. 4. 5. Numerical values of Nusselt number when water is considered as a base fluid and $\varepsilon = 0.5, \Omega = 0.5, t = 0$	96
Table. 4. 6. Numerical values of Nusselt number when Ethylene Glycol is considered as a base fluid and $\varepsilon = 0.5, \Omega = 0.5, t = 0$	96
Table. 4. 7. Numerical values of Nusselt number when Engine Oil is considered as a base fluid and $\varepsilon = 0.5, \Omega = 0.5, t = 0$	97
Table. 5. 1. Numerical Values of C_f with $K = \infty, S = 0$ and $\varphi = 0$ (regular fluid), Results in parenthesis () are the second (lower branch) solutions.	117
Table. 5. 2. Comparison of eigenvalues α for different β when $S = 0, \varphi = 0.0, K = \infty, \Omega = 0$	118
Table. 5. 3. Smallest eigenvalues α at selected values of S and β when $\varphi = 0.2, K = 200, \Omega = -2$	118
Table. 6. 1. Numerical values of physical parameters obtained from Eqs. (6.61)-(6.64) when $\varphi = 0.2$	142

Nomenclature

Dimensional	
\bar{t}	Time coordinate [T]
$\bar{x}, \bar{y}, \bar{z}$	Spatial coordinates [L]
$\bar{u}, \bar{v}, \bar{w}$	velocity components [L/T]
\bar{p}	Pressure field [ML/T ²]
$\bar{\psi}$	Stream function [L ² /T]
$\bar{f}(\bar{y})$	Normal component of the flow
$\bar{g}(\bar{t}, \bar{y})$	Shear component of flow in fixed frame of reference
$\bar{h}(\bar{t}, \bar{y})$	Shear component of flow in moving frame of reference
\bar{V}	Velocity field
T	Temperature field
C	Concentration profile
ρ_{nf}	Density of nanofluids
ρ_f	Density of base fluids
ρ_s	Density of solid fraction
μ_{nf}	Dynamic viscosity of nanofluids
μ_f	Dynamic viscosity of base fluids
μ_s	Dynamic viscosity of solid fraction
ν_{nf}	Kinematic viscosity of nanofluids
ν_f	Kinematic viscosity of base fluids
ν_s	Kinematic viscosity of solid fraction
k_{nf}	Thermal conductivity of nanofluids
k_f	Thermal conductivity of base fluids
k_s	Thermal conductivity of solid fraction
$(\rho C_p)_{nf}$	Heat capacity of nanofluids
$(\rho C_p)_f$	Heat capacity of base fluids
$(\rho C_p)_s$	Heat capacity of solid fraction

α_{nf}	Thermal diffusivity of nanofluids
α_f	Thermal diffusivity of base fluids
α_s	Thermal diffusivity of solid fraction
σ_{nf}	Electrical conductivity of nanofluids
σ_f	Electrical conductivity of base fluids
σ_s	Electrical conductivity of solid fraction
a, b	Free stream parameter [1/T]
U	Waves speed amplitude [L/T]
ω	Frequency of oscillation [1/T]
B_0	strength of magnetic field
C_f	Skin friction coefficient
Nu	Nusselts Number
Sh	Sherwood number
$\bar{\mathbf{E}}$	Electric field
$\bar{\mathbf{H}}$	Magnetic field
A, B	Boundary layer control parameters [L]
T_w	Reference temperature
T_∞	Ambient temperature
\bar{N}	Angular momentum
$\bar{F}(\bar{y})$	Normal component of angular momentum
$\bar{G}(\bar{y}, \bar{t})$	Shear component of angular momentum
κ	Material parameter of micropolar fluid
j	Micro-inertia
\bar{r}, \bar{s}	Radial and Arc-length coordinates [L]
R	Radius of curvature [L]
Non-dimensional	
t	Time coordinate
x, y, z	Spatial coordinates

u, v, w	velocity components
p	Pressure field
ψ	Stream function
$f(y)$	Normal component of the flow
$g(t, y)$	Shear component of flow in fixed frame of reference
$h(t, y)$	Shear component of flow in moving frame of reference
\mathbf{V}	Velocity field
$g_0(y)$	Steady part of shear flow
$g_1(y)$	Temporal part of shear flow in fixed frame of reference
$h(y)$	Temporal part of shear flow in moving frame of reference
γ	Free stream parameter
Ω	Frequency (Unsteady parameter)
M	Hartmann Number
ε	Amplitude
$\theta(y, t)$	Temperature profile
$\theta_0(y)$	Steady part of temperature profile
$\theta_1(y)$	Temporal part of temperature profile
$\phi(t, y)$	Concentration profile
$\phi_0(y)$	Steady part of concentration profile
$\phi_1(y)$	Temporal part of concentration profile
Pr	Prandtl number
Nt	Thermophoresis parameter
Nb	Brownian motion parameter
Sc	Schmidt number
A, B	Boundary layer control parameter
$Re_{\bar{x}}$	Reynold number
$F(y)$	Normal component of angular momentum
$G(y, t)$	Shear component of angular momentum

$G_0(y)$	Steady part of Shear angular momentum
$G_1(y)$	Temporal part of Shear angular momentum
K	Material parameter of micropolar fluid
S	Mass flux parameter
β	Stretching/ Shrinking parameter
r, s	Radial and Arc-length coordinates
φ	Nanoparticle volume fraction

Chapter # 0

Introduction

Stagnation flow occurs due to the impact of fluid on the solid objects. Near the stagnation point, the flow exhibits the highest heat transfer rate, pressure (static pressure), and mass deposition. According to Bernoulli's equation when fluid velocity comes to zero it experiences a maximum pressure. It is because kinetic energy of the fluid is converted into pressure and is known as stagnation pressure (static pressure). Stagnation flows are significant in transpiration cooling (e.g. cooling of a nuclear reactor), reduce friction, and many other industrial and hydrodynamic activities. The application of stagnation point flows in analytical chemistry and life sciences has been seen in the literature presented by [1]. Hiemenz [2] was the first who studied the flow in the region of stagnation point. He begins with a qualitative description of the flow phenomena observed in a fluid of low friction over an obstacle. In the mathematical treatment of this flow, in the boundary layer, Hiemenz start from the Navier-Stokes system and presented a curvilinear coordinate system adjusted to the problem by applying the boundary layer approximation, Hiemenz got the same flow problem as found for the boundary layer along a fixed straight wall. It is exciting to take note of that the curvature of the coordinates has no impact on the procedures in the boundary layer. Hiemenz found the series solution for this problem and from the first order approximation, he used the similarity transformation and found the third order ordinary differential equation. The asymptotic forms for large $y \rightarrow \infty$ as $f \sim y - 0.6479$, $\delta^* \sim 0.6479\delta$, where δ^* is a boundary layer thickness. Hiemenz compare the computational results with the experimental one and found that the last outcome is a quantitatively very palatable understanding of experimental perception and numerical computation. Pohlhausen (*loc. Cit. as given in [3]*) attacks Hiemenz result for the point of separation as being obtained from an insufficient number of terms of a slowly converging series, as all terms of higher power than the fifth in x were neglected. For this purpose, in 1934, Howarth [3] discussed the Hiemenz flow and solved it with nine different method in which some are

- i. Blasius method
- ii. Karman-Pohlhausen method

- iii. Bairstow and Green method
- iv. Falkner-Skan's method
- v. Thomas second method.

After these analysis, Howarth found that this attack was, to some extent, unjustified. Howarth was shown that Hiemenz's results for the position of the point of separation hold good to, within, two degrees. Later on, in 1936, Homann [4] found the equation for the axisymmetric stagnation point flow and compare the computation with the experimental data. Howarth [5], in 1951, proposed the equation for the non-axisymmetric by using the equations of his another paper [6]. He used the similarity variables and obtained a pair of simultaneous ordinary third-order differential equations containing a single parameter $c = b/a$. He restricted the range for this parameter as $0 \leq c \leq 1$, where $c = 0$ corresponding to two-dimensional flow (i.e. Hiemenz flow) and $c = 1$ corresponding to the axial flow past a body of revolution (i.e. Homann flow) and found the numerical results. In 1956, Root [7] extend the work of Hiemenz and discussed the orthogonal stagnation point flow over a plate which perform a harmonic oscillation in its own plane. He used the similarity solutions which is the combination of orthogonal flow (Hiemenz flow) and temporal part of flow (g -flow) where he got the coupled equations of Hiemenz function and g -flow. Since f was found by Hiemenz [2], so Root took f as a known function and find the closed form solution for the **steady part** of g -flow and show that the corresponding shearing stress at the wall depends upon Hiemenz function only. The inviscid stream function for the oblique stagnation point flow, also known as non-orthogonal stagnation point flow, was discussed for the very first time by Stuart [8] in 1959. He just added a constant vorticity ξ_0 to the Hiemenz orthogonal flow. Stuart used the similarity solution which is the combination of orthogonal flow (Hiemenz flow) and shear flow and got a system of coupled ordinary differential equations in which the Hiemenz function was independent of shear flow but shear flow depends upon Hiemenz function. Like Root's, Stuart assume f as a known function (Hiemenz's function) and find the analytical solution for the shear flow (g -flow). In 1951, Howarth [5] pointed out that the solution for $f'(y)$ and $g'(y)$ for $c < 0$ may be found by using the symmetry

$$g(y, -c) = g(y, c), f(y, -c) = f(y, c)$$

but later-on, in 1964, Davey [9] stated that “these equations are incorrect since they do not satisfy the boundary conditions at infinity. Thus, solutions with $c < 0$ can't not be found from Howarth [5] results”. He suggested that the solution is possible for $c < 0$ when one take the velocity component normal to the surface near the stagnation point as $\{-a(1 + c)\bar{z}\}$ which is negative when $c > -1$, and he found that, the case $c < -1$ would correspond to saddle point of separation (but the equations can't be solved by Davey), whereas Howarth discussed only the nodal point of attachment. Furthermore, he proved that “ $g - flow$ has no solution which satisfy $g'(y) \rightarrow 1$ as $y \rightarrow 1$ when $c < -1$ ”. In follow-on work, Rosenhead [10], Davey and Schofield [11], Libby [12], Schofield and Davey [13] reported dual solutions of Howarth's equations at selected values of c . In 1967, Libby [14] extend the work of Homann by studying the stagnation point flow with large rates of injection. This flow is also known as a well-known “Homann-Libby flow”. Matunnobu [15,16] extend the Homann stagnation point flow and discussed the temporal variation of wall shear stress near the stagnation point. Tamada [17] and Dorrepaal [18] extended the orthogonal stagnation point flow (Hiemenz flow) to non-orthogonal stagnation point flow and found the exact solution of the Navier-Stokes equation. Recently, Weidman [19] found a new non-axisymmetric Homann flow by superposed an outer irrotational flow $\bar{u} = b\bar{y}$, $\bar{v} = b\bar{x}$ on to the Homann potential flow $\bar{u} = a\bar{x}$, $\bar{v} = a\bar{y}$, $\bar{w} = -2a\bar{z}$. In this flow, the non-dimensional Navier–Stokes equations depends on a single free stream parameter $\gamma = b/a$ which is the ratio of shear rate and strain rate. Many researchers have shown their great interest in stagnation point flow and widely explored this area by their research [20-30].

Nanofluids are engineerely manufactured fluids in which a small concentration of nanoparticles is added in such a way that it remains to behave as a fluid. The quantity of the solid concentration is kept small to make sure that the nature of the fluid is not changed. These small concentrations are producing the magical effects on the nature of the ordinary fluids. The addition of solid particle in liquids to improve their properties is not a new idea and originally dates back to Maxwell times 1873. But the addition of micrometer dimension solid particles has disadvantages like clogging, sedimentation, clogging of channels and decrease in pressure force. The molecular size of ordinary liquids ranges in nanometers for example size of most commonly used liquid water is 0.275 nm. This size is almost comparable to the size of

nanoparticles which ranges between 1-100 nm [31]. This makes it more suitable to mix with the molecules of ordinary liquids as compared to micro size particles. Because of their extreme small size, they create slip velocity between the liquid molecules and solid particles which prevents the gravitational settling of the molecules in fluid flow and avoid clogging of channel. The use of nanofluid as a coolant can reduce the cooling cost as reported by Choi [32]. Masuda et al. [33] claimed that the positive change in thermophysical properties of fluids is primarily due to the thermal conductivity and viscosity difference between the solid particles and base fluid. Buongiorno [34] sheds the light on an important flow aspect of nanoparticle i.e. they carry slip velocity to the neighboring liquid molecules. After the detailed analysis on possible impact of various slip mechanisms he reached the conclusion that the important slip mechanisms are the thermophoresis and Brownian motion. Researchers have given equal importance to the homogenous concentration model and the Buongiorno models simultaneously in recent literature. Hussain et al. [35] studied micro rotation effects in flowing fluid due to the moving surface in the presence of nanoparticles. It concludes that micro-rotation reduces the drag but increase the heat transfer mechanism. It is further highlighted *Cu* and *Ag* – water has low Nusselt number as compared to *Cu* – *Ag* – kerosene oil. Nanoparticles shape is equally playing an important role in the alteration of thermal properties of fluid. Considering this fact Timofeeva et al. [36] presented the detailed comparison of particle shapes and their effects on the thermal conductivity enhancement. It concludes that the blade shape particles produce the highest change in thermal conductivity of base fluid as compared to the other shaped nanoparticles. Vajravelu et al. [37] considered the heat transfer phenomenon in *Ag*- and *Cu*-water. Their analysis suggest that *Ag*-water produced deeper penetration of heat due to greater thermal boundary layer as compared to that of *Cu*-water. During last decade renowned researchers [38–44] have considered the flow of nanofluids in various shaped geometries.

The nanofluid flow behavior over a continuous stretching surface has been discussed by renowned scientist in recent years [45–48]. Hassani et al [49] developed the mathematical model for nanofluid flow over a moving surface and produced the analytical solution. Ibrahim et al [50] studied the effects of stagnation point flow due to the presence of normal direction magnetic field. Some other studies report the nanofluid flow with different kind of moving flat boundaries. Nadeem and Lee [51] examined the effects of exponentially moving surface on

the nanofluid boundary layer. Rana and Bhargava [52] presented the numerical solutions for the boundary layer nanofluid flow due to a non-linearly stretching velocity. Haq et al. [53] discussed the effects of radiation, microrotation and nanoparticles due to a vertically moving surface.

In above mentioned articles the surface is considered to be smooth, flat and flow is generated due to the motion of surface. The dynamics of the flow will be quite different in case of curved surface stretching. It requires the consideration of curvature effects and as well as consideration of moving wall. The formation of boundary layer around the surface will be different from the one for plane surface stretching. This phenomenon has potential application in polymer industry where the extrusion process is being done due to the movement of curved surface. Saleh et al. [54] analyzed the effects of curved stretching or shrinking surface on the micro-polar fluid flow, they found that multiple solutions will exist in this case. Pop et al. [55] analyzed the surface curvature effects in the presence of magnetic field, the presence of magnetic field has shown significant variation in the skin friction values. Moreover, they proved the existence of four solutions for small values of suction and magnetic parameters. Arifin et al. [56] examined the curvature and suction effects for a permeable curved surface. Rosca and Pop [57] suggested existence of multiple solutions in case of curved surface shrinking and creating a situation of reverse flow. They also examined the stability of solution and presented the range of values for which single solution, multiple solution and no solution exist. The case of shrinking is different from the stretching as it will create a reverse flow situation. Mathematically in the case of shrinking more than one solution will exist.

The question of thermal conductivity enhancement due to presence of nanoparticles is beyond doubt but the problem remains with the mathematical model whose data can be correctly correlated with the experimental observations. Maxwell model [58] is usually considered to analyze the impact of solid concentrations on the viscosity and thermal conductivity of the base fluid. This model is based on the assumption that the solid particles are highly dispersed and the temperature variation of one particle has negligible effect on the any other surrounding particle. Moreover, it is based on the steady state fluid assumption. This model doesn't consider the effect of shape and size of nanoparticles on the effective thermal conductivity of fluid. The Hamilton and Crosser [59] accommodated this constraint of the

Maxwell model and proposed the new model which reduces to the Maxwell model for the case of spherical particles. Yamada and Ota [60] proposed the unit cell model equation to describe the effects of solid concentration on the thermal conductivity. Zhang et al. [61] experimentally correlated the data for thermal conductivity enhancement and thermal diffusivity of different particles including carbon nanotubes and found that the experimental data is close to the results predicted by Maxwell, Yamada and Ota models. In 2005, Xue [62] has proposed an effective model for thermal conductivity of carbon nanotubes. He showed that the data generated by proposed model are in agreeing with the experimental observations generated for carbon nanotubes suspension. The nanoparticles effects on the nanofluid flow have been extensively discussed by researchers in recent years [63-65]. Keeping the above important highlights in mind, the present thesis is arranged as follows:

In first chapter we have presented the theoretical comparison of two main methods of nanofluids, phase flow and Buongiorno model. The governing flow equations for oscillatory oblique stagnation point flow are deliberated in fixed frame and in moving frame of references. The complicated coupled system of differential equations is transformed into non-dimensional form via a suitable similarity transformation. The numerical and analytical results have been obtained by using the homotopy analysis method and the results are observed through tables and graphs. The content of this chapter had been published in European journal of physics plus.

In second chapter we studied non-orthogonal stagnation point flow of nanofluid over the oscillatory and slip surface and assume the MHD effects in the direction of stream lines. We considered water based nanofluid with three types of nanoparticles, namely, Alumina (Al_2O_3), Copper (Cu), and Titania (TiO_2). Mathematical equations were formulated by applying magnetic field in the dividing stream line. The complicated coupled system of differential equations is transformed into non-dimensional form via a suitable similarity transformation. The numerical results have been obtained by using the midpoint method with Richardson extrapolation enhancement. The effects of physical parameters on the flow are showed graphically and discussed quantitatively. The content of this chapter had been published in journal of molecular liquids.

The third chapter is made to envision the characteristics of magneto-hydrodynamic oscillatory oblique stagnation point flow of micropolar nanofluid. The applied magnetic field

is assumed parallel towards dividing streamline. A comparative study is executed for copper Cu and Alumina Al_2O_3 nanoparticles while considering water as a base fluid. To be more specific, in the presence of both weak and strong concentration, the physical situation of micropolar fluid is mathematically modeled in terms of differential equations. The transformed coupled system is finally solved by midpoint method with the Richardson extrapolation enhancement and shooting mechanism with fifth order R-K Fehlberg technique. The obtained results are compared with existing published literature. An excellent match has been found which yields the validity of the current analysis. The content of this chapter has been submitted in journal of the Brazilian society of mechanical sciences and engineering.

In forth chapter, different proposed theoretical models for the thermal conductivity of Carbon nanotubes are analyzed. Both SWCNT and MWCNT are discussed in three types of base fluids namely ethylene glycol, engine oil and water. By using the fundamental governing laws and their modifications for the presence of solid concentrations are used to mathematically model the differential equations. The complicated coupled system of differential equations is transformed into non-dimensional form via a suitable similarity transformation. Then numerical results have been obtained by using the midpoint method with Richardson extrapolation enhancement. The numerical results can be computed when the length " L " and diameter " d " of CNT's are $3\mu m \leq L \leq 70\mu m$ and $10nm \leq d \leq 40nm$. It can be observed that when length and diameter of CNT's are $50\mu m \times 25nm$, the calculated value of Yamada and Ota model is greater than that of Xue and H-C (Hamilton and Crosser) model. The content of this chapter had been published in international journal of hydrogen energy.

Fifth chapter examines possible existence of reverse flow situation in unsteady nanofluid flow over a curved surface. Alumina (Al_2O_3) and Ethylene glycol are considered as a nanoparticles and base fluid, respectively. Mathematical form of the problem is obtained by using the fundamental form of governing equations for motion and heat transfer when solid concentrations are added to an ordinary liquid. The complicated coupled unsteady system is transformed into non-dimensional form by use relevant transformations. The solution of the nonlinear problem is produced by use of numerical scheme available in the form of BVP4C package in MATLAB. In the case of surface shrinking towards the surface a reverse flow situation is also developed and requires careful selection of solution by examining the stability

of solution. Detailed stability analysis is done, and critical values are determined for possible existence of dual solutions. Various parameters variation is analyzed by plotting graphs and tables. The numerical values are also calculated for the reduced Nusselt number and skin friction due to variation in values of different flow parameters. Results have shown that for the curved shrinking surfaces, one should expect multiple solutions for a set of parameter values like mass suction, curvature, nanoparticles volume fraction and unsteadiness. The content of this chapter has been submitted in journal of molecular liquids.

Sixth chapter examines the unsteady 3D non-axisymmetric Homann flow of an electrically conducting nanofluids in the presence of buoyancy forces. We consider the uniform external magnetic field, \mathbf{B}_0 , by neglecting induced magnetic field and examines the three possible directions of \mathbf{B}_0 which coincides with the direction of axes. A similarity solution is derived which involve the dimensionless parameters $\varphi, M, \omega, \gamma$ and λ . We have treated the case for forced convection when $\lambda = 0$ which arise from the singularity $\gamma = \mp 1$. We found that, for large γ and λ , the leading terms of the solutions are independent of M and ω , and the effects of φ in that solutions are negligible. Numerical results are found for illustrative values of all the flow parameters by using bvp4c scheme in MATLAB. The critical values λ_c of λ are seen in opposing flow for small rate of deceleration parameter ω while it changes to assisting flow for large value of ω . The content of this chapter has been submitted in scientific reports.

Chapter 1

A comparative study of different nanofluid models for the oscillatory stagnation point flow

1.1 Introduction

In this chapter, we have presented the theoretical comparison of two main methods of nanofluids, phase flow and Buongiorno models. The governing flow equations for oscillatory oblique stagnation point flow are deliberated in fixed frame and in moving frame of references. The complicated coupled system of differential equations is transformed into non-dimensional form via a suitable similarity transformation. Then numerical and analytical results have been obtained by using the homotopy analysis method and the results are discussed through graphs and tables.

1.2 Mathematical formulation for two-phase model:

Consider the problem of electrically conducting stagnation point flow of nanofluid over an oscillatory surface with velocity $U \cos \omega \bar{t}$. The fluid impinges obliquely to the oscillatory surface $\bar{y} = 0$. By neglecting external mechanical body force and body couple the flow rheological equations becomes

$$\frac{\partial \bar{u}}{\partial \bar{x}} + \frac{\partial \bar{v}}{\partial \bar{y}} = 0, \quad (1.1)$$

$$v_{nf} \left(\frac{\partial^2 \bar{u}}{\partial \bar{x}^2} + \frac{\partial^2 \bar{u}}{\partial \bar{y}^2} \right) - \bar{u} \frac{\partial \bar{u}}{\partial \bar{x}} - \bar{v} \frac{\partial \bar{u}}{\partial \bar{y}} - \frac{\partial \bar{u}}{\partial \bar{t}} - \frac{\sigma_f B_0^2}{\rho_{nf}} \bar{u} = \frac{1}{\rho_{nf}} \frac{\partial \bar{p}}{\partial \bar{x}}, \quad (1.2)$$

$$v_{nf} \left(\frac{\partial^2 \bar{v}}{\partial \bar{x}^2} + \frac{\partial^2 \bar{v}}{\partial \bar{y}^2} \right) - \bar{u} \frac{\partial \bar{v}}{\partial \bar{x}} - \bar{v} \frac{\partial \bar{v}}{\partial \bar{y}} - \frac{\partial \bar{v}}{\partial \bar{t}} = \frac{1}{\rho_{nf}} \frac{\partial \bar{p}}{\partial \bar{y}}, \quad (1.3)$$

$$\alpha_{nf} \left(\frac{\partial^2 T}{\partial \bar{x}^2} + \frac{\partial^2 T}{\partial \bar{y}^2} \right) - \bar{u} \frac{\partial T}{\partial \bar{x}} - \bar{v} \frac{\partial T}{\partial \bar{y}} - \frac{\partial T}{\partial \bar{t}} = 0, \quad (1.4)$$

where ρ_{nf} , v_{nf} and α_{nf} are defined in *Table 1.1*. From Eq. (1.1), we considered that

$$\bar{u} = \frac{\partial \bar{\psi}}{\partial \bar{y}}, \quad \bar{v} = -\frac{\partial \bar{\psi}}{\partial \bar{x}}. \quad (1.5)$$

Putting Eq. (1.5) in Eqs. (1.2)-(1.4) and eliminate the pressure from resulting equations using $\bar{p}_{\bar{y}\bar{x}} = \bar{p}_{\bar{x}\bar{y}}$ yields

$$\frac{\partial(\bar{\nabla}^2\bar{\psi})}{\partial\bar{t}} - \frac{\partial(\bar{\psi}, \bar{\nabla}^2\bar{\psi})}{\partial(\bar{x}, \bar{y})} - v_{nf}\bar{\nabla}^4\bar{\psi} + \frac{\sigma_f B_0^2}{\rho_{nf}} \frac{\partial^2\bar{\psi}}{\partial\bar{y}^2} = 0, \quad (1.6)$$

$$\alpha_{nf} \left(\frac{\partial^2 T}{\partial\bar{x}^2} + \frac{\partial^2 T}{\partial\bar{y}^2} \right) - \frac{\partial T}{\partial\bar{t}} - \frac{\partial\bar{\psi}}{\partial\bar{y}} \frac{\partial T}{\partial\bar{x}} + \frac{\partial\bar{\psi}}{\partial\bar{x}} \frac{\partial T}{\partial\bar{y}} = 0. \quad (1.7)$$

Eqs (1.6,1.7) were solved in both fixed and moving frame of references as studied by [66].

1.2.1 Fixed frame of reference:

According to [67] and [66], we assume that

$$\bar{\psi} = a[\bar{x}\bar{f}(\bar{y}) + \bar{g}(\bar{t}, \bar{y})]. \quad (1.8)$$

We consider that the fluid occupies the entire plane $\bar{y} > 0$ and the plate at $\bar{y} = 0$ is oscillating with velocity $U\cos(\omega\bar{t})$. Furthermore, we assume the stream function away from the plate as [66] $\bar{\psi} = a \left[\frac{1}{2}\gamma\bar{y}^2 + \bar{x}\bar{y} \right]$. Thus, the boundary conditions are,

$$\bar{f}(0) = 0, \quad \bar{g}(\bar{t}, 0) = 0, \quad \bar{f}'(0) = 0, \quad \bar{g}_{\bar{y}}(\bar{t}, 0) = Re\left[\frac{U}{a} e^{i\omega\bar{t}}\right] \quad (1.9)$$

$$\bar{f}'(\bar{y}) = 1, \quad \bar{g}_{\bar{y}}(\bar{t}, \bar{y}) = \gamma\bar{y} \quad \text{as} \quad \bar{y} \rightarrow \infty. \quad (1.10)$$

We are interested only in real part of the complex quantity. Making use of Eq. (1.8) and Eq. (1.6), we get

$$v_{nf} \frac{d^4\bar{f}}{d\bar{y}^4} + a \left(\bar{f} \frac{d^3\bar{f}}{d\bar{y}^3} - \frac{d\bar{f}}{d\bar{y}} \frac{d^2\bar{f}}{d\bar{y}^2} \right) - \frac{\sigma_f B_0^2}{\rho_{nf}} \frac{d^2\bar{f}}{d\bar{y}^2} = 0 \quad (1.11)$$

$$v_{nf} \frac{\partial^4\bar{g}}{\partial\bar{y}^4} + a \left(\bar{f} \frac{\partial^3\bar{g}}{\partial\bar{y}^3} - \frac{\partial\bar{g}}{\partial\bar{y}} \frac{d^2\bar{f}}{d\bar{y}^2} \right) - \frac{\partial^3\bar{g}}{\partial\bar{y}^2\partial\bar{t}} - \frac{\sigma_f B_0^2}{\rho_{nf}} \frac{\partial^2\bar{g}}{\partial\bar{y}^2} = 0 \quad (1.12)$$

Integrate Eqs. (1.11) and (1.12) with respect to \bar{y} and use Eq. (1.10), we get

$$v_{nf} \frac{d^3 \bar{f}}{d\bar{y}^3} + a \left(\bar{f} \frac{d^2 \bar{f}}{d\bar{y}^2} - \frac{d\bar{f}}{d\bar{y}} \frac{d\bar{f}}{d\bar{y}} \right) - \frac{\sigma_f B_0^2}{\rho_{nf}} \frac{d\bar{f}}{d\bar{y}} = -a - \frac{\sigma_f B_0^2}{\rho_{nf}} \quad (1.13)$$

$$v_{nf} \frac{\partial^3 \bar{g}}{\partial \bar{y}^3} + a \left(\bar{f} \frac{\partial^2 \bar{g}}{\partial \bar{y}^2} - \frac{\partial \bar{g}}{\partial \bar{y}} \frac{d\bar{f}}{d\bar{y}} \right) - \frac{\partial^2 \bar{g}}{\partial \bar{y} \partial \bar{t}} - \frac{\sigma_f B_0^2}{\rho_{nf}} \frac{\partial \bar{g}}{\partial \bar{y}} = -\frac{\sigma_f B_0^2}{\rho_{nf}} \gamma \bar{y} \quad (1.14)$$

For non-dimensionalizing, we introduce

$$\begin{aligned} \bar{f}(\bar{y}) &= \sqrt{\frac{v_f}{a}} f(y), & \bar{g}(\bar{t}, \bar{y}) &= \frac{v_f}{a} [g_0(y) + \varepsilon g_1(y) e^{it}], \\ y &= \sqrt{\frac{a}{v_f}} \bar{y}, & \Omega &= \frac{\omega}{a}, & \varepsilon &= \frac{U}{\sqrt{v_f a}}, & t &= \omega \bar{t} \end{aligned} \quad (1.15)$$

Eqs. (1.13)-(1.14) along with the boundary conditions (1.9) and (1.10) take the form

$$\frac{v_{nf}}{v_f} f'''' + f f'' - (f')^2 - M^2 f' = -1 - M^2, \quad (1.16)$$

$$\frac{v_{nf}}{v_f} g_0'''' + f g_0'' - f' g_0' - M^2 g_0' = -M^2 \gamma y, \quad (1.17)$$

$$\frac{v_{nf}}{v_f} g_1'''' + f g_1'' - f' g_1' - i \Omega g_1' - M^2 g_1' = 0, \quad (1.18)$$

$$f'(0) = 0, \quad f(0) = 0, \quad f'(\infty) = 1, \quad (1.19)$$

$$g_0'(0) = 0, \quad g_0(0) = 0, \quad g_0''(\infty) = \gamma, \quad (1.20)$$

$$g_1'(0) = 1, \quad g_1(0) = 0, \quad g_1'(\infty) = 0. \quad (1.21)$$

In flow along the surface the important parameters to determine the flow behavior is the skin friction coefficient C_f . The shear stress at the plate is given by τ_w and are defined below

$$C_f = \frac{\tau_w}{\frac{1}{2} \rho_f U_w^2},$$

$$\tau_w = \mu_{nf} \frac{\partial \bar{u}}{\partial \bar{y}} \Big|_{\bar{y}=0}.$$

By using Eqs. (1.15), the above equations reduced to

$$\frac{1}{2}Re_{\bar{x}}C_f = \frac{\mu_{nf}}{\mu_f} [\sqrt{Re_{\bar{x}}}f''(0) + g_0''(0) + \epsilon g_1''(0)e^{it}], \quad (1.22)$$

where $Re_{\bar{x}} = a\bar{x}^2/\nu_f$.

With the help of Eqs. (1.15), we find the dimensionless stream function as

$$\bar{\psi} = \frac{\bar{\psi}}{\nu_f} = xf(y) + g_0(y) + \epsilon g_1(y)e^{it}. \quad (1.23)$$

The separating stream line making an angle, say α , with the plate. This line can be obtained by putting $\psi = 0$ as [66]. Thus, we have

$$\psi = \frac{1}{2}\gamma y^2 + x y = 0$$

which gives a straight line $y = \left(-\frac{2}{\gamma}\right)x$ whose slope is $m = -\frac{2}{\gamma}$. Thus, we can easily find the relation between the free stream parameter γ and the impinging angle α as

$$\alpha = \tan^{-1}\left(-\frac{2}{\gamma}\right).$$

Further, the point of attachment of the separation stream line can be found by setting $\tau_w = 0$. It is also known as the point of zero skin friction

$$x_s = -\frac{[g_0''(0) + \epsilon g_1''(0)e^{it}]}{f''(0)}.$$

1.2.2 Moving frame of reference:

To discuss the flow equations in moving frame, we considered that the (\bar{x}, \bar{y}) frame is moving with the plate such that the plate becomes at rest reference to (\bar{x}, \bar{y}) coordinates system. The stream function in this case can be considered as [66]

$$\bar{\psi} = a[\bar{x}\bar{f}(\bar{y}) + \bar{h}(\bar{t}, \bar{y})]. \quad (1.24)$$

The boundary constrains become

$$\left. \begin{aligned} \bar{f}(0) = 0, \quad \bar{h}(\bar{t}, 0) = 0, \quad \bar{f}'(0) = 0, \quad \bar{h}_{\bar{y}}(\bar{t}, 0) = 0 \\ \bar{f}'(\bar{y}) = 1, \quad \bar{h}_{\bar{y}}(\bar{t}, \bar{y}) = \gamma\bar{y} - \operatorname{Re}\left[\frac{U}{a}e^{i\omega\bar{t}}\right] \text{ as } \bar{y} \rightarrow \infty, \end{aligned} \right\} \quad (1.25)$$

Substitute Eq. (1.24) in Eq. (1.6) and comparing like powers of \bar{x} . After that integrate once with respect to \bar{y} and then use the conditions of free stream, we get

$$v_{nf} \frac{d^3 \bar{f}}{d\bar{y}^3} + a \left(\bar{f} \frac{d^2 \bar{f}}{d\bar{y}^2} - \frac{d\bar{f}}{d\bar{y}} \frac{d\bar{f}}{d\bar{y}} \right) - \frac{\sigma_f B_0^2}{\rho_{nf}} \frac{d\bar{f}}{d\bar{y}} = -a - \frac{\sigma_f B_0^2}{\rho_{nf}} \quad (1.26)$$

$$\begin{aligned} v_{nf} \frac{\partial^3 \bar{h}}{\partial \bar{y}^3} + a \left(\bar{f} \frac{\partial^2 \bar{h}}{\partial \bar{y}^2} - \frac{\partial \bar{h}}{\partial \bar{y}} \frac{d\bar{f}}{d\bar{y}} \right) - \frac{\partial^2 \bar{h}}{\partial \bar{y} \partial \bar{t}} - \frac{\sigma_f B_0^2}{\rho_{nf}} \frac{\partial \bar{h}}{\partial \bar{y}} \\ = -\frac{\sigma_f B_0^2}{\rho_{nf}} \gamma \bar{y} + \left(1 + \frac{i\omega}{a} + \frac{\sigma_f B_0^2}{\rho_{nf} a} \right) U e^{i\omega \bar{t}} \end{aligned} \quad (1.27)$$

Introducing the dimensionless shear flow component of stream function $\bar{h}(\bar{t}, \bar{y}) = \frac{v_f}{a} [g_0(\bar{y}) - \varepsilon h(\bar{y})e^{it}]$ and using (1.15) and Eqs. (1.24)-(1.27), we obtain

$$\frac{v_{nf}}{v_f} f''' + ff'' - (f')^2 - M^2 f' = -1 - M^2, \quad (1.28)$$

$$\frac{v_{nf}}{v_f} g_0''' + f g_0'' - f' g_0' - M^2 g_0' = -M^2 \gamma \bar{y}, \quad (1.29)$$

$$\frac{v_{nf}}{v_f} h''' + fh'' - f'h' - i\Omega h' - M^2 h' = -(1 + i\Omega + M^2) \quad (1.30)$$

$$f'(0) = 0, \quad f(0) = 0, \quad f'(\infty) = 1, \quad (1.31)$$

$$g_0'(0) = 0, \quad g_0(0) = 0, \quad g_0''(\infty) = \gamma, \quad (1.32)$$

$$h'(0) = 0, \quad h(0) = 0, \quad h'(\infty) = 1. \quad (1.33)$$

The skin friction coefficient C_f and the wall shear stress τ_w , along the plate, are

$$C_f = \frac{\tau_w}{\frac{1}{2} \rho_f U_w^2}$$

$$\tau_w = \mu_{nf} \frac{\partial \bar{u}}{\partial \bar{y}} \Big|_{\bar{y}=0}.$$

In non-dimensional form, the above equations take the form

$$\frac{1}{2} Re_{\bar{x}} C_f = \frac{\mu_{nf}}{\mu_f} [\sqrt{Re_{\bar{x}}} f''(0) + g_0''(0) - \epsilon h''(0) e^{it}], \quad (1.34)$$

Further, the dimensionless stream function can be obtained, as

$$\psi = \frac{\bar{\psi}}{v_f} = x f(y) + g_0(y) - \epsilon h(y) e^{it}. \quad (1.35)$$

The separating stream line can be obtained by setting the far away stream function $\psi = 0$, obtain

$$\psi = \frac{1}{2} \gamma y^2 + x y - \epsilon y e^{it} = 0.$$

This gives a straight line $y = \left(-\frac{2}{\gamma}\right)x + \epsilon e^{it}$ whose slope is $m = -\frac{2}{\gamma}$. Thus, we can easily find the relation between the free stream parameter γ and the impinging angle α as

$$\alpha = \tan^{-1} \left(-\frac{2}{\gamma} \right).$$

Further, the point of attachment of the separation stream line can be found by setting $\tau_w = 0$. It is also known as the point of zero skin friction

$$\bar{x}_s = -\frac{[g_0''(0) - \epsilon h''(0) e^{it}]}{f''(0)}.$$

1.2.3 Energy Equation:

The energy equation is same, defined in Eq. (1.7), in both fixed and in moving frame of references because the temperature in each layer can be seen same in both references. The boundary conditions for Eq. (1.7) is assumed as

$$T(\bar{x}, 0, \bar{t}) = T_w + \epsilon(T_w - T_\infty) Re[e^{i\omega \bar{t}}], \quad T(\bar{x}, \infty, \bar{t}) = T_\infty, \quad (1.36)$$

Introduce the non-dimensional temperature profile

$$\theta(y, t) = \frac{T - T_\infty}{T_w - T_\infty} = \theta_0(y) + \varepsilon\theta_1(y)e^{it}$$

and using Eqs. (1.15), we attain

$$\frac{k_{nf}}{k_f} \theta_0'' + Pr \frac{(\rho C_p)_{nf}}{(\rho C_p)_f} f \theta_0' = 0, \quad (1.37)$$

$$\frac{k_{nf}}{k_f} \theta_1'' + Pr \frac{(\rho C_p)_{nf}}{(\rho C_p)_f} f \theta_1' - i\Omega Pr \frac{(\rho C_p)_{nf}}{(\rho C_p)_f} \theta_1 = 0, \quad (1.38)$$

$$\left. \begin{aligned} \theta_0(0) = 1, \quad \theta_0(\infty) = 0 \\ \theta_1(0) = 1, \quad \theta_1(\infty) = 0 \end{aligned} \right\}. \quad (1.39)$$

The local Nusselt number Nu and the surface heat flux q_w , from the flat plate, are

$$Nu = \frac{\bar{x} q_w}{k_f (T_w - T_\infty)},$$

$$q_w = -k_{nf} \left. \frac{\partial T}{\partial y} \right|_{\bar{y}=0}.$$

Using Eqs. (1.15), we obtain

$$(Re_{\bar{x}})^{-\frac{1}{2}} Nu = -\frac{k_{nf}}{k_f} (\theta_0'(0) + \varepsilon\theta_1(0)e^{it}), \quad (1.40)$$

1.3 Mathematical formulation for Buongiorno model:

To avoid the repetition, the momentum equations for Buongiorno nanofluid model can be obtained from section 1.2 by putting $\varphi = 0$ (defined in v_{nf}/v_f see **Table 1.1**) for both fixed and moving frame of references. Therefore, here we mention only temperature and concentration equations as

$$\alpha \left(\frac{\partial^2 T}{\partial \bar{x}^2} + \frac{\partial^2 T}{\partial \bar{y}^2} \right) - \bar{u} \frac{\partial T}{\partial \bar{x}} - \bar{v} \frac{\partial T}{\partial \bar{y}} - \frac{\partial T}{\partial \bar{t}} + \frac{(\rho C_p)_s}{(\rho C_p)_f} \frac{D_T}{T_\infty} \left[\left(\frac{\partial T}{\partial \bar{x}} \right)^2 + \left(\frac{\partial T}{\partial \bar{y}} \right)^2 \right] + \frac{(\rho C_p)_s}{(\rho C_p)_f} D_B \left(\frac{\partial C}{\partial \bar{x}} \frac{\partial T}{\partial \bar{x}} + \frac{\partial C}{\partial \bar{y}} \frac{\partial T}{\partial \bar{y}} \right) = 0 \quad (1.41)$$

$$D_B \left(\frac{\partial^2 C}{\partial \bar{x}^2} + \frac{\partial^2 C}{\partial \bar{y}^2} \right) - \bar{u} \frac{\partial C}{\partial \bar{x}} - \bar{v} \frac{\partial C}{\partial \bar{y}} - \frac{\partial C}{\partial \bar{t}} + \frac{D_T}{T_\infty} \left(\frac{\partial^2 T}{\partial \bar{x}^2} + \frac{\partial^2 T}{\partial \bar{y}^2} \right) = 0 \quad (1.42)$$

$$\left. \begin{aligned} T(\bar{t}, \bar{x}, 0) &= T_w + \epsilon(T_w - T_\infty) \operatorname{Re}[e^{i\omega \bar{t}}], & T(\bar{t}, \bar{x}, \infty) &= T_\infty \\ C(\bar{t}, \bar{x}, 0) &= C_w + \epsilon(C_w - C_\infty) \operatorname{Re}[e^{i\omega \bar{t}}], & C(\bar{t}, \bar{x}, \infty) &= C_\infty \end{aligned} \right\} \quad (1.43)$$

By using (1.8) and the similarity variables define below, we attain

$$\begin{aligned} \bar{f}(\bar{y}) &= \sqrt{\frac{\nu_f}{a}} f(y), & \theta(t, y) &= [\theta_0(y) + \epsilon \theta_1(y) e^{it}] = \frac{T - T_\infty}{T_w - T_\infty}, \\ y &= \sqrt{\frac{a}{\nu_f}} \bar{y}, & \Omega &= \frac{\omega}{a}, & \epsilon &= \frac{U}{\sqrt{\nu_f a}}, & t &= \omega \bar{t} \\ \phi(t, y) &= [\phi_0(y) + \epsilon \phi_1(y) e^{it}] = \frac{C - C_\infty}{C_w - C_\infty} \end{aligned} \quad]$$

$$\frac{1}{Pr} \theta_0'' + f \theta_0' + Nb \phi_0' \theta_0' + Nt (\theta_0')^2 = 0, \quad (1.44)$$

$$\frac{1}{Pr} \theta_1'' + f \theta_1' - i\Omega \theta_1 + Nb(\phi_1' \theta_0' + \phi_0' \theta_1') + 2Nt \theta_0' \theta_1' = 0, \quad (1.45)$$

$$\phi_0'' + Sc f \phi_0' + \frac{Nt}{Nb} \theta_0'' = 0, \quad (1.46)$$

$$\phi_1'' + Sc(f \phi_0' - i\Omega \phi_1) + \frac{Nt}{Nb} \theta_1'' = 0, \quad (1.47)$$

$$\left. \begin{aligned} \theta_0(0) &= 1, & \theta_0(\infty) &= 0 \\ \theta_1(0) &= 1, & \theta_1(\infty) &= 0 \\ \phi_0(0) &= 1, & \phi_0(\infty) &= 0 \\ \phi_1(0) &= 1, & \phi_1(\infty) &= 0 \end{aligned} \right\} \quad (1.48)$$

where

$$Pr = \frac{\nu_f}{\alpha_f}, Nt = \frac{D_T (\rho C_p)_s (T_w - T_\infty)}{T_\infty (\rho C_p)_f \nu_f}, Nb = D_B \frac{(\rho C_p)_s (C_w - C_\infty)}{(\rho C_p)_f \nu}, Sc = \frac{\nu_f}{D_B}.$$

The physical quantities are the local Nusselt number, the Sherwood number, the surface heat flux q_w and the mass diffusion flux j_w , along the plate, which can be written as

$$Nu = \frac{\bar{x} q_w}{k(T_w - T_\infty)},$$

$$Sh = \frac{\bar{x} j_w}{D(C_w - C_\infty)},$$

$$q_w = -k \left. \frac{\partial T}{\partial \bar{y}} \right|_{\bar{y}=0},$$

$$j_w = -D \left. \frac{\partial C}{\partial \bar{y}} \right|_{\bar{y}=0}.$$

In dimensionless form the above quantities reduced to

$$(Re_{\bar{x}})^{-\frac{1}{2}} Nu = -[\theta_0'(0) + \varepsilon \theta_1(0) e^{it}] \quad (1.49)$$

$$(Re_{\bar{x}})^{-\frac{1}{2}} Sh = -[\phi_0'(0) + \varepsilon \phi_1(0) e^{it}] \quad (1.50)$$

1.4 Homotopy Analysis method:

For the homotopy analysis method, the main requirements are linear operators and initial guesses which are defined below, whereas the detail is given in the book of Liao [68]. Therefore, in the preceding sections we presented only the numerical and graphical data.

$$\left. \begin{aligned} f_0(y) &= y - 1 + e^{-y}, & g_{00}(y) &= \frac{\gamma}{2} y^2, \\ g_{10}(y) &= 1 - e^{-y}, & h_0(y) &= y - 1 + e^{-y} \\ \theta_{00}(y) &= e^{-y}, & \theta_{10}(y) &= e^{-y}, \\ \phi_{00}(y) &= e^{-y}, & \phi_{10}(y) &= e^{-y} \end{aligned} \right\} \quad (1.51)$$

The linear operators are given by,

$$\begin{aligned}
L_f &= \frac{d^3 f}{dy^3} + \frac{d^2 f}{dy^2}, & L_{g_0} &= \frac{d^3 g_0}{dy^3}, \\
L_{g_1} &= \frac{d^3 g_1}{dy^3} - \frac{dg_1}{dy}, & L_h &= \frac{d^3 h}{dy^3} + \frac{d^2 h}{dy^2} \\
L_{\theta_0} &= \frac{d^2 \theta_0}{dy^2} - \theta_0, & L_{\theta_1} &= \frac{d^2 \theta_1}{dy^2} - \theta_1, \\
L_{\phi_0} &= \frac{d^2 \phi_0}{dy^2} - \phi_0, & L_{\phi_1} &= \frac{d^2 \phi_1}{dy^2} - \phi_1 \text{)}
\end{aligned} \tag{1.52}$$

1.5 Results and Discussion:

The aim of this study is to present the comparison of main models of nanofluids, i.e. two-phase model and Buongiorno model. This comparison is made on the rising parameters of oblique stagnation point flow over oscillatory surface. The flow equations (1.16)-(1.21), (1.30), (1.37)-(1.39) and (1.44)-(1.48) have been solved in fixed and moving frame of references by using homotopy analysis method. We have used copper (*Cu*) as a nanoparticle and water as a base fluid in this chapter whereas the thermophysical properties of nanoparticles and base fluid are given in **Table 1.2**. To validate the HAM procedure, the comparison of data is made for the particular case as shown in **Table 1.3**. These results are in good agreement with the former results by [69,70,71]. We can observe from **Fig. 1.1** that the normal component of velocity $f'(y)$ increases against M and φ and the boundary layer thickness in the normal direction decreases against both parameters. Also, the magnitude of steady part of shear velocity $g_0'(y)$ increase against φ and M as shown in **Fig. 1.2**. As well as, these figures show that the behavior of $g_0'(y)$ for $\gamma < 0$ and $\gamma > 0$ is symmetric about $\gamma = 0$. **Fig. 1.3** display the effects of M and φ on the temporal parts of shear velocity in fixed frame of reference $g_1'(y)$ and in moving frame of reference $h'(y)$. It is seen that $g_1'(y)$ increases while $h'(y)$ decreases against both M and φ whereas the boundary layer thickness of both velocity components decreases against M and φ . **Fig. 1.4** depicts shear velocity component $g_y(y, t)$ in the unsteady domain. Generally, free stream velocity drives the flow due to the plate oscillation. At the plate, the velocity of nanofluid is minimum and gradually it approaches the free stream velocity as approaches infinity. It is observed that, in fixed frame, the amplitude of oscillation is maximum at the surface, whereas, in the moving frame the amplitude is maximum at the free stream. It satisfies the boundary constrains which also shows validity of obtained results. **Figs. 1.5** are plotted for

stream lines in the case of impinging fluid at different angles. It intersects the surface at the point $x = x_s$ which is the point of zero velocity that is stagnation point. Its location depends on the values of γ . It is observed that for the positive values of γ , the stagnation point appears on the left sides of the plate from the origin whereas the opposite behavior can be seen for the negative values of γ . The behavior of temperature and concentration profile against different physical parameters are shown in **Figs. 1.6**. It is observed that the temperature profile increases against φ and the amplitude of oscillation is maximum at the surface and gradually decrease when it goes away from the surface. Furthermore, temperature profile increases for higher values of Nt and Nb , whereas, concentration profile increases against Nt and decreases for higher values of Nb . For some particular values of Pr , the temperature profile is observed in two-phase model and Buongiorno model as shown in **Fig. 1.7**. We observed that $\theta(y, t)$ decreases in both models for higher values of Pr and the value of $\theta(y, t)$ in two-phase model is higher than the Buongiorno model. The influence of skin friction coefficient against different physical parameters are shown in **Figs. 1.8**. We observed that the behavior of skin friction is same in both frame of references. Also, the skin friction coefficient has oscillation behavior against time t . Furthermore, skin friction increases against M and φ and change the phase of oscillation for different values of Ω . The influence of Nusselt number against different involving parameters are described in **Figs. 1.9**. from these figures we observed that Nusselt number has oscillatory behavior against time t and the amplitude of oscillation increase by increasing Ω . Also, the value of Nusselt number is same for $Nt = Nb = 0$ in Buongiorno model and $\varphi = 0$ in two-phase model. Further, Nusselt number increase with respect to Pr in both nanofluid models. **Fig. 1.10** suggest that Sherwood number increases against Nb and decreases against Nt .

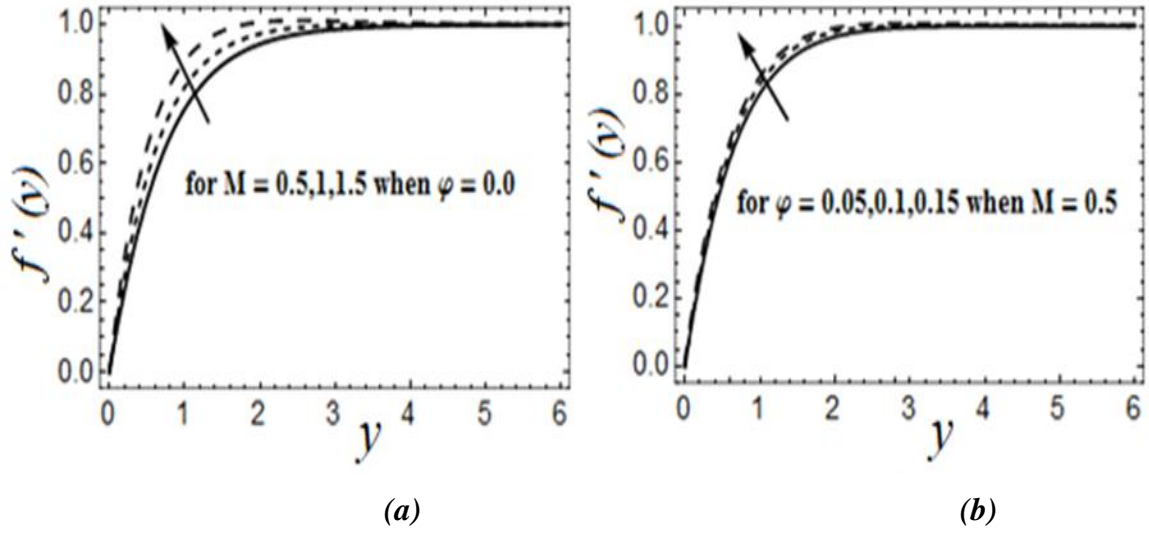


Fig. 1. 1. Normal component of velocity profile $f'(y)$ against M and ϕ .

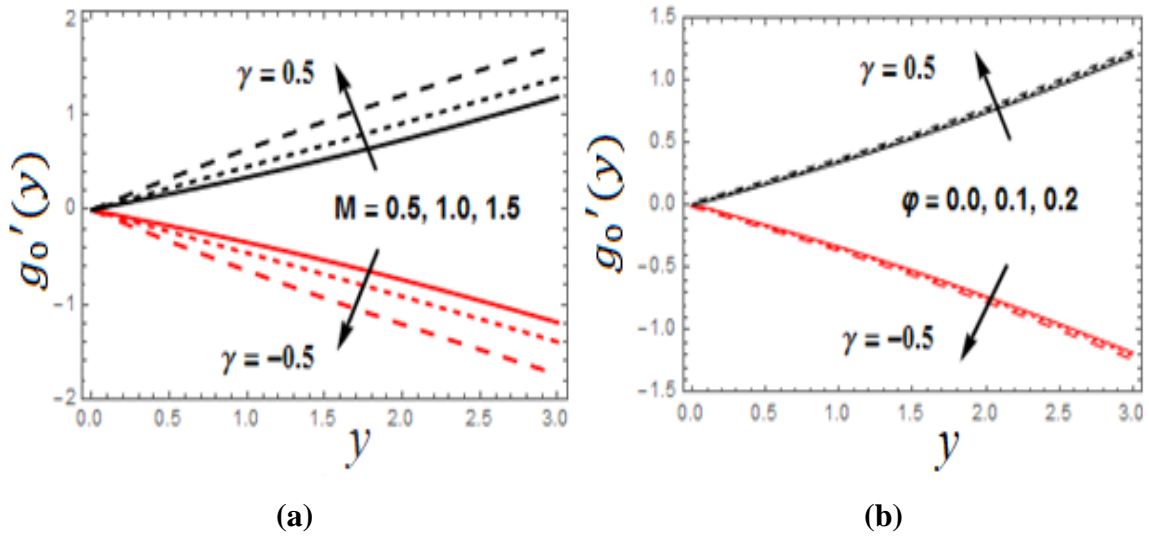


Fig. 1. 2. Steady part of shear velocity $g_0'(y)$ against M and ϕ .

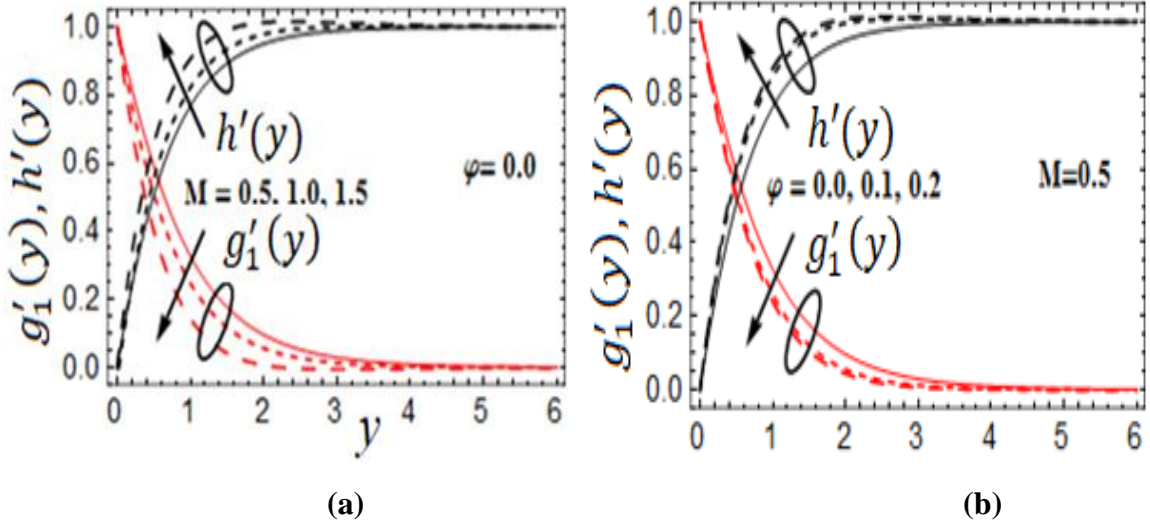


Fig. 1. 3. Temporal parts of shear velocity in fixed frame $g'_1(y)$ and moving frame $h'(y)$ against M and φ .

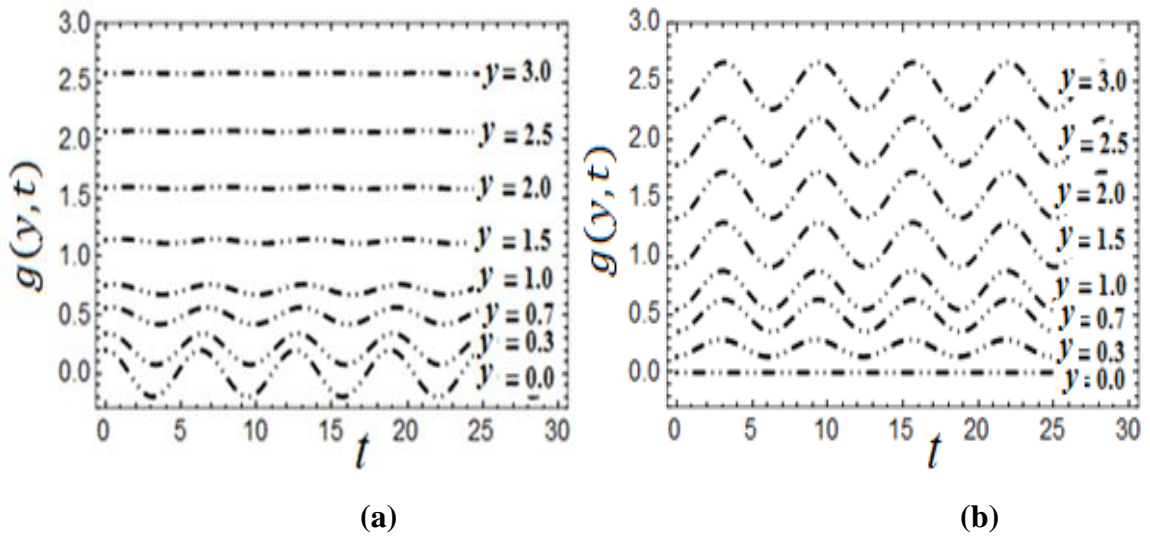
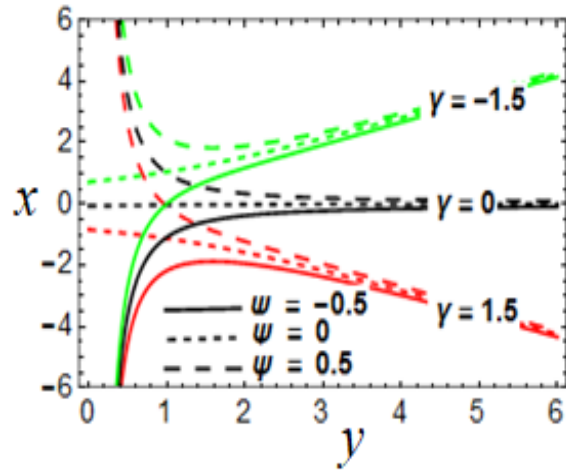
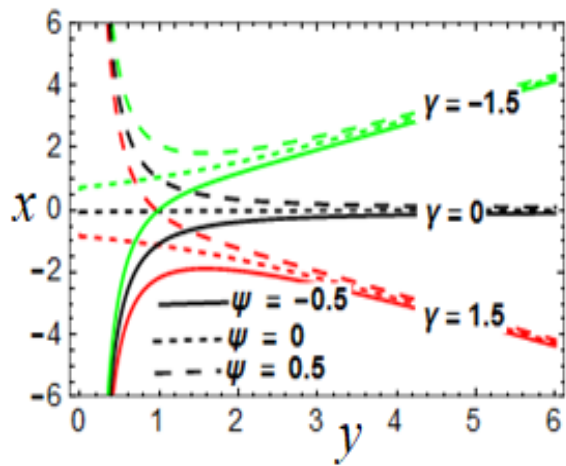


Fig. 1. 4. Time dependent flow $g_y(y, t)$ at different locations from the surface when $\Omega = 1, \gamma = 1, M = 0.5, \varepsilon = 0.2$. (a) fixed frame of reference (b) moving frame of reference.



(a)



(b)

Fig. 1. 5. Streamlines pattern when $\Omega = 1$, $M = 0.5$, $t = \frac{\pi}{2}$, $\varepsilon = 0.2$ **(a)** fixed frame of reference **(b)** moving frame of reference.

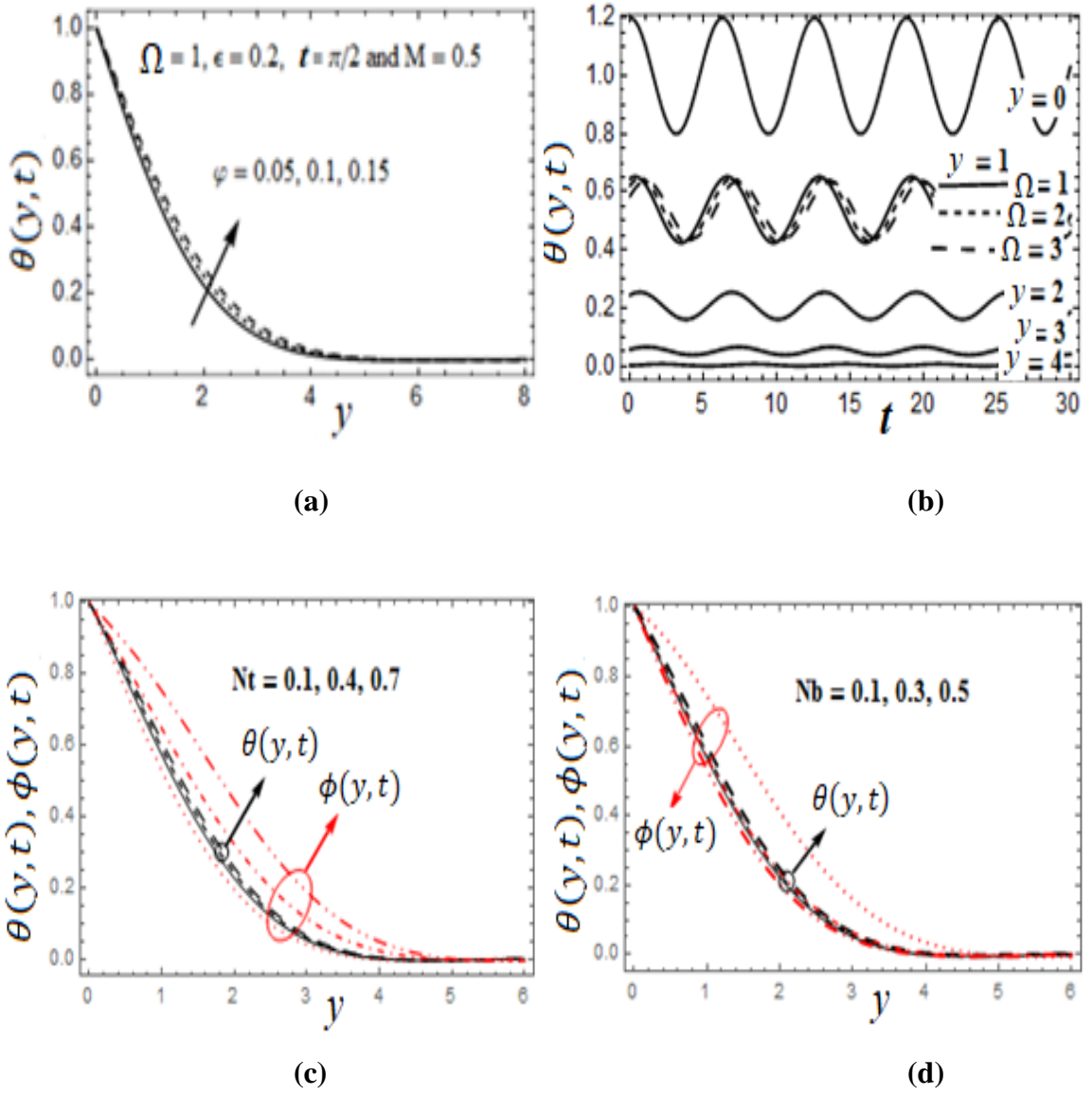


Fig. 1. 6. Influence of concentration and temperature profiles for different values of the involving parameters.

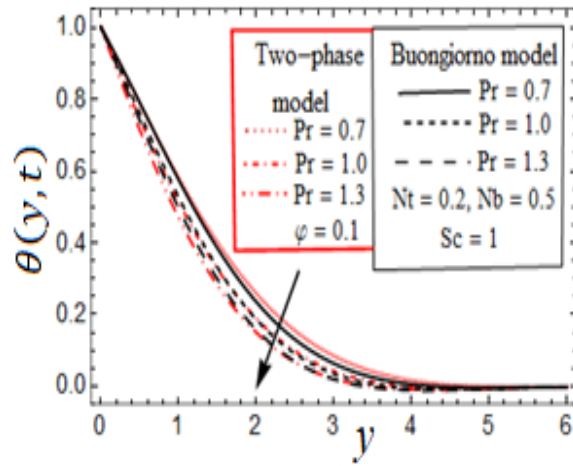


Fig. 1. 7. Comparison of two-phase model and Buongiorno model against Pr when $\Omega = 1, M = 0.5, t = \frac{\pi}{2}, \varepsilon = 0.2$.

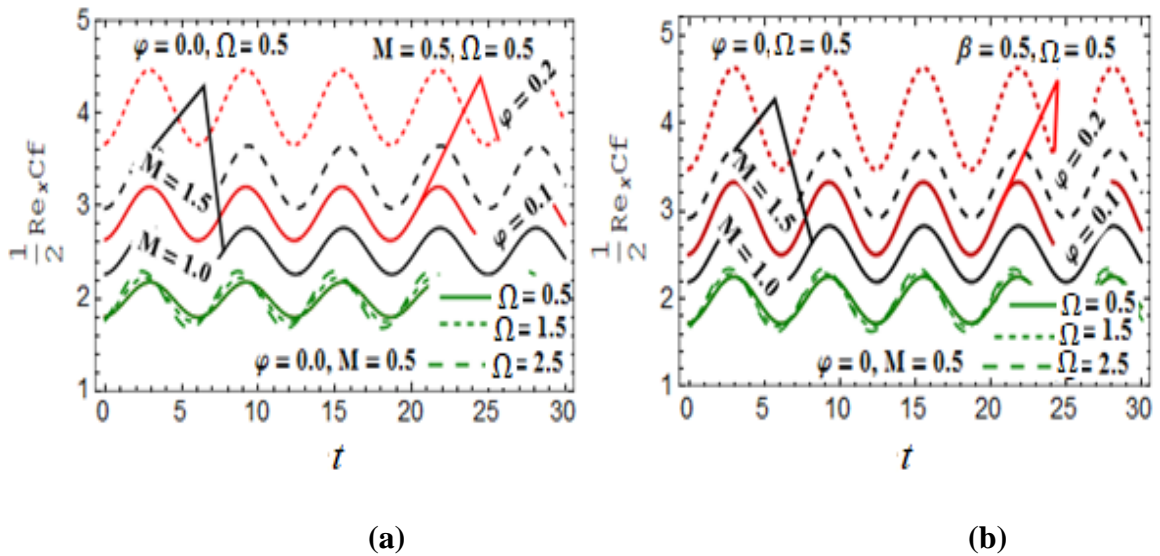
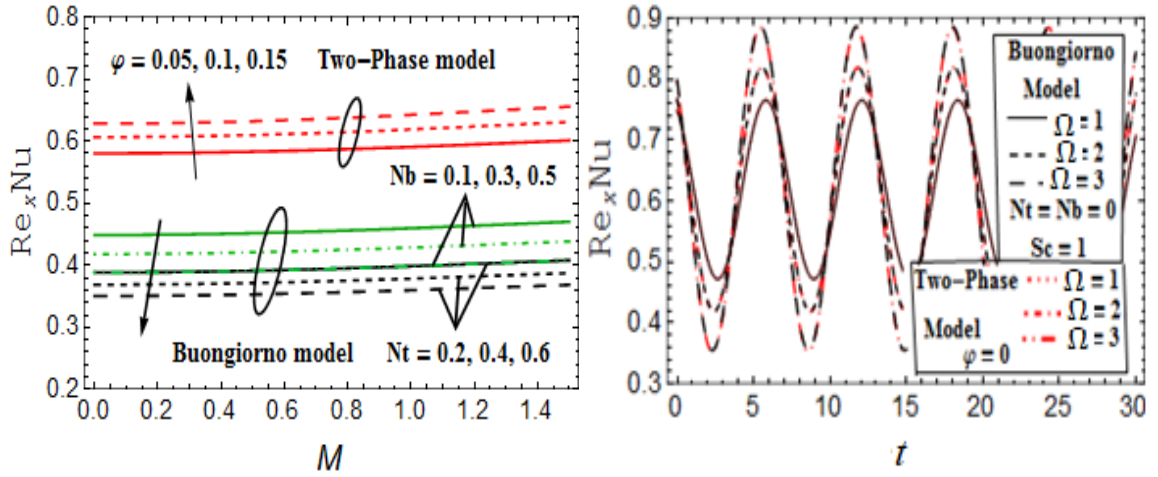
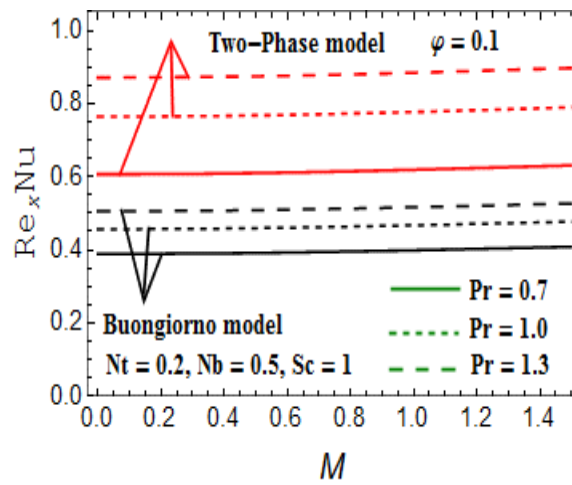


Fig. 1. 8. Variation of skin friction coefficient (a) fixed frame of reference (b) moving frame of reference.



(a)

(b)



(c)

Fig. 1. 9. Variation of Nusselt number (a) Nt, Nb and φ (b) Ω (c) Pr .

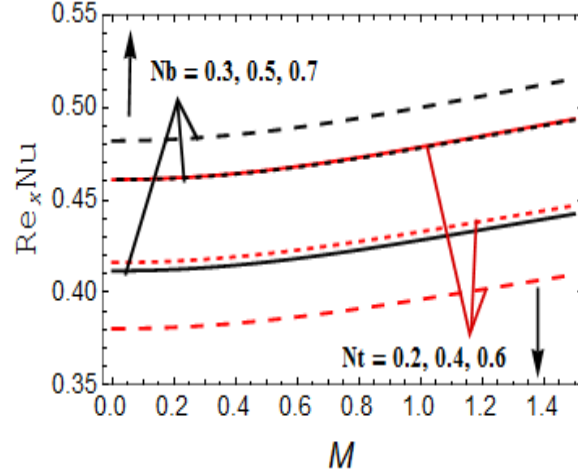


Fig. 1. 10. Sherwood number for different value of Nt and Nb .

Table. 1. 1. Effective thermophysical quantities of nanofluids [72]

Dynamic viscosity of nanofluid	$\mu_{nf} = \frac{\mu_f}{(1 - \varphi)^{2.5}}$
Density of nanofluid	$\rho_{nf} = (1 - \varphi)\rho_f + \varphi\rho_s$
Thermal expansion coefficient of nanofluid	$\beta_{nf} = (1 - \varphi)\beta_f + \varphi\beta_s$
Electric conductivity of nanofluid	$\sigma_{nf} = (1 - \varphi)\sigma_f + \varphi\sigma_s$
Kinematic viscosity of nanofluid	$\nu_{nf} = \frac{\mu_f}{(1 - \varphi)^{2.5} \times [(1 - \varphi)\rho_f + \varphi\rho_s]}$
Heat capacity of nanofluid	$(\rho C_p)_{nf} = (1 - \varphi)(\rho C_p)_f + \varphi(\rho C_p)_s$
Thermal conductivity of nanofluid	$\frac{k_{nf}}{k_f} = \frac{(k_s + 2k_f) - 2\varphi(k_f - k_s)}{(k_s + 2k_f) + \varphi(k_f - k_s)}$
Thermal diffusivity of nanofluid	$\alpha_{nf} = \frac{k_{nf}}{(\rho C_p)_{nf}}$

Table. 1. 2. Thermophysical properties of nanoparticles and base fluids [72].

Thermophysical properties	$C_p (J / kgK)$	$\rho (kg / m^3)$	$k (W / mK)$	$\sigma (S/m)$	$\beta \times 10^{-5} (1/K)$
Pure-water	4179	997.1	0.613	5.5×10^{-6}	21
Ethylene glycol	2430	1115	0.253	1×10^{-7}	70
Engine oil	1910	884	0.144	1.07×10^{-6}	57
Copper (<i>Cu</i>)	385	8933	400	59.6×10^6	1.67
Alumina (Al_2O_3)	765	3970	40	35×10^6	0.85
Titania or Titanium Oxide (TiO_2)	686.2	4250	8.9538	2.0×10^6	0.9
SWCNT	425	2600	6600	1.26×10^6	0.19
MWCNT	796	1600	3000		0.21

Table. 1. 3. Validation of results for $f''(0)$.

M	Ariel [69]	Grosan et al. [70]	T. Javed [71]	Present Study
0.0	1.232588	1.232588	1.232597	1.232593
0.16	1.295368	1.295368	1.295377	1.295369
0.64	1.467976	1.467976	1.467987	1.467975
1.0	1.585331	1.585331	1.585342	1.585329

1.6 Conclusion

This chapter is based on the comparison of two main models of nanofluids namely two-phase model and Buongiorno model. We have checked this comparison on the oblique stagnation point flow over an oscillatory surface and considered a mixture of Cu and water as a nanofluid for two-phase model. The governing equations of this comparative study have been solved analytically with the help of homotopy analysis method and results are discussed through graphs. The conclusions of this study are summarized as follows:

- In fixed frame of reference, the amplitude of oscillation is maximum at the surface while in moving frame the amplitude is maximum at free stream.
- Both skin friction coefficient and Nusselt number have oscillatory behavior against t .
- Generally, the values of physical quantities skin friction coefficient and Nusselt number doesn't match for two-phase model and Buongiorno model.
- The values of Nusselt number are same for both models, only, when we choose $Nt = Nb = 0$ in Buongiorno model and $\varphi = 0$ in two-phase model.
- The behavior of skin friction coefficient and Nusselt number are same in both fixed frame and moving frame of reference.

Chapter # 2

Phase flow study of MHD nanofluid with slip effects on oscillatory oblique stagnation point flow in view of inclined magnetic field

2.1 Introduction

In second chapter we studied oblique stagnation point flow of MHD nanofluid over the oscillatory and slip surface. We compared three different nanoparticles namely, Alumina (Al_2O_3), Copper (Cu), and Titania (TiO_2) by assuming water as a base fluid. Mathematical equations were formulated by applying magnetic field in the direction of dividing stream line. The complicated coupled system of differential equations is transformed into non-dimensional form via a suitable similarity transformation. The numerical results have been obtained by using the midpoint method with Richardson extrapolation enhancement. The effects of different involved parameters on the flow characteristics are presented in tables and showed graphically.

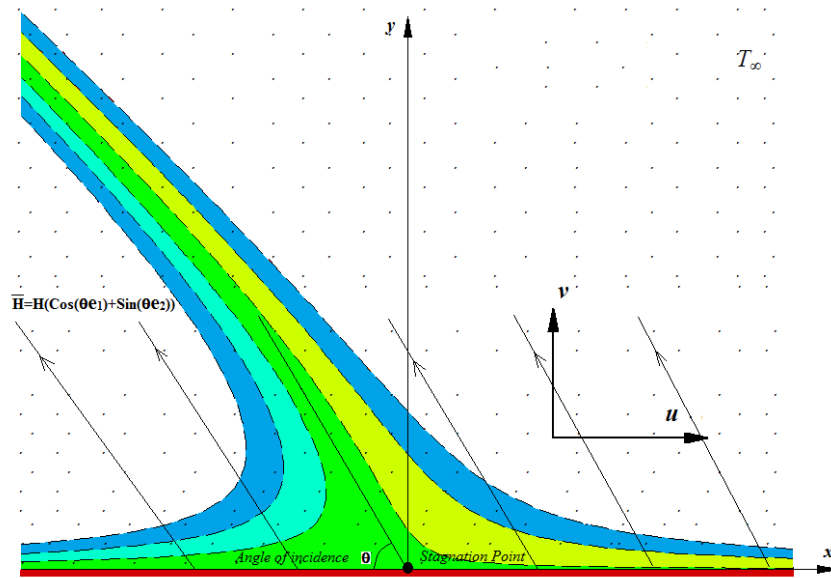


Fig. 2. 1. Geometry of the problem

2.2 Problem description and governing equations

Consider the problem of stagnation point flow over an oscillatory surface with velocity $U_0 \cos \omega \bar{t}$. The \bar{x} -coordinate is taken horizontally and the \bar{y} -coordinate is considered perpendicular to horizontal direction and is pointed in outward direction towards the fluid as shown in **Fig. 2.1**. It is assumed that the fluid impinges obliquely to the oscillatory surface. The governing equations of fluid flow can be written as

$$\begin{aligned} \mu_{nf} \bar{\nabla}^2 \bar{\mathbf{V}} - \rho_{nf} \frac{\partial \bar{\mathbf{V}}}{\partial \bar{t}} - (\bar{\mathbf{V}} \cdot \bar{\nabla}) \bar{\mathbf{V}} + \mu_e (\bar{\mathbf{V}} \times \bar{\mathbf{H}}) \times \bar{\mathbf{H}} + \bar{\nabla} \bar{p} &= 0, \\ \alpha_{nf} \bar{\nabla}^2 \bar{T} - \frac{\partial \bar{T}}{\partial \bar{t}} - (\bar{\mathbf{V}} \cdot \bar{\nabla}) \bar{T} &= 0, \\ \bar{\nabla} \times \bar{\mathbf{H}} &= \sigma_e (\bar{\mathbf{E}} + \mu_e \bar{\mathbf{V}} \times \bar{\mathbf{H}}), \\ \bar{\mathbf{V}} \cdot \bar{\mathbf{V}} = 0, \quad \bar{\mathbf{V}} \cdot \bar{\mathbf{H}} = 0, \quad \bar{\mathbf{V}} \times \bar{\mathbf{E}} = \mathbf{0}, \quad \bar{\mathbf{V}} \cdot \bar{\mathbf{E}} = 0, \end{aligned} \quad (2.1)$$

where μ_{nf} , ρ_{nf} and α_{nf} are defined in **Table 1.1**. $\bar{\mathbf{H}}$ and $\bar{\mathbf{E}} = \mathbf{0}$ are the magnetic and electric fields and are defined as

$$\bar{\mathbf{H}} = H(\cos \vartheta \mathbf{i} + \sin \vartheta \mathbf{j}), \vartheta = \arctan(-2a/b)$$

Consider the boundary conditions to system (2.1) as

$$\left. \begin{aligned} \bar{v} = 0, \quad \bar{u} - \lambda_1 \frac{\mu_{nf}}{\mu_f} \frac{\partial \bar{u}}{\partial \bar{y}} = U \cos \omega \bar{t}, \\ \bar{T} - \lambda_2 \frac{k_{nf}}{k_f} \frac{\partial \bar{T}}{\partial \bar{y}} = \bar{T}_w + \epsilon (\bar{T}_w - \bar{T}_\infty) \text{Re}[e^{i\omega \bar{t}}] \end{aligned} \right\} \text{at } \bar{y} = 0 \quad (2.2)$$

$$\bar{v} = -a\bar{y}, \quad \bar{u} = a\bar{x} + b\bar{y}, \quad \bar{T} = \bar{T}_\infty \quad \text{as } \bar{y} \rightarrow \infty,$$

where λ_1 and λ_2 are the velocity slip and thermal jump parameters.

The free stream velocities in system (2.2) shows that the streamlines are hyperbolas. The asymptotes of these stream lines, also known as degenerate streamlines, can be obtained from the free stream velocities as

$$\bar{y} = 0 \quad \text{and} \quad \bar{y} = -\frac{2a}{b} \bar{x}. \quad (2.3)$$

We consider a more general case of free stream that the fluid imping obliquely on the plane

$\bar{y} = A$ by letting

$$\forall \bar{x} \in \mathbb{R} \text{ and } \bar{y} \geq A \Rightarrow \bar{v} = -a(\bar{y} - A), \quad \bar{u} = a\bar{x} + b(\bar{y} - B),$$

The stagnation point become in this case is $(b(B - A)/a, A)$ and the asymptotes of the hyperbolic streamlines are

$$\bar{y} = A$$

And

$$\bar{y} = -\frac{2a}{b}\bar{x} + 2B - A.$$

Further [73] stated that “the oblique stagnation point flow exists if, and only if, the external magnetic field is parallel to the dividing streamline” and shown that

$$\bar{\mathbf{H}}_0 = \frac{H_0(-b\hat{\mathbf{i}} + 2a\hat{\mathbf{j}})}{\sqrt{4a^2 + b^2}}. \quad (2.4)$$

After neglecting the induced magnetic and electric field, we can write

$$(\bar{\mathbf{V}} \times \bar{\mathbf{H}}) \times \bar{\mathbf{H}} \cong \sigma_e \mu_e (\bar{\mathbf{V}} \times \bar{\mathbf{H}}_0) \times \bar{\mathbf{H}}_0, \quad (2.5)$$

and by assuming

$$\bar{v} = -a\bar{f}(\bar{y}), \quad \bar{u} = a\bar{x}\bar{f}'(\bar{y}) + b\bar{g}(\bar{y}, \bar{t}), \quad (2.6)$$

the Eqs. (2.1)_{1,2} and (2.2) reduce to

$$\begin{aligned} & a\bar{x} \left[a\bar{f}'^2 - a\bar{f}\bar{f}'' - v_{nf}\bar{f}''' + 4a^2 \frac{\sigma_f}{\rho_{nf}} \frac{B_0^2}{4a^2 + b^2} \bar{f}' \right] \\ & + b \left[\bar{g}_{\bar{t}} + a(\bar{g}\bar{f}' - \bar{f}\bar{g}') - v_{nf}\bar{g}'' \right. \\ & \left. + 2a^2 \frac{\sigma_f}{\rho_{nf}} \frac{B_0^2}{4a^2 + b^2} (2\bar{g} - \bar{f}) \right] = -\frac{1}{\rho_{nf}} \frac{\partial \bar{p}}{\partial \bar{x}}, \end{aligned} \quad (2.7)$$

$$a^2 \bar{f} \bar{f}' + v_{nf} a \bar{f}'' + \frac{\sigma_f}{\rho_{nf}} \frac{B_0^2}{4a^2 + b^2} (2a^2 b \bar{x} \bar{f}' + ab^2 (2\bar{g} - \bar{f})) = -\frac{1}{\rho_{nf}} \frac{\partial \bar{p}}{\partial \bar{y}}, \quad (2.8)$$

$$\begin{aligned}
\bar{p}_0 - \bar{p}(\bar{x}, \bar{y}) = \rho_{nf} & \left[v_{nf} a \bar{f}' + \frac{a^2}{2} \left(\bar{x}^2 - 2 \frac{b}{a} (B - A) \bar{x} + \bar{f}^2 \right) \right. \\
& + \frac{\sigma_f}{\rho_{nf}} \frac{B_0^2}{4a^2 + b^2} \left\{ 2a^3 \left(\bar{x}^2 - 2 \frac{b}{a} (B - A) \bar{x} \right) + 2a^2 b \bar{x} \bar{f} \right. \\
& \left. \left. + ab^2 \int_0^{\bar{y}} \left(2\bar{g}(\bar{s}, \bar{t}) - \bar{f}(\bar{s}) \right) d\bar{s} \right\} \right]. \quad (2.13)
\end{aligned}$$

In Eq. (2.13), \bar{p}_0 is the stagnation pressure and represent that it is the maximum pressure throughout the field. By using Eq. (2.13), Eqs. (2.7)-(2.9) takes the form

$$\left. \begin{aligned}
\frac{1}{a} v_{nf} \bar{f}'''' + \bar{f} \bar{f}'' - \bar{f}'^2 - \frac{\sigma_f}{\rho_{nf}} \frac{4aB_0^2}{4a^2 + b^2} \bar{f}' &= -\frac{\sigma_f}{\rho_{nf}} \frac{4aB_0^2}{4a^2 + b^2} - 1 \\
\frac{1}{a} v_{nf} \bar{g}'' + \bar{f} \bar{g}' - \bar{g} \bar{f}' + \frac{\sigma_f}{\rho_{nf}} \frac{4aB_0^2}{4a^2 + b^2} (\bar{f} - \bar{g}) - \frac{1}{a} \bar{g}_{\bar{t}} &= \\
\left(1 + \frac{\sigma_f}{\rho_{nf}} \frac{4aB_0^2}{4a^2 + b^2} \right) (B - A). &
\end{aligned} \right\} \quad (2.14)$$

The following similarity variables are presented to make simpler the mathematical analysis of the problem

$$\left. \begin{aligned}
y = \sqrt{\frac{a}{v_f}} \bar{y}, f(y) = \sqrt{\frac{a}{v_f}} \bar{f} \left(\sqrt{\frac{v_f}{a}} y \right), \quad t = \omega \bar{t}, \\
g(y, t) = \sqrt{\frac{a}{v_f}} \bar{g} \left(\sqrt{\frac{v_f}{a}} y, \frac{t}{\omega} \right) = g_0(y) + \varepsilon g_1(y) e^{it}, \\
\theta(y, t) = \frac{T - T_\infty}{T_w - T_\infty} = \theta_0(y) + \varepsilon \theta_1(y) e^{it}.
\end{aligned} \right\} \quad (2.15)$$

Using the above similarity variables, Eqs. (2.7)-(2.8) together with (2.9) (2.1)₂ and (2.2)_{3,6} reduce to

$$\begin{aligned}
\frac{\mu_{nf}}{\mu_f} \frac{\rho_f}{\rho_{nf}} g_0'' + f g_0' - g_0 f' + \frac{\rho_f}{\rho_{nf}} M^2 (f - g_0) - \left(1 + \frac{\rho_f}{\rho_{nf}} M^2\right) (\mathbb{B} - \mathbb{A}) &= 0, \\
\frac{\mu_{nf}}{\mu_f} \frac{\rho_f}{\rho_{nf}} f''' + f f'' - f'^2 + 1 + \frac{\rho_f}{\rho_{nf}} M^2 (1 - f') &= 0, \\
\frac{\mu_{nf}}{\mu_f} \frac{\rho_f}{\rho_{nf}} g_1'' + f g_1' - g_1 f' - \frac{\rho_f}{\rho_{nf}} M^2 g_1 - i\Omega g_1 &= 0, \\
\frac{k_{nf}}{k_f} \theta_0'' + Pr \frac{(\rho C_p)_{nf}}{(\rho C_p)_f} f \theta_0' &= 0,
\end{aligned} \tag{2.16}$$

$$\begin{aligned}
\frac{1}{Pr} \frac{k_{nf}}{k_f} \theta_1'' + Pr \frac{(\rho C_p)_{nf}}{(\rho C_p)_f} f \theta_1' - i\Omega Pr \frac{(\rho C_p)_{nf}}{(\rho C_p)_f} \theta_1 &= 0, \\
f(0) = 0, \quad f'(0) - \frac{\mu_{nf}}{\mu_f} N_1 f''(0) = 0, \quad g_0(0) - \frac{\mu_{nf}}{\mu_f} N_1 g_0'(0) = 0, \\
g_1(0) - \frac{\mu_{nf}}{\mu_f} N_1 g_1'(0) = 1, \\
\theta_0(0) - \frac{k_{nf}}{k_f} N_2 \theta_0'(0) = 1, \quad \theta_1(0) - \frac{k_{nf}}{k_f} N_2 \theta_1'(0) = 1, \\
g_0'(y) = 1, \quad f'(y) = 1, \quad g_1(y) = 0, \quad \theta_1(y) = 0, \quad \theta_0(y) = 0, \quad y \rightarrow \infty, \\
g_0(y) = y - \mathbb{B}, \quad f(y) = y - \mathbb{A}, \quad \text{as } y \rightarrow \infty,
\end{aligned} \tag{2.17}$$

where

$$\begin{aligned}
\mathbb{B} &= \sqrt{\frac{a}{v_f}} B, \quad \mathbb{A} = \sqrt{\frac{a}{v_f}} A, \quad N_2 = \lambda_2 \sqrt{\frac{a}{v_f}}, \quad N_1 = \lambda_1 \sqrt{\frac{a}{v_f}}, \\
M^2 &= 4a \frac{\sigma_f}{\rho_f} \frac{B_0^2}{4a^2 + b^2}, \quad \Omega = \frac{\omega}{a}, \quad Pr = \frac{v_f}{\alpha}, \quad \epsilon = \sqrt{\frac{a}{v_f}} \frac{U}{b},
\end{aligned} \tag{2.18}$$

where N_1 and N_2 are the velocity slip and thermal jump parameters.

Furthermore, the skin-friction coefficient (C_f), local wall shear stress τ_w , local Nusselt number (Nu) and surface heat flux q_w are defined as

$$\begin{aligned}
C_f &= \frac{\tau_w}{\frac{1}{2} \rho_f U_w^2}, \\
Nu &= \frac{\bar{x} q_w}{k_f (\bar{T}_w - \bar{T}_\infty)},
\end{aligned}$$

$$\tau_w = \left[\mu_{nf} \frac{\partial \bar{u}}{\partial \bar{y}} \right]_{\bar{y}=0},$$

$$q_w = -k_{nf} \frac{\partial \bar{T}}{\partial \bar{y}} \Big|_{\bar{y}=0}.$$

By making use of (2.15), the above equations reduced

$$\frac{1}{2} Re_{\bar{x}} C_f = \frac{\mu_{nf}}{\mu_f} \left[\sqrt{Re_x} f''(0) + \frac{b}{a} (g_0'(0) + \epsilon g_1'(0) e^{it}) \right]$$

$$\frac{Nu}{\sqrt{Re_{\bar{x}}}} = -\frac{k_{nf}}{k_f} \theta_0'(0) - \frac{k_{nf}}{k_f} \epsilon \theta_1'(0) e^{it},$$

At the surface $\bar{y} = 0$, three points carry significant importance: the stagnation point towards which the separating streamline far away from the surface are directed, the position where maximum pressure is exerted $\bar{x} = \bar{x}_p$, and the position of zero tangential stress $\bar{x} = \bar{x}_s$. The equation of separating streamline which intersect the boundary is

$$x = \sqrt{\frac{a}{v_f}} \bar{x}, \quad x f(y) + \frac{b}{a} \int_0^y (g_0(s) + \epsilon e^{it} g_1(s)) ds = 0. \quad (2.19)$$

From Eq. (2.13) and wall shear stress, we see that

$$\begin{aligned} \bar{x}_p &= \frac{b}{a} \left(\frac{v_f}{a} \right)^{1/2} (\mathbb{B} - \mathbb{A}) \\ \bar{x}_s &= -\frac{b}{a} \left(\frac{v_f}{a} \right)^{1/2} \frac{[g_0'(0) + \epsilon g_1'(0) e^{it}]}{f''(0)} \end{aligned} \quad (2.20)$$

We note that \bar{x}_p does not depend on M^2 and the ratio

$$\frac{\bar{x}_p}{\bar{x}_s} = -(\mathbb{B} - \mathbb{A}) \frac{f''(0)}{[g_0'(0) + \epsilon g_1'(0) e^{it}]}$$

is same for all angles of incidence.

2.3 Solution procedure

Numerical solutions of (2.16)₁ and (2.17)_{1,2,7,12} have been solved numerically by means of midpoint method with Richardson extrapolation enhancement. Notice that we have coupled system of governing equations in which $f(y)$ is coupled in $\theta_0(y), g_0(y), \theta_1(y)$ and $g_1(y)$ but not vice versa. Thus, we can find the solution for $g_0(y)$ -flow as

$$g_0(y) = C_1 f'' + C_2 f'' \Delta(y) + (\mathbb{A} - \mathbb{B}) f' + g_{0p}(y),$$

with

$$C_1 = N_1 \frac{\mu_{nf}}{\mu_f} \frac{g'_0(0)}{f''(0)} + (\mathbb{B} - \mathbb{A}) \frac{f'(0)}{f''(0)},$$

$$C_2 = N_1 \frac{\mu_{nf}}{\mu_f} g'_0(0) (f''(0))^{2\frac{v_f}{v_{nf}}} + (\mathbb{B} - \mathbb{A}) f'(0) (f''(0))^{2\frac{v_f}{v_{nf}}},$$

$$\Delta(y) = \int_0^y (f''(s))^{-2\frac{v_f}{v_{nf}}} \cdot \text{Exp} \left(-\frac{v_f}{v_{nf}} \int_0^s f(\eta) d\eta \right) ds,$$

$$g_{0p}(y) = \frac{\rho_f}{\rho_{nf}} M^2 f''(y) \left\{ \begin{array}{l} \int_0^y \Delta(s) \cdot f(s) (f''(s))^{(2\frac{v_f}{v_{nf}}-1)} \cdot \text{Exp} \left(\frac{v_f}{v_{nf}} \int_0^s f(\eta) d\eta \right) ds \\ -\Delta(y) \int_0^y f(s) (f''(s))^{(2\frac{v_f}{v_{nf}}-1)} \cdot \text{Exp} \left(\frac{v_f}{v_{nf}} \int_0^s f(\eta) d\eta \right) ds \end{array} \right\}$$

Furthermore, the series solutions of equation (2.16)₃ and (2.16)₅ for small value of Ω have been obtained

$$g_1(y) = \sum_{n=0}^{\infty} (i\Omega)^n \phi_n(y).$$

$$\theta_1(y) = \sum_{n=0}^{\infty} (i\Omega)^n \theta_{1n}(y).$$

In present problem, the real part of solutions is

$$\left. \begin{array}{l} g_1(y) = \phi_0(y) - \Omega^2 \phi_2(y) + \Omega^4 \phi_4(y) \dots \\ \theta_1(y) = \theta_{10}(y) - \Omega^2 \theta_{12}(y) + \Omega^4 \theta_{14}(y) \dots \end{array} \right\}$$

where

$$\left. \begin{aligned} \frac{\mu_{nf}}{\mu_f} \frac{\rho_f}{\rho_{nf}} \phi_0'' + f \phi_0' - \phi_0 f' - \frac{\rho_f}{\rho_{nf}} M^2 \phi_0 &= 0 \\ \frac{\mu_{nf}}{\mu_f} \frac{\rho_f}{\rho_{nf}} \phi_m'' + f \phi_m' - \phi_m f' - \frac{\rho_f}{\rho_{nf}} M^2 \phi_m &= \phi_{m-1} \\ \phi_0(0) - N_1 \frac{\mu_{nf}}{\mu_f} \phi_0'(0) &= 1, \quad \phi_0(\infty) = 0 \\ \phi_m(0) - N_1 \frac{\mu_{nf}}{\mu_f} \phi_m'(0) &= 0, \quad \phi_m(\infty) = 0 \end{aligned} \right\}, \quad m = 1, 2, 3 \dots$$

and

$$\left. \begin{aligned} \frac{k_{nf}}{k_f} \theta_{1n}'' + Pr \frac{(\rho C_p)_{nf}}{(\rho C_p)_f} f \theta_{1n}' - Pr \frac{(\rho C_p)_{nf}}{(\rho C_p)_f} \theta_{1(n-1)} &= 0 \\ \theta_{1n}(0) - N_2 \frac{k_{nf}}{k_f} \theta_{1n}'(0) &= 0, \quad \theta_{1n}(\infty) = 0 \end{aligned} \right\}, \quad n = 1, 2, 3 \dots$$

in which $\theta_{10}(y) = \theta_0(y)$ which can be obtained from (2.16)₄

$$\theta_0(y) = \frac{1}{J_{nf}(\infty, Pr) + N_2 \frac{k_{nf}}{k_f}} \left(J_{nf}(\infty, Pr) - J_{nf}(y, Pr) \right)$$

where

$$J_{nf}(y, Pr) = \int_0^y \text{Exp} \left(-\frac{k_f}{k_{nf}} \frac{(\rho C_p)_{nf}}{(\rho C_p)_f} Pr \int_0^s f(\eta) d\eta \right) ds$$

and

$$J_{nf}(\infty, Pr) = \lim_{y \rightarrow \infty} J_{nf}(y, Pr).$$

The above systems have been solved numerically using midpoint method with Richardson extrapolation enhancement and the numerical integration for $g_0(y)$ and $\theta_0(y)$ can be executed easily with aid of any mathematical software.

2.4 Results and Discussion

The numerical results of the modeled equations are obtained for three types of different nanoparticles namely Titania (TiO_2), Alumina (Al_2O_3) and copper (Cu) having water as a base fluid and the thermophysical properties of nanoparticles and base fluid are given in **Table 1.2**.

The solid volume fraction φ of the nanoparticles represent up to what fraction of whole liquid, solid concentrations are incorporated. Keeping the fluid nature of base material, it is kept less than 0.2. We have used constant Prandtl number for water, $Pr = 6.2$, throughout in computation. The values of the skin friction components and boundary layer thickness are obtained and compared with previously published results [73] as given in **Table 2.1,2.2**. It is seen that the comparison is in good agreement and thus gives us confidence to the accuracy of the numerical results presented in this chapter.

We illustrate the effects of the parameters M, φ, N_1, N_2 and Ω on dimensionless stream-function, velocity profile, temperature profile, velocity gradient at the surface, temperature gradient at the surface and boundary layer thickness. Generally, the flow over an oscillatory surface is driven by the combine effect of free stream parameter and magnetic field. **Fig 2.2** shows that normal component of velocity profile satisfies the boundary constrains which also shows validity of obtained results. Furthermore, from this figure, we depict that $f(y) = y - 0.393589$ and the velocity gradient decreases gradually when it goes far away from the surface. The maximum value of velocity gradient is found at the surface and from this figure we illustrate that $f''(0) = 2.346663$. The steady part of shear velocity $g_0(y)$ changes its direction for positive and negative values of $\mathbb{B} - \mathbb{A}$ and the same behavior is seen for $g_0'(y)$ as shown in **Fig. 2.3**. Furthermore, the magnitude of $g_0(y)$ is gradually increase whenever it achieves the free stream $g_0(y) = y - \mathbb{B}$. The normal velocity component $f'(y)$ increases against both parameters M and N_1 whereas the boundary layer thickness decreases. **Figs. 2.5** shows the effects of different involved flow parameters M, N_1 and $\mathbb{B} - \mathbb{A}$ on the steady part of shear flow $g_0(y)$ and its gradient $g_0'(y)$. **Fig. 2.6** depicts velocity profile $u(y, t)$ in the unsteady domain. Generally, free stream velocity drives the flow due to the plate oscillation. At the plate nanofluid velocity is minimum and gradually it approaches the free stream velocity. It observes that the amplitude of oscillation is maximum at the surface and regularly

increase until it achieves the free stream velocity. We know that temperature equation does not influence the momentum equations therefore, the effects of thermal jump parameter N_2 does not affect the velocity components and hence velocity components are identical against thermal jump parameter N_2 . Moreover, the thermal boundary layer thickness decreases for higher values of M and N_2 as shown in **Fig. 2.7**. **Fig. 2.8** are plotted for stream lines in the case of impinging fluid at different angles $\mathbb{B} - \mathbb{A}$ and Hartmann number M . It intersects the wall $y = 0$ at the point \bar{x}_s , which is the point of zero skin friction. The location of this point depends on $\mathbb{B} - \mathbb{A}$ and we observed that for positive values of $\mathbb{B} - \mathbb{A}$, the stagnation point appears at the right side of the plate from the origin whereas the opposite can be seen for negative values of $\mathbb{B} - \mathbb{A}$. **Fig. 2.9** is constructed for the comparison of different nanoparticles. These results show that Alumina (Al_2O_3) are definitely small, while Titania (TiO_2) and copper (Cu) distinctly under estimate the Nusselt number. The numerical values of skin friction coefficient components and Nusselt number components are given in **Table 2.3-2.6**. From these tables we observed that momentum boundary layer thickness decreases against all physical involved parameters whereas Al_2O_3 produce highest value of boundary layer and Cu has the lowest. The values of $f''(0)$ increases for higher values of M and decreases against velocity slip parameter N_1 . Also, the values of $f''(0)$ is maximum for $Cu - water$ nanofluids and minimum for $Al_2O_3 - water$ nanofluids. From **Table 2.4** we observed that the values of steady part of shear component $g_0'(0)$ change its sign against $\mathbb{B} - \mathbb{A}$ that is for $\mathbb{B} - \mathbb{A} < 0$ the values of $g_0'(0)$ are positive and for $\mathbb{B} - \mathbb{A} > 0$ it is negative. It is due the change of direction of velocity profile for $\mathbb{B} - \mathbb{A} \geq 0$. Furthermore, the values of $g_0'(0)$ decreases for higher values of M and N_1 . Also, $g_0'(0)$ is maximum in the case of $Cu - water$ and minimum for $Al_2O_3 - water$. **Table 2.5(a, b)** represents the values of $\phi_0'(0)$, $\phi_2'(0)$ and $\phi_4'(0)$ for

different values M , φ and N_1 . **Table 2.6(a, b)** shows that Nusselt number enhance against the Hartmann number M and reduce for higher values of N_2 and φ . Also $Cu - water$ produce the highest Nusselt number whereas $Al_2O_3 - water$ produce the lowest.

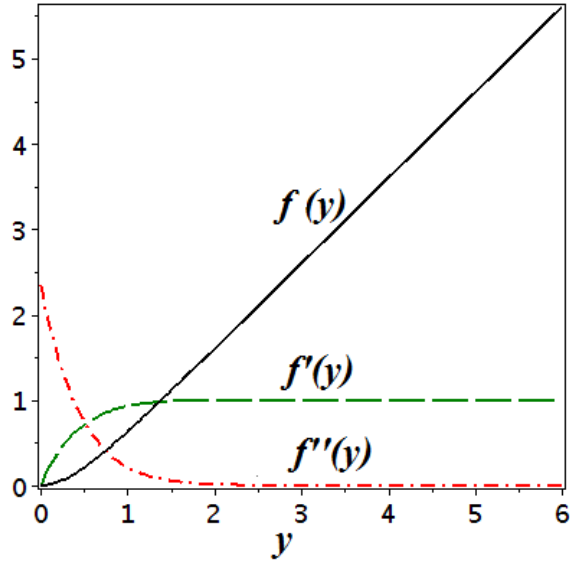


Fig. 2. 2. $f(y)$, $f'(y)$, $f''(y)$ when $M = 2$, $N_1 = 0.0$, $\varphi = 0.0$,

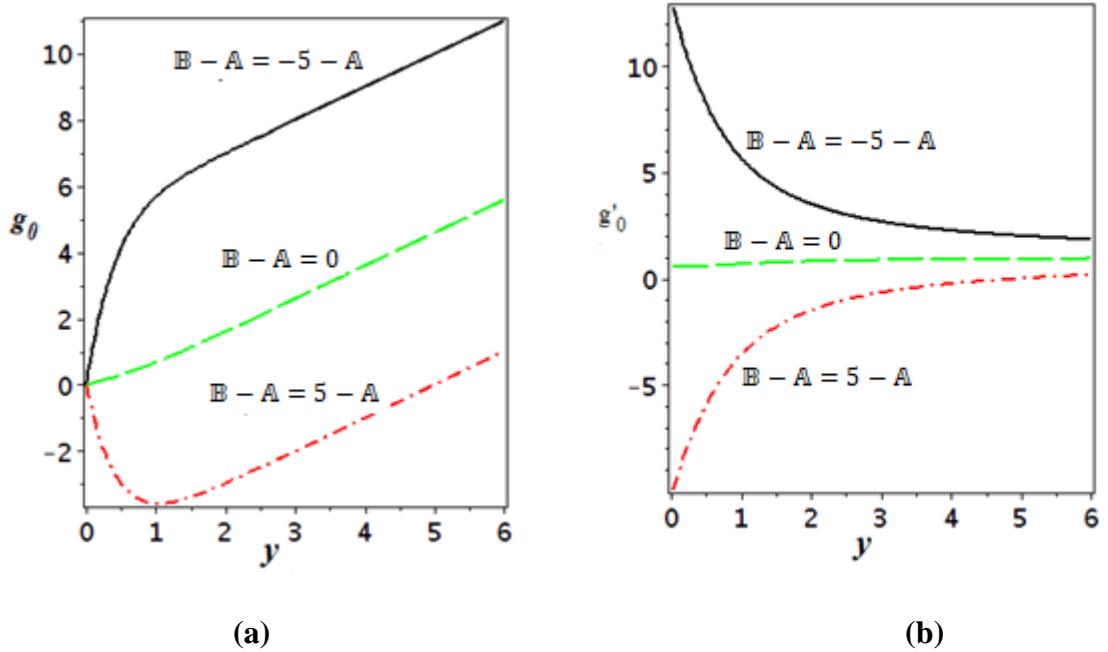
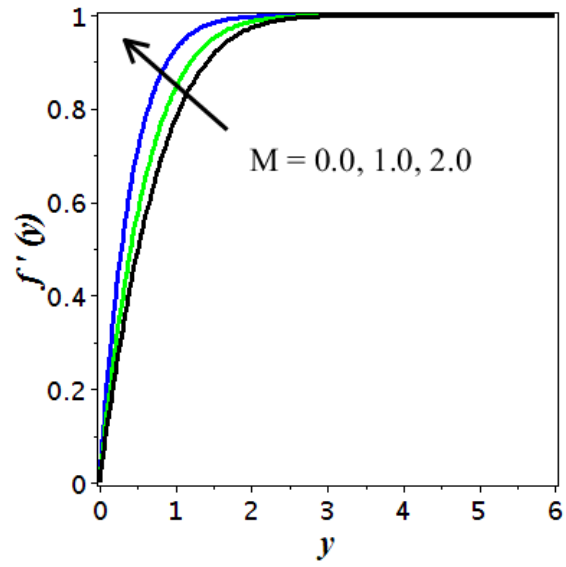
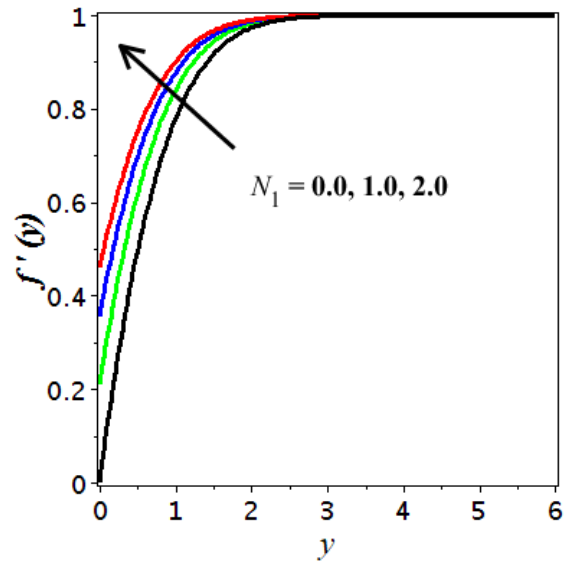


Fig. 2. 3. $g_0(y)$, $g_0'(y)$ for different $B - A$ when $M = 2$, $N_1 = 0.0$, $\varphi = 0.0$.

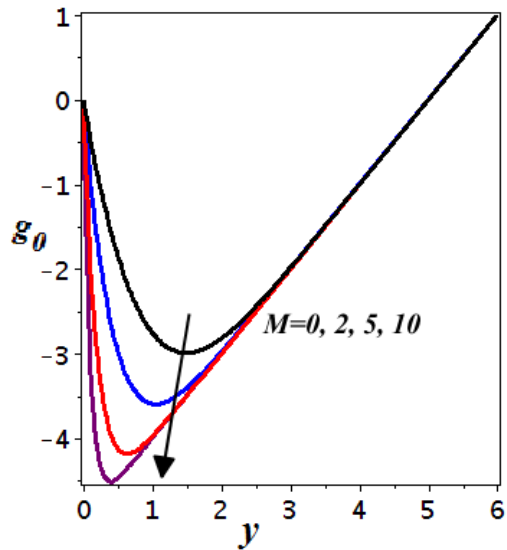


(a)

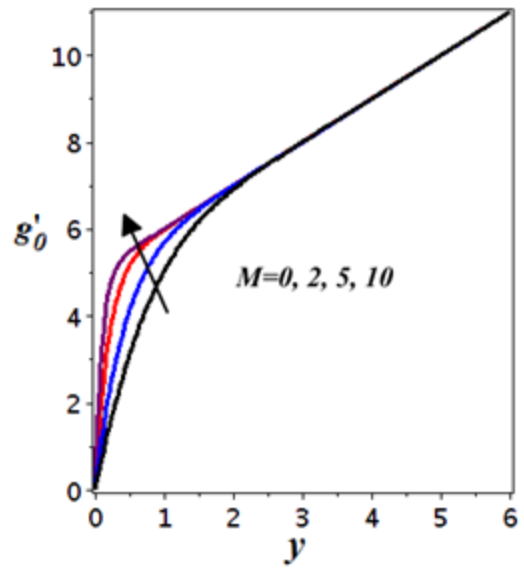


(b)

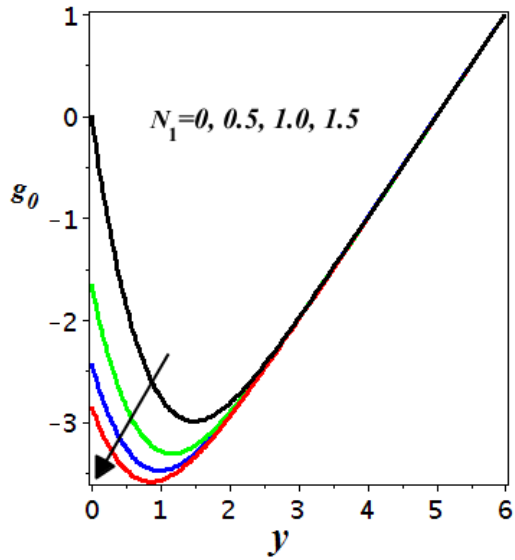
Fig. 2. 4. Influence of $f'(y)$, (a) $\varphi = 0.0, N_1 = 0.0$ and (b) $M = 0, \varphi = 0.0$



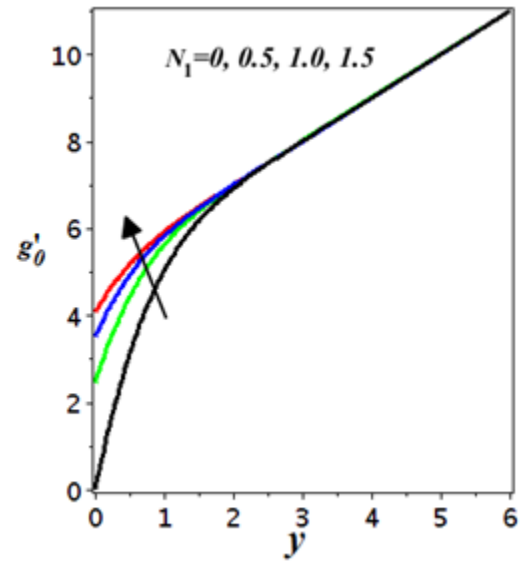
(a)



(b)



(c)



(d)

Fig. 2. 5. Influence of $g_0(y)$ and $g'_0(y)$ (a)-(b) $\varphi = 0.0, N_1 = 0.0$ and (c)-(d) $\varphi = 0.0, M = 0.0$.

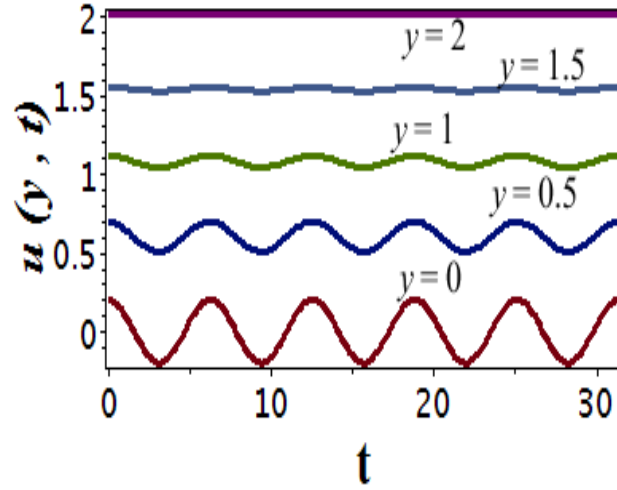


Fig. 2. 6. Time dependent flow $u(y, t)$ at different locations from the surface when $\varphi = 0.1, N_1 = 0.0, M = 1.0, \varepsilon = 0.2, \Omega = 0.2, \mathbb{B} - \mathbb{A} = -\mathbb{A}, x = 1$.

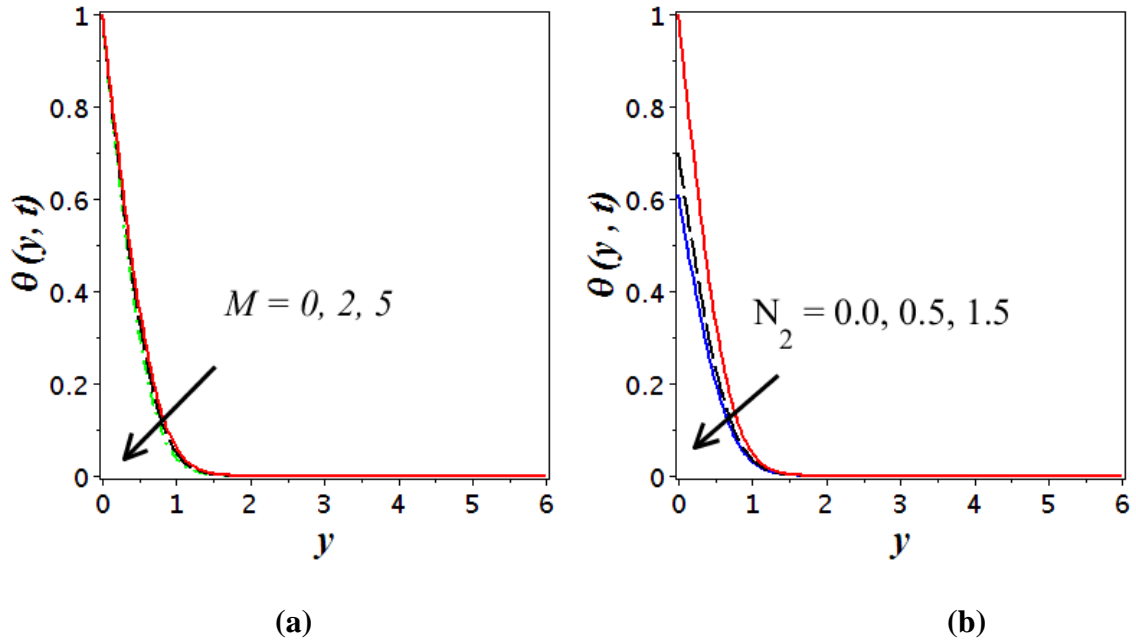
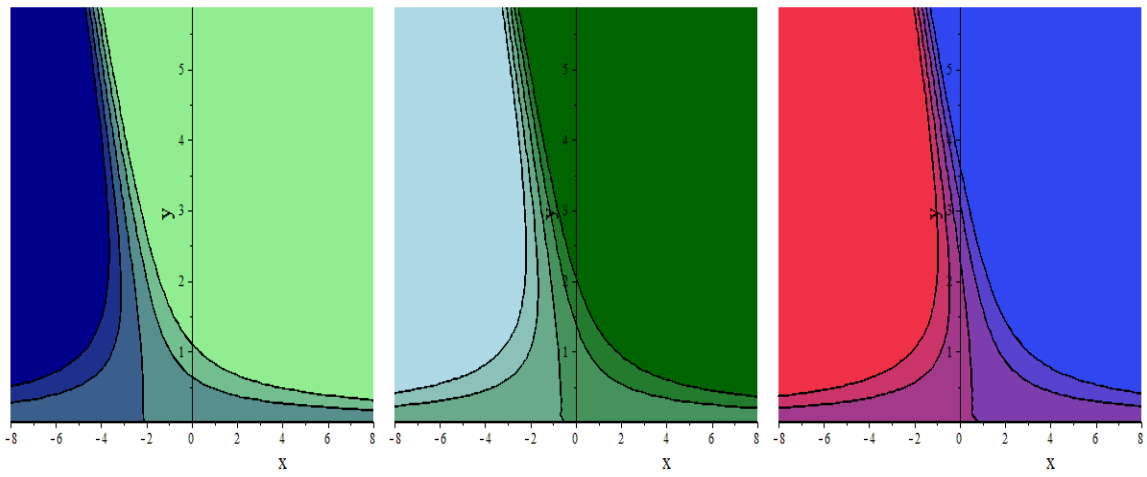


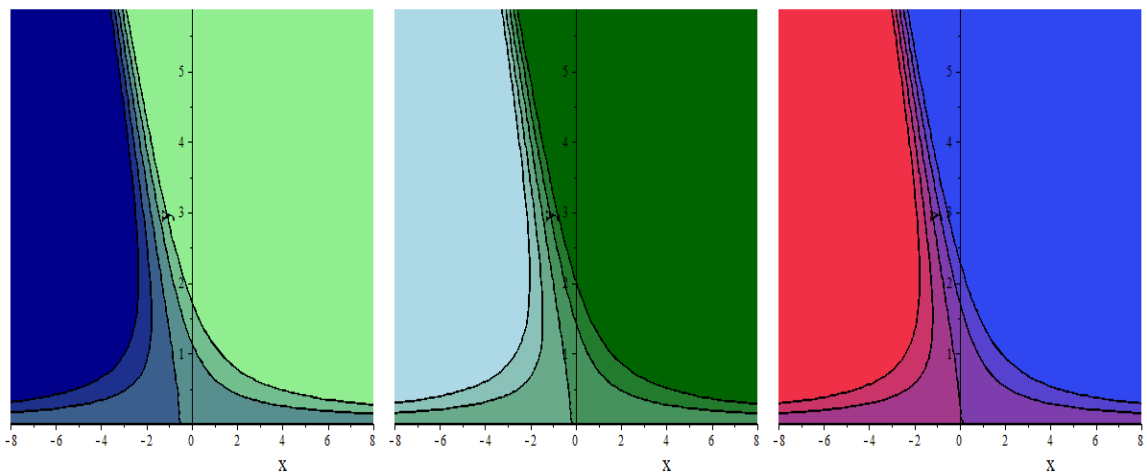
Fig. 2. 7. Variation of $\theta(y, t)$ (a) $\varphi = 0.1, N_2 = 0.0, N_1 = 0.5, \varepsilon = 0.0$ and (b) $\varphi = 0.1, M = 2.0, N_1 = 0.5, \varepsilon = 0.0$.



(a)

(b)

(c)



(d)

(e)

(f)

Fig. 2.8. Streamlines pattern for *Cu – Water* nanofluid when $t = 0, \frac{b}{a} = 1, \Omega = 0.5, N_1 = 0.5, \varepsilon = 0.2$ for $\mathbb{B} - \mathbb{A} = -5\mathbb{A}, 0, 5\mathbb{A}$ respectively. (a), (b), (c) for $M = 1$ and (d), (e), (f) for $M = 5$.

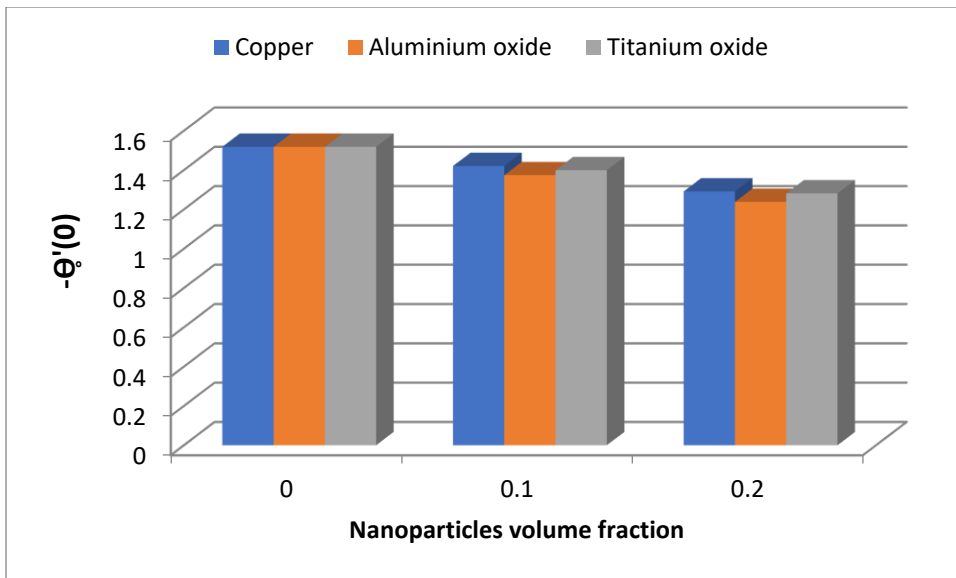


Fig. 2. 9. Bar graph comparison of various nanoparticles.

Table. 2. 1. Validation of results for $f''(0)$ and \mathbb{A} when $\varphi = 0$ and $N_1 = 0$.

M	$f''(0)$		\mathbb{A}	
	Present results	[73]	Present results	[73]
0	1.232588	1.2326	0.647901	0.6479
1	1.585331	1.5853	0.541007	0.5410
2	2.346663	2.3467	0.393589	0.3936
5	5.147964	5.1480	0.190729	0.1907
10	10.074741	10.0747	0.098774	0.0988

Table. 2. 2. Validation of results for $g_0'(0)$ when $\varphi = 0$ and $N_1 = 0$.

M	$\mathbb{B} - \mathbb{A}$	$g_0'(0)$	
		[73]	Present results
0	$-\mathbb{A} = -0.647901$	1.4065	1.406545
	0	0.6080	0.607950
	$\mathbb{A} = 0.647901$	0.1906	-0.190645
1	$-\mathbb{A} = -0.541007$	1.4240	1.423990
	0	0.5663	0.566316
	$\mathbb{A} = 0.541007$	-0.2913	-0.291360
2	$-\mathbb{A} = -0.393589$	1.4541	1.454064
	0	0.5304	0.530442
	$\mathbb{A} = 0.393589$	-0.3932	-0.393181
5	$-\mathbb{A} = -0.190729$	1.4880	1.488171
	0	0.5063	0.506303
	$\mathbb{A} = 0.190729$	-0.4754	-0.475564
10	$-\mathbb{A} = -0.098774$	1.4970	1.496769
	0	0.5016	0.501643
	$\mathbb{A} = 0.098774$	-0.4937	-0.493483

Table. 2. 3. $f''(0)$ and \mathbb{A} for different values of N_1, M, φ and nanoparticles.

φ	M	N_1	Al_2O_3 -Water nanofluid		Cu -Water nanofluid		TiO_2 -Water nanofluid	
			$f''(0)$	\mathbb{A}	$f''(0)$	\mathbb{A}	$f''(0)$	\mathbb{A}
0.0	0.0	0.0	1.232587	0.647900	1.232587	0.647900	1.232587	0.647900
0.1			1.231074	0.648697	1.447977	0.551523	1.244317	0.641792
0.2			1.178253	0.677777	1.501345	0.531918	1.198801	0.666160
0.1	1.0		1.509640	0.561376	1.691074	0.494686	1.520451	0.556870
	5.0		4.550725	0.214712	4.613509	0.210182	4.554289	0.214448
	10.0		8.850999	0.112272	8.883376	0.111603	8.852829	0.112233
	1.0	0.5	0.801948	0.246579	0.851419	0.200339	0.805091	0.243368
		1.0	0.531899	0.154881	0.552730	0.122968	0.533255	0.152631
		1.5	0.396376	0.112573	0.407669	0.088472	0.397119	0.110861

Table. 2. 4. $g_0'(0)$ and $\mathbb{B} - \mathbb{A}$ for different values of N_1, φ, M and nanoparticles

N_1	M	φ	Cu -Water nanofluid		Al_2O_3 -Water nanofluid		TiO_2 -Water nanofluid	
			$\mathbb{B} - \mathbb{A}$	$g_0'(0)$	$\mathbb{B} - \mathbb{A}$	$g_0'(0)$	$\mathbb{B} - \mathbb{A}$	$g_0'(0)$
0.0	0.0	0.0	-	1.406544	-	1.406544	-	1.406544
			0.647900	0.607950	0.647900	0.607950	0.647900	0.607950
			0	0.607950	0	0.607950	0	0.607950
		0.1	0.647900	-	0.647900	-	0.647900	-
				0.190644		0.190644		0.190644
		0.2	-	1.406544	-	1.406544	-	1.406544
			0.531918	0.607949	0.677777	0.607950	0.666160	0.607950
			0	0.607949	0	0.607950	0	0.607950
		0.1	0.531918	-	0.677777	-	0.666160	-
				0.190644		0.190643		0.190643
	1.0	0.1	-	1.416619	-	1.420283	-	1.420010
			0.494686		0.561376		0.556870	

			0	0.580068	0	0.572806	0	0.573315
			0.494686	- 0.256482	0.561376	- 0.274670	0.556870	- 0.273379
	5.0		- 0.210182	1.480522	- 0.214712	1.485147	- 0.214448	1.484872
			0	0.510844	0	0.508050	0	0.508212
			0.210182	- 0.458832	0.214712	- 0.469045	0.214448	- 0.468447
	10.0		- 0.111603	1.494335	- 0.112272	1.495843	- 0.112233	1.495757
			0	0.502917	0	0.502124	0	0.502169
			0.111603	- 0.488500	0.112272	- 0.491595	0.112233	- 0.491419
0.5	1.0		- 0.200339	0.580021	- 0.246579	0.621280	- 0.243368	0.618665
			0	0.409448	0	0.423537	0	0.422731
			0.200339	0.238875	0.246579	0.225793	0.243368	0.226798
1.0			- 0.122968	0.355580	- 0.154881	0.388140	- 0.152631	0.386037
			0	0.287611	0	0.305759	0	0.304646
			0.122968	0.219643	0.154881	0.223378	0.152631	0.223254
1.5			- 0.088472	0.255542	- 0.112573	0.281223	- 0.110861	0.279551
			0	0.219474	0	0.236602	0	0.235525
			0.088472	0.183407	0.112573	0.191980	0.110861	0.191500

Table. 2. 5(a). Numerical values of $-\phi_0'(0)$, $\phi_2'(0)$ and $\phi_4'(0)$.

N_1	M	φ	<i>Cu</i> -Water nanofluid			Al_2O_3 -Water nanofluid		
			$-\phi_0'(0)$	$\phi_2'(0)$	$\phi_4'(0)$	$-\phi_0'(0)$	$\phi_2'(0)$	$\phi_4'(0)$
0.0	0.0	0.0	0.811301	0.094676	0.011705	0.811301	0.094676	0.011705
		0.1	0.953073	0.111221	0.013751	0.810305	0.094560	0.011691
		0.2	0.988200	0.115320	0.014258	0.775538	0.090503	0.011189
	1.0	0.1	1.270471	0.065327	0.004642	1.169800	0.047055	0.002793
	5.0		4.463166	0.002545	0.000003	4.440694	0.001369	0.000001
	10.0		8.805590	0.000344	0	8.794587	0.000181	0
0.5	1.0		0.765688	0.027499	0.002707	0.722477	0.022119	0.001778
1.0			0.518612	0.012595	0.001418	0.498804	0.010703	0.000990
1.5			0.389577	0.007080	0.000847	0.378456	0.006179	0.000611

Table. 2. 5(b). Numerical values of $-\phi_0'(0)$, $\phi_2'(0)$ and $\phi_4'(0)$.

φ	M	N_1	TiO_2 -Water nanofluid		
			$-\phi_0'(0)$	$\phi_2'(0)$	$\phi_4'(0)$
0.0	0.0	0.0	0.811301	0.094676	0.011705
0.1			0.819022	0.095577	0.011817
0.2			0.789063	0.092081	0.011384
0.1	1.0		1.175675	0.048140	0.002895
	5.0		4.441957	0.001426	0.000001
	10.0		8.795207	0.000189	0
	1.0	0.5	0.725143	0.022478	0.001833
		1.0	0.500059	0.010838	0.001017
		1.5	0.379170	0.006246	0.000626

Table. 2. 6(a). $-\theta_0'(0), \theta_{12}'(0)$ and $\theta_{14}'(0)$ when $N_1 = 0.5$.

φ	M	N_2	Al_2O_3 -Water nanofluid			Cu -Water nanofluid		
			$-\theta_0'(0)$	$\theta_{12}'(0)$	$\theta_{14}'(0)$	$-\theta_0'(0)$	$\theta_{12}'(0)$	$\theta_{14}'(0)$
0.0	0.0	0.0	1.518447	0.615987	0.239294	1.518447	0.615987	0.239294
0.1			1.374020	0.467158	0.155804	1.420924	0.427659	0.128054
0.2			1.237966	0.368580	0.110049	1.291484	0.330620	0.086582
0.1	1.0		1.418100	0.432202	0.131229	1.451223	0.406570	0.114632
	5.0		1.613428	0.320890	0.068744	1.615178	0.319486	0.068152
	10.0		1.671431	0.300534	0.059955	1.670761	0.300222	0.059866
	1.0	0.5	0.967924	0.376784	0.290370	0.999085	0.354113	0.255369
		1.0	0.871449	0.276243	0.288779	0.903134	0.258399	0.251649
		1.5	0.829395	0.215670	0.260087	0.861412	0.201215	0.225352

Table. 2. 6(b). $-\theta_0'(0), \theta_{12}'(0)$ and $\theta_{14}'(0)$ when $N_1 = 0.5$.

φ	M	N_2	TiO_2 -Water nanofluid		
			$-\theta_0'(0)$	$\theta_{12}'(0)$	$\theta_{14}'(0)$
0.0	0.0	0.0	1.518447	0.615987	0.239294
0.1			1.399510	0.475001	0.158319
0.2			1.281369	0.381109	0.113856
0.1	1.0		1.443460	0.440112	0.133775
	5.0		1.641117	0.327016	0.070167
	10.0		1.700527	0.306012	0.061082
	1.0	0.5	0.988548	0.386194	0.294901
		1.0	0.889490	0.284371	0.295033
		1.5	0.846134	0.222513	0.266708

2.5 Conclusion

This chapter is based on study of slip conditions and MHD effects on the oscillatory non-orthogonal stagnation point flow of water based nanofluids for three different type of nanoparticles, namely, Cu , Al_2O_3 and TiO_2 . The governing coupled system is solved numerically by using BVP solution method with the aid of midpoint method with Richardson extrapolation enhancement. Moreover, a detailed analysis is presented for the magnetic, velocity slip and thermal jump effects on the flow behavior. The important finding of the current study can be summarized as follows:

- Velocity profile changes its direction for $\mathbb{B} - \mathbb{A} > 0$ and $\mathbb{B} - \mathbb{A} < 0$.
- The momentum boundary layer thickness becomes thinner for higher values of M , φ and N_2 .
- The thermal boundary layer thickness decreases for higher values of N_2 and M .
- The velocity amplitude of oscillation is maximum at the surface and gradually decrease when it goes away from the surface
- The stagnation point appears on the right side of the plate, from origin, for $\mathbb{B} - \mathbb{A} > 0$ and on the opposite side for $\mathbb{B} - \mathbb{A} < 0$.
- The momentum boundary layer thickness decreases against all physical involved parameters whereas Al_2O_3 produce highest value of boundary layer and Cu has the lowest.
- The values of $f''(0)$ increases for higher values of M and decreases against velocity slip parameter N_1 . Also, $f''(0)$ is maximum for $Cu - water$ nanofluids and minimum for $Al_2O_3 - water$ nanofluids.
- Nusselt number enhances against the Hartmann number M and reduce for higher values of N_2 and φ .
- $Cu - water$ produce the highest Nusselt number whereas $Al_2O_3 - water$ produce the lowest.

Chapter # 3

Impact of external magnetic field and metallic particles on oscillatory oblique stagnation point flow of a micropolar fluid

3.1 Introduction

The present chapter is made to envision the characteristics of magneto-hydrodynamic oscillatory oblique stagnation point flow of micropolar nanofluid. The applied magnetic field is assumed parallel towards dividing streamline. A comparative study is executed for copper Cu and Alumina Al_2O_3 nanoparticles while considering water as a base fluid. To be more specific, in the presence of both weak and strong concentration, the physical situation of micropolar fluid is mathematically modeled in terms of differential equations. The transformed coupled system is finally solved by midpoint method with the Richardson extrapolation enhancement and shooting mechanism with fifth order R-K Fehlberg technique. The obtained results are compared with existing published literature. An excellent match has been found which yields the validity of the current analysis.

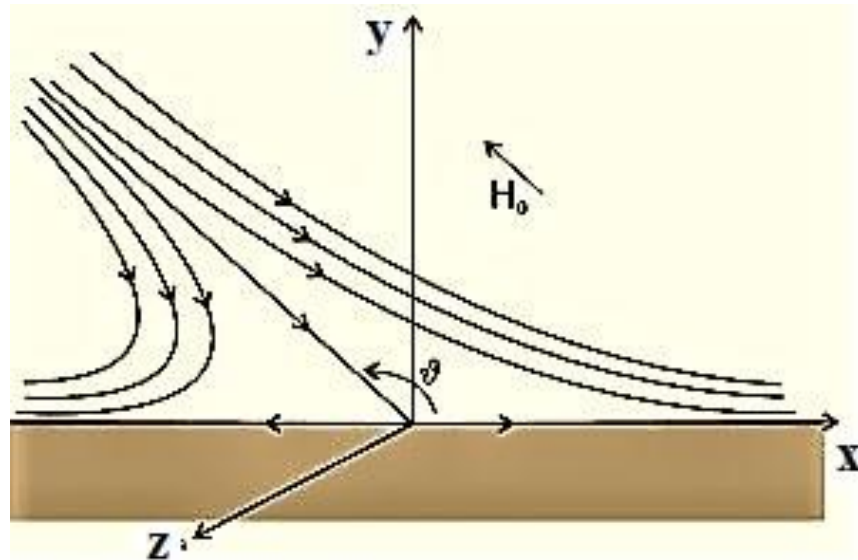


Fig. 3. 1. Flow description of the problem.

3.2 Problem description and governing equations:

Consider the problem of stagnation point flow of an electrically conducting micropolar nanofluid over an oscillatory surface with velocity $U \cos \omega \bar{t}$. The fluid impinges obliquely on the oscillatory surface $\bar{y} = 0$. By neglecting external mechanical body force and body couple the flow rheological equations become

$$\left. \begin{aligned} \bar{\nabla} \cdot \bar{\mathbf{V}} &= 0 \\ \left(\frac{\partial \bar{\mathbf{V}}}{\partial \bar{t}} + (\bar{\mathbf{V}} \cdot \bar{\nabla}) \bar{\mathbf{V}} \right) &= -\frac{1}{\rho_{nf}} \bar{\nabla} \bar{p} + \frac{1}{\rho_{nf}} (\mu_{nf} + \kappa) \bar{\nabla}^2 \bar{\mathbf{V}} + \frac{\mu_e}{\rho_{nf}} (\bar{\nabla} \times \bar{\mathbf{H}}) \times \bar{\mathbf{H}} \\ &\quad + \frac{\kappa}{\rho_{nf}} (\bar{\nabla} \times \bar{\mathbf{N}}) \\ \rho_{nf} j \left(\frac{\partial \bar{\mathbf{N}}}{\partial \bar{t}} + (\bar{\mathbf{V}} \cdot \bar{\nabla}) \bar{\mathbf{N}} \right) &= \gamma_{nf} \bar{\nabla}^2 \bar{\mathbf{N}} + \kappa (\bar{\nabla} \times \bar{\mathbf{V}}) - 2\kappa \bar{\mathbf{N}} \\ \left(\frac{\partial \bar{T}}{\partial \bar{t}} + (\bar{\mathbf{V}} \cdot \bar{\nabla}) \bar{T} \right) &= \alpha_{nf} \bar{\nabla}^2 \bar{T} \\ \bar{\nabla} \times \bar{\mathbf{E}} &= 0, \quad \bar{\nabla} \cdot \bar{\mathbf{H}} = 0, \\ \bar{\nabla} \cdot \bar{\mathbf{E}} &= 0, \quad \bar{\nabla} \times \bar{\mathbf{H}} = \sigma_e (\bar{\mathbf{E}} + \mu_e \bar{\nabla} \times \bar{\mathbf{H}}), \end{aligned} \right\} \quad (3.1)$$

For system (3.1) we append the boundary condition:

$$\left. \begin{aligned} \bar{u} &= U \cos \omega \bar{t}, \quad \bar{v} = 0, \quad \bar{N} = -n \frac{\partial \bar{u}}{\partial \bar{y}}, \\ \bar{T} &= \bar{T}_w + \epsilon (\bar{T}_w - \bar{T}_\infty) \text{Re}[e^{i\omega \bar{t}}] \quad \text{at } \bar{y} = 0 \\ \bar{u} &= a\bar{x} + b\bar{y}, \quad \bar{v} = -a\bar{y}, \quad \bar{N} = \frac{1}{2} (\bar{\nabla} \times \bar{\mathbf{V}}), \quad T = \bar{T}_\infty \quad \text{as } \bar{y} \rightarrow \infty. \end{aligned} \right\} \quad (2.2)$$

It is interesting to note that the concentration of micropolar fluid is controlled by the value of micro gyration parameter n ($0 \leq n \leq 1$). For the case of $n = 0$, we have $\bar{N} = 0$ at the wall which shows strong concentration [74]. Physically it means that microelements near the surface are unable to rotate [75]. Further, for the case $n = 1/2$, narrates the vanishing of anti-symmetric part of the stress tensor and indicates weak concentration [76] of microelements. On the other side, at $n = 1$, flows indicate turbulent boundary layer flow [77]

Conditions (3.2) mean that at infinity, $\bar{\mathbf{N}} = \frac{1}{2} (\bar{\nabla} \times \bar{\mathbf{V}})$, the micropolar fluid behaves like a classical fluid.

The equations of degenerate streamlines, also known as asymptotes of streamlines, can be expressed as:

$$\bar{y} = -\frac{2a}{b}\bar{x} \text{ and } \bar{y} = 0. \quad (3.3)$$

Considering a more general motion as reported by [73]

$$\bar{v} = -a(\bar{y} - A), \quad \bar{u} = a\bar{x} + b(\bar{y} - B).$$

In this way, the stagnation point is $(\frac{b}{a}(B - A), A)$ and the asymptotes of the streamlines becomes

$$\bar{y} = -\frac{2a}{b}\bar{x} + 2B - A, \text{ and } \bar{y} = A.$$

Further, [73] show that

$$\bar{\mathbf{H}}_0 = H_0(b^2 + 4a^2)^{-\frac{1}{2}}(-b\hat{\mathbf{i}} + 2a\hat{\mathbf{j}}). \quad (3.4)$$

Neglect the influence of induced magnetic field, we have

$$(\bar{\mathbf{V}} \times \bar{\mathbf{H}}) \times \bar{\mathbf{H}} \sim \sigma_e \mu_e (\bar{\mathbf{V}} \times \bar{\mathbf{H}}_0) \times \bar{\mathbf{H}}_0, \quad \bar{\mathbf{E}} = 0, \quad (3.5)$$

and by consideration of

$$\left. \begin{aligned} \bar{N} &= \bar{x}\bar{F}(\bar{y}) + \bar{G}(\bar{y}, \bar{t}) \\ \bar{v} &= -a\bar{f}'(\bar{y}), \bar{u} = a\bar{x}\bar{f}'(\bar{y}) + b\bar{g}(\bar{y}, \bar{t}) \\ \gamma_{nf} &= \left(\mu_{nf} + \frac{\kappa}{2}\right)j \\ j &= \frac{a}{\nu_f} \end{aligned} \right\}, \quad (3.6)$$

Eqs. (3.1) and (3.2) can be written as

$$\begin{aligned}
a\bar{x} \left[a\bar{f}'^2 - a\bar{f}\bar{f}'' - \left(v_{nf} + \frac{\kappa}{\rho_{nf}} \right) \bar{f}''' - \frac{\kappa}{a\rho_{nf}} \bar{F}' + 4a^2 \frac{\sigma_{nf}}{\rho_{nf}} \frac{B_0^2}{4a^2 + b^2} \bar{f}' \right] \\
+ b \left[\bar{g}_{\bar{t}} + a(\bar{g}\bar{f}' - \bar{f}\bar{g}') - \left(v_{nf} + \frac{\kappa}{\rho_{nf}} \right) \bar{g}'' - \frac{\kappa}{b\rho_{nf}} \bar{G}' \right. \\
\left. + 2a^2 \frac{\sigma_{nf}}{\rho_{nf}} \frac{B_0^2}{4a^2 + b^2} (2\bar{g} - \bar{f}) \right] = -\frac{1}{\rho_{nf}} \frac{\partial \bar{p}}{\partial \bar{x}}
\end{aligned} \tag{3.7}$$

$$\begin{aligned}
a^2 \bar{f}\bar{f}' + \left(v_{nf} + \frac{\kappa}{\rho_{nf}} \right) \bar{f}'' - \frac{\kappa}{\rho_{nf}} \bar{F} \\
+ \frac{\sigma_{nf}}{\rho_{nf}} \frac{B_0^2}{4a^2 + b^2} \left(2a^2 b \bar{x} \bar{f}' + ab^2 (2\bar{g} - \bar{f}) \right) = -\frac{1}{\rho_{nf}} \frac{\partial \bar{p}}{\partial \bar{y}}
\end{aligned} \tag{3.8}$$

$$\begin{aligned}
\left(v_{nf} + \frac{\kappa}{2\rho_{nf}} \right) (\bar{x}\bar{F}'' + \bar{G}'') + \frac{\kappa}{j\rho_{nf}} (-a\bar{x}\bar{f}'' - b\bar{g}') - \frac{2\kappa}{j\rho_{nf}} (\bar{x}\bar{F} + \bar{G}) \\
= \bar{G}_{\bar{t}} + (a\bar{x}\bar{f}' + b\bar{g})\bar{F} - a\bar{f}(\bar{x}\bar{F}' + \bar{G}')
\end{aligned} \tag{3.9}$$

$$\left. \begin{aligned}
\bar{f}(0) = 0, \bar{f}'(0) = 0, \bar{g}(0, \bar{t}) = \frac{U}{b} \text{Re}(e^{i\omega\bar{t}}), \\
\bar{F}(0) = -a n \bar{f}''(0), \bar{G}(0, \bar{t}) = -b n \bar{g}'(0, \bar{t}), \\
\bar{f}'(\bar{y}) = 1, \bar{g}'(\bar{y}, \bar{t}) = 1, \bar{F}(\bar{y}) = 0, \bar{G}(\bar{y}, \bar{t}) = -\frac{b}{2} \quad \text{as } \bar{y} \rightarrow \infty
\end{aligned} \right\} \tag{3.10}$$

From (3.10), we can find the asymptotic solutions for large \bar{y}

$$\bar{g}(\bar{y}) \sim \bar{y} - B \quad \text{and} \quad \bar{f}(\bar{y}) \sim \bar{y} - A. \tag{3.11}$$

From Eqs. (3.7-3.8), we find the pressure field as

$$\begin{aligned}
\bar{p}_0 - \bar{p}(\bar{x}, \bar{y}) = \rho_{nf} & \left[\frac{a^2}{2} (\bar{x}^2 + \bar{f}^2 - 2 \frac{b}{a} (B - A) \bar{x}) + \left(v_{nf} + \frac{\kappa}{\rho_{nf}} \right) a \bar{f}' \right. \\
& + \frac{\kappa}{\rho_{nf}} \int_0^{\bar{y}} \bar{F}(\bar{s}) d\bar{s} \\
& + \frac{\sigma_{nf}}{\rho_{nf}} \frac{B_0^2}{4a^2 + b^2} \left\{ 2a^2 b \bar{x} \bar{f}' + 4a^3 \left(\bar{x}^2 - 2 \frac{b}{a} (B - A) \bar{x} \right) \right. \\
& \left. \left. + ab^2 \int_0^{\bar{y}} \left(2\bar{g}(\bar{s}, \bar{t}) - \bar{f}(\bar{s}) \right) d\bar{s} \right\} \right], \tag{3.12}
\end{aligned}$$

in which \bar{p}_0 is the stagnation pressure. From Eq. (3.12), it is clearly seen that maximum pressure occurs at the stagnation point in through-out the flow domain. Thus Eqs. (3.7) -(3.9) implies that

$$\begin{aligned}
& \frac{1}{a} \left(v_{nf} + \frac{\kappa}{\rho_{nf}} \right) \bar{f}'''' - \bar{f}'^2 + \bar{f} \bar{f}'' + \frac{\kappa}{a^2 \rho_{nf}} \bar{F}' \\
& - 4a \frac{\sigma_{nf}}{\rho_{nf}} \frac{B_0^2}{4a^2 + b^2} (\bar{f}' - 1) + 1 = 0 \\
& \frac{1}{a} \left(v_{nf} + \frac{\kappa}{\rho_{nf}} \right) \bar{g}'' - \bar{g} \bar{f}' - \frac{1}{a} \bar{g}_{\bar{t}} + \bar{f} \bar{g}' + \frac{\kappa}{ab \rho_{nf}} \bar{G}' \\
& + 4a \frac{\sigma_{nf}}{\rho_{nf}} \frac{B_0^2}{4a^2 + b^2} (\bar{f} - \bar{g}) = \left(1 + 4a \frac{\sigma_{nf}}{\rho_{nf}} \frac{B_0^2}{4a^2 + b^2} \right) (B - A) \\
& \left(v_{nf} + \frac{\kappa}{2\rho_{nf}} \right) \bar{F}'' + a \bar{f} \bar{F}' - a \bar{f}' \bar{F} - \frac{\kappa}{j \rho_{nf}} a \bar{f}'' - \frac{2\kappa}{j \rho_{nf}} \bar{F} = 0 \\
& \left(v_{nf} + \frac{\kappa}{2\rho_{nf}} \right) \bar{G}'' + a \bar{f} \bar{G}' - b \bar{g} \bar{F} - \bar{G}_{\bar{t}} - \frac{\kappa}{j \rho_{nf}} b \bar{g}' - \frac{2\kappa}{j \rho_{nf}} \bar{G} = 0 \tag{3.13}
\end{aligned}$$

The following similarity variables are presented to make simpler the mathematical analysis of the problem

$$f(y) = \sqrt{\frac{a}{v_f}} \bar{f} \left(\sqrt{\frac{v_f}{a}} y \right), \quad y = \sqrt{\frac{a}{v_f}} \bar{y}, \quad F(y) = \frac{1}{a} \sqrt{\frac{v_f}{a}} \bar{F} \left(\sqrt{\frac{v_f}{a}} y \right), \quad t = \omega \bar{t},$$

$$g_0(y) + \varepsilon g_1(y) e^{it} = g(y, t) = \sqrt{\frac{a}{v_f}} \bar{g} \left(\sqrt{\frac{v_f}{a}} y, \frac{t}{\omega} \right), \quad (3.14)$$

$$G_0(y) + \varepsilon G_1(y) e^{it} = G(y, t) = \frac{1}{b} \bar{G} \left(\sqrt{\frac{v_f}{a}} y, \frac{t}{\omega} \right),$$

$$\theta_0(y) + \varepsilon \theta_1(y) e^{it} = \theta(y, t) = \frac{T - T_\infty}{T_w - T_\infty},$$

Using the above similarity variables, Eqs. (3.13) and (3.14) together with boundary conditions (3.10) and (3.2)_{4,8} reduce to

$$\begin{aligned} & \left(\frac{\mu_{nf}}{\mu_f} + K \right) \frac{\rho_f}{\rho_{nf}} f''' - f'^2 + ff'' + K \frac{\rho_f}{\rho_{nf}} F' + \frac{\sigma_{nf}}{\sigma_f} \frac{\rho_f}{\rho_{nf}} M^2 (1 - f') + 1 = 0, \\ & \left(\frac{\mu_{nf}}{\mu_f} + K \right) \frac{\rho_f}{\rho_{nf}} g_0'' + f g_0' - g_0 f' + K \frac{\rho_f}{\rho_{nf}} G_0' - \frac{\sigma_{nf}}{\sigma_f} \frac{\rho_f}{\rho_{nf}} M^2 (g_0 - f) = \\ & \quad \left(1 + \frac{\sigma_{nf}}{\sigma_f} \frac{\rho_f}{\rho_{nf}} M^2 \right) (\mathbb{B} - \mathbb{A}), \\ & \left(\frac{\mu_{nf}}{\mu_f} + K \right) \frac{\rho_f}{\rho_{nf}} g_1'' + f g_1' - g_1 f' - i\Omega g_1 + K \frac{\rho_f}{\rho_{nf}} G_1' - \frac{\sigma_{nf}}{\sigma_f} \frac{\rho_f}{\rho_{nf}} M^2 g_1 = 0, \\ & \quad \left(\frac{\mu_{nf}}{\mu_f} + \frac{K}{2} \right) \frac{\rho_f}{\rho_{nf}} F'' - f'F + fF' - K \frac{\rho_f}{\rho_{nf}} (f'' - 2F) = 0, \\ & \quad \left(\frac{\mu_{nf}}{\mu_f} + \frac{K}{2} \right) \frac{\rho_f}{\rho_{nf}} G_0'' - g_0 F + f G_0' - K \frac{\rho_f}{\rho_{nf}} (g_0' - 2G_0) = 0, \\ & \quad \left(\frac{\mu_{nf}}{\mu_f} + \frac{K}{2} \right) \frac{\rho_f}{\rho_{nf}} G_1'' + f G_1' - g_1 F - i\Omega G_1 - K \frac{\rho_f}{\rho_{nf}} (g_1' - 2G_1) = 0, \\ & \quad \frac{k_{nf}}{k_f} \theta_0'' + Pr \frac{(\rho C_p)_{nf}}{(\rho C_p)_f} f \theta_0' = 0, \\ & \quad \frac{k_{nf}}{k_f} \theta_1'' + Pr \frac{(\rho C_p)_{nf}}{(\rho C_p)_f} f \theta_1' - i\Omega Pr \frac{(\rho C_p)_{nf}}{(\rho C_p)_f} \theta_1 = 0, \end{aligned} \quad \text{J} \quad (3.15)$$

$$\left. \begin{aligned} f(0) = 0, g_0(0) = 0, f'(0) = 0, g_1(0) = 1, \theta_0(0) = 1, \theta_1(0) = 1, \\ F(0) = -nf''(0), G_0(0) = -ng'_0(0), G_1(0) = -ng'_1(0), \\ g_1(y) = 0, g'_0(y) = 1, f'(y) = 1, F(y) = 0, G_0(y) = -\frac{1}{2}, G_1(y) = 0, \quad y \rightarrow \infty \\ \theta_0(y) = 0, \theta_1(y) = 0, g(y) \sim y - \mathbb{B}, f(y) \sim y - \mathbb{A}, \quad \bar{y} \rightarrow \infty, \end{aligned} \right\} \quad (3.16)$$

Where

$$\mathbb{B} = B \sqrt{\frac{a}{v_f}}, \quad \mathbb{A} = A \sqrt{\frac{a}{v_f}}, \quad M^2 = 4a \frac{\sigma_f}{\rho_f} \frac{B_0^2}{4a^2 + b^2}, \quad K = \frac{\kappa}{\mu_f}, \quad \Omega = \frac{\omega}{a}, \quad Pr = \frac{v_f}{k_f}, \quad \epsilon = \frac{U}{b} \sqrt{\frac{a}{v_f}}.$$

The surface shear stress (C_f) and heat transfer rate (Nu) in dimensionless form can be expressed as

$$C_f = \frac{\tau_w}{\frac{1}{2} \rho_f U_w^2}, \quad (3.17)$$

$$Nu = \frac{\bar{x} q_w}{k_f (\bar{T}_w - \bar{T}_\infty)},$$

where τ_w , is the wall shear stress and q_w the surface heat flux defines as

$$\tau_w = \left[(\mu_{nf} + \kappa) \frac{\partial \bar{u}}{\partial \bar{y}} + \kappa \bar{N} \right] \Big|_{\bar{y}=0}, \quad (3.18)$$

$$q_w = -k_{nf} \frac{\partial \bar{T}}{\partial \bar{y}} \Big|_{\bar{y}=0}.$$

By using of (3.14), (3.17) and (3.18), we may write it as

$$\frac{1}{2} Re_{\bar{x}} C_f = \left(\frac{\mu_{nf}}{\mu_f} + (1-n)K \right) \left[\sqrt{Re_{\bar{x}}} f''(0) + \frac{b}{a} g'_0(0) - \epsilon \frac{b}{a} e^{it} g'_1(0) \right]$$

$$(Re_{\bar{x}})^{-\frac{1}{2}} Nu = -\frac{k_{nf}}{k_f} \theta_0'(0) - \frac{k_{nf}}{k_f} \epsilon e^{it} \theta_1(0),$$

At the surface $\bar{y} = 0$, three points carry significant importance: the stagnation point towards which the separating streamline far away from the surface are directed, the position

where maximum pressure is exerted $\bar{x} = \bar{x}_p$, and the position of zero tangential stress $\bar{x} = \bar{x}_s$. The equation of separating streamline which intersect the boundary is

$$x = \sqrt{\frac{a}{v_f}} \bar{x}, \quad xf(y) + \frac{b}{a} \int_0^y (g_0(s) + \varepsilon e^{it} g_1(s)) ds = 0, \quad (3.19)$$

From Eqs. (3.12) and (3.18), we see that

$$\begin{aligned} \bar{x}_p &= \frac{b}{a} \left(\frac{v_f}{a}\right)^{1/2} (\beta - \alpha), \\ \bar{x}_s &= -\frac{b}{a} \left(\frac{v_f}{a}\right)^{1/2} \frac{1}{f''(0)} (g_0'(0) + \varepsilon e^{it} g_1'(0)). \end{aligned} \quad (3.20)$$

We note that \bar{x}_p does not depend on M whereas \bar{x}_s depends on M . The ratio

$$\frac{\bar{x}_p}{\bar{x}_s} = -(\mathbb{B} - \mathbb{A}) \frac{f''(0)}{[g_0'(0) + \varepsilon e^{it} g_1'(0)]'}$$

(for a fixed time) is same for all angles of incidence.

3.3 Solution procedure:

Numerical solution of (3.15)_{1,2,4,5} together with their boundary conditions in (3.16) have been deliberated by means of shooting technique with fifth order R–K–Fehlberg method and midpoint method with the Richardson extrapolation enhancement.

Furthermore, the series solutions of equations (3.15)_{3,6} for small value of frequency Ω have been obtained, that is

$$g_1(y) = \sum_{n=0}^{\infty} (i\Omega)^n \Phi_n(y)$$

and

$$G_1(y) = \sum_{n=0}^{\infty} (i\Omega)^n \gamma_n(y)$$

In this problem, the real part of solution is

$$g_1(y) = \Phi_0(y) - \Omega^2\Phi_2(y) + \Omega^4\Phi_4(y) \dots,$$

where

$$\left. \begin{aligned} \frac{\mu_{nf}}{\mu_f} \frac{\rho_f}{\rho_{nf}} \Phi_0'' + f\Phi_0' - \Phi_0 f' + K \frac{\rho_f}{\rho_{nf}} \gamma_0 - \frac{\rho_f}{\rho_{nf}} M^2 \Phi_0 &= 0 \\ \frac{\mu_{nf}}{\mu_f} \frac{\rho_f}{\rho_{nf}} \Phi_n'' + f\Phi_n' - \Phi_n f' + K \frac{\rho_f}{\rho_{nf}} \gamma_n - \frac{\rho_f}{\rho_{nf}} M^2 \Phi_n &= \Phi_{n-1} \\ \Phi_0(0) = 1, \quad \Phi_0(\infty) &= 0 \\ \Phi_n(0) = 0, \quad \Phi_n(\infty) &= 0 \end{aligned} \right\}, \quad n = 1, 2, 3 \dots$$

The above system has been tackled numerically using midpoint method with the Richardson extrapolation enhancement.

Similarly, for a small value of Ω , equation (3.15)₅ becomes

$$\theta_1(y) = \sum_{n=0}^{\infty} (i\Omega)^n \Theta_{1n}(y).$$

$$\theta_1(y) = \Theta_{10}(y) - \Omega^2\Theta_{12}(y) + \Omega^4\Theta_{14}(y) \dots \quad (3.21)$$

From (3.15)₄, we have

$$\theta_0(y) = \frac{I_{nf}(Pr, \infty) - I_{nf}(Pr, y)}{I_{nf}(Pr, \infty)} \quad (3.22)$$

where

$$I_{nf}(Pr, y) = \int_0^y \text{Exp} \left(-Pr \frac{k_f}{k_{nf}} \frac{(\rho C_p)_{nf}}{(\rho C_p)_f} \int_0^s f(\eta) d\eta \right) ds$$

and

$$I_{nf}(Pr, \infty) = \lim_{y \rightarrow \infty} I_{nf}(Pr, y).$$

Making use of Eqs. (3.21) and (3.15)₅, we may write

$$\left. \begin{aligned} \frac{1}{Pr} \frac{k_{nf}}{k_f} \Theta_{1n}'' + \frac{(\rho C_p)_{nf}}{(\rho C_p)_f} (f\Theta_{1n}' - \Theta_{1(n-1)}) &= 0 \\ \Theta_{1n}(0) = 0, \quad \Theta_{1n}(\infty) &= 0 \end{aligned} \right\}, \quad n = 1, 2, 3 \dots$$

Where $\Theta_{10}(y) = \theta_0(y)$ is given in (3.22)

The numerical integration for the above system can be executed easily with aid of any mathematical software.

3.4 Results and Discussion:

Numerical assessment is carried out towards model equations by way of water based micropolar nanofluid containing metals and oxide ceramics nanoparticles named as Alumina (Al_2O_3) and copper (Cu). The range of solid volume fraction φ for the nanoparticles is maintained as $0 \leq \varphi \leq 0.2$ along with the upper limit of Prandtl number is 6.2 for base fluid i-e water. **Table 1.2** is used to present the thermos-physical properties of Copper, Alumina and water. The numerical scheme is validated by constructing discrete case of Hartmann number by ignoring the effects of nanoparticles shown in **Table 3.1** and **Table 3.2**, we have found that our obtained results are agreed perfectly with [73].

The influences of involved physical parameters on velocity distributions are portrayed in **Figs. (3.2-3.6)**. The combined impact of free stream and magnetic action claims the fluid flow past an oscillatory sheet. The velocity of nanofluid is minimum near the plate and gradually increases until it attains the free stream condition and satisfying the prearranged endpoint condition. **Fig. 3.2** depicts the behavior of $f(y), f'(y), f''(y)$ for $M = 10^{-7}, \varphi = 0.0, K = 0.0$. **Fig. 3.4** displays the alterations in $f'(y)$ for distinct values of K, φ, n and different nanoparticles when water is considered as base fluid. In **Fig. 3.4(a)**, it is detected that thickness of momentum boundary layer increases by increasing the material parameter K . In **Fig. 3.4(b)**, it is seen that the momentum boundary layer thickness decreases with increasing the nanoparticle volume fraction φ . The strength of **Fig. 3.4(c)** is drawn to discuss the impact of an imperative parameter n , the micro gyration parameter, which indicates the concentration of micropolar fluid. From this figure, it can be observed that momentum boundary layer thickness is thin just in case of weak concentration as compared to strong concentration. It is interesting to note that $Al_2O_3 - water$ nanofluid produce a thicker momentum boundary layer than $Cu - water$ as illustrated in **Fig. 3.4(d)**. **Fig. 3.3** indicates the profile of $F(y), F'(y)$ when $M = 10^{-7}, K = 1.0$ and $\varphi = 0.0$. In **Fig. 3.5**, demonstrates the change in $g_0(y)$ for dissimilar Hartmann number M and micro gyration parameter n along with the condition i.e. $\mathbb{B} - \mathbb{A} =$

$-5 - \mathbb{A}$ and $\mathbb{B} - \mathbb{A} = 5 - \mathbb{A}$. The flow field is unaffected by Prandtl number because flow equations and temperature are uncoupled. To be more specific, the fact is that for every value of Pr , functions i-e $f(y), g_0(y), g_1(y)$ and their derivatives are found to be identical. In **Fig. 3.6** the impact of time t on $u(x, y, t)$ is reported. It is seen that $u(x, y, t)$ shows an oscillation performance with maximum amplitude at the surface and gradually decreases away from the surface. **Fig. 3.7** depicts the attitude of the temperature distribution $\theta(y, t)$ towards nanoparticle volume fraction φ and Hartmann number M when $Pr = 6.2$. The influence of increasing Hartmann number on temperature profile, the decreasing nature of temperature field can be observed neat the surface, while it shows a rise in behavior with the enhancement in nanoparticle volume fraction. The impact of time t on $\theta(x, y, t)$ is shown with the aid of **Fig. 3.8**. It is noticed that $\theta(x, y, t)$ exhibit waving nature and the amplitude of wave is found maximum near the surface and decreases far away from the surface. Further, it is examined that the temperature is maximum at the surface, that is $y = 0$, and decrease away from it. The oblique flows are presented by way of streamline patterns in **Figs. (3.9-3.11)**. The streamline meets the wall $y = 0$, at \bar{x}_s . It is concluded from these figures that their location depends on Hartmann number M , $\mathbb{B} - \mathbb{A}$ and time t . **Fig. 3.12**. shows the bar graph comparison of both Copper and Aluminum oxide nanoparticles. It demonstrates that Copper has higher surface temperature gradient when contrasted with the Aluminum oxide nanoparticles.

Table 3.3-3.6 delineate the impacts of the involved parameter on the physical quantities near the wall for both Copper and Aluminum oxide nanoparticles when water is treated as a base fluid. We comment that the estimations of \mathbb{A} and $f''(0)$ rely on upon M , φ and K , as should be obvious from **Table 3.3(a, b)**. More precisely, $f''(0)$ increases and α decreases as φ and M are increases. Moreover, increases in material parameter K cause increase in \mathbb{A} and decrease in $f''(0)$. **Table 3.4(a, b)** shows the numerical values of velocity gradient at the surface against M , φ , K and $\mathbb{B} - \mathbb{A} = -\mathbb{A}, 0, \alpha$ and it is noticed that the magnitude of $g_0(y)$ does not depend on φ . As far as the variation of $g_0(y)$ against M and K are concerned, we found its magnitude shows increments when M increases while shows decline nature for all $\mathbb{B} - \mathbb{A}$ when K increases. The rapid increase is found for Cu -water nanofluid as compared to Al_2O_3 -water. The numerical variation of $\phi_0'(0), \phi_2'(0), \phi_4'(0)$ against M , φ , and K are revealed in **Table 3.5(a, b)**. In **Table 3.6(a, b)**, it is found that temperature gradient is

decreasing function of both material parameter K and nanoparticle volume fraction φ . Thus, the heat transfer rate increase near the surface. It is important to note that Cu -water remarks higher heat transfer rate as compared to Al_2O_3 -water nanofluid. Furthermore, it is also noticed that the temperature gradient shows inciting attitude when we increase Hartmann number M which brings enhancement in heat transfer rate near the surface.

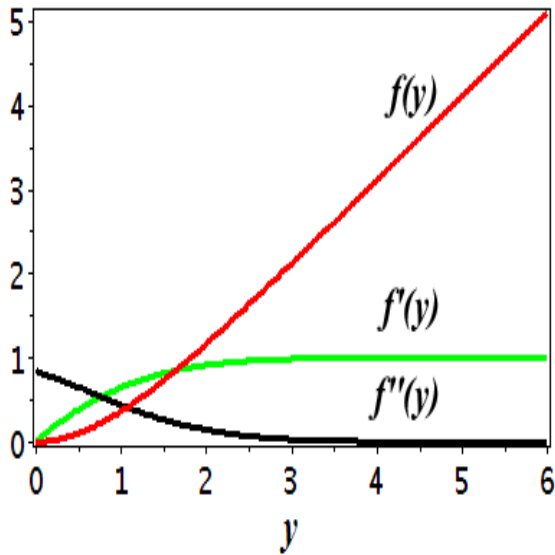


Fig. 3. 2. $f(y)$, $f'(y)$, $f''(y)$ when $M = 10^{-7}$, $\varphi = 0.0$, $K = 0.0$

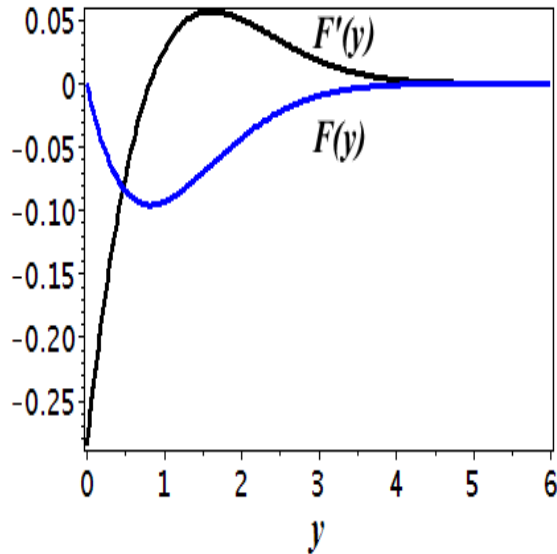
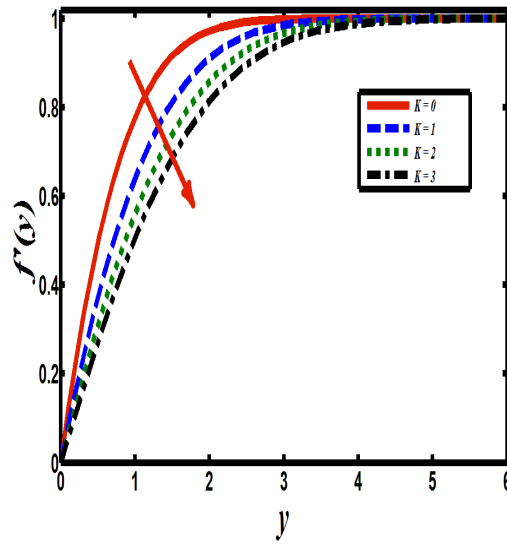
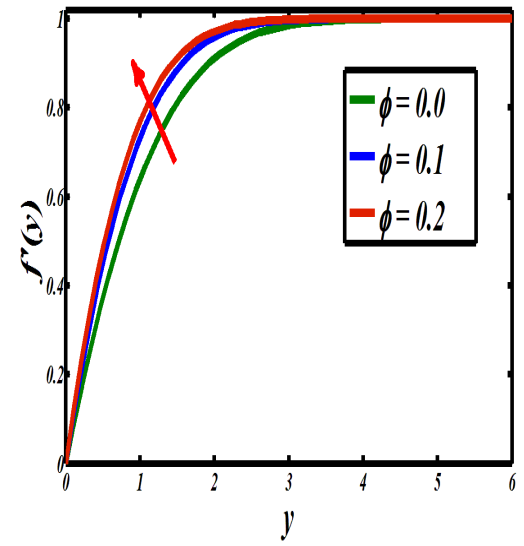


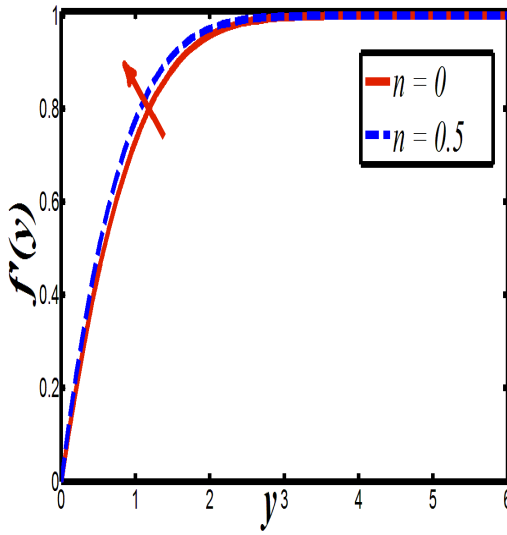
Fig. 3. 3. $F(y)$, $F'(y)$ when $M = 10^{-7}$, $\varphi = 0.0$, $K = 1.0$.



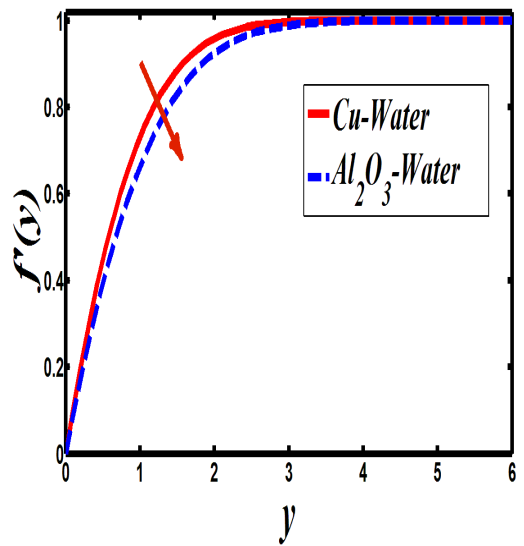
(a)



(b)



(c)



(d)

Fig. 3. 4. Plots showing $f'(y)$ when $M = 10^{-7}$ (a) $\phi = 0.0, n = 0, M = 10^{-7}$, (b) $n = 0.1, K = 0.0$ and (c) $K = 0, \phi = 0.0$ (d) $n = 0, K = 0, \phi = 0.1$.

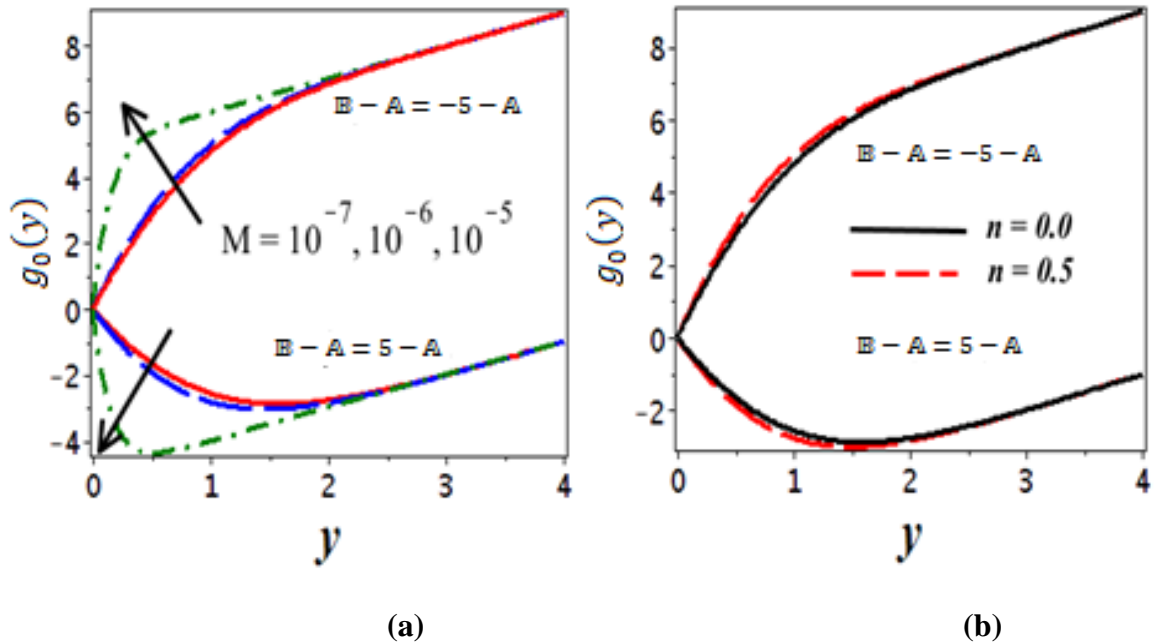


Fig. 3. 5. Influence of $g_0(y)$, (a) for various M when $\varphi = 0.0, K = 0.0$ and (b) for various n when $M = 10^{-7}, \varphi = 0.0, K = 0$.

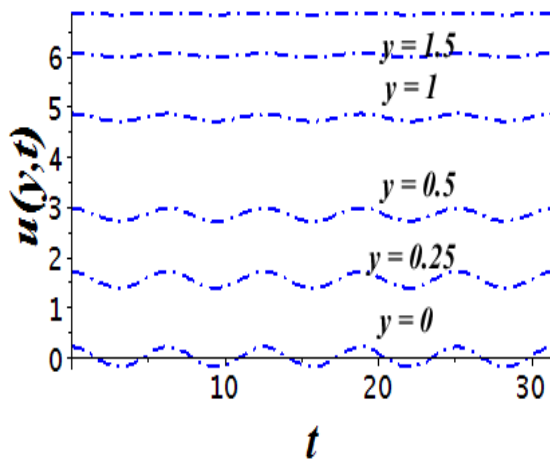


Fig. 3. 6. Time dependent flow $u(y, t)$ at different locations from the surface when $Cu - Water, \varphi = 0.1, K = 0.0, M = 10^{-7}, \varepsilon = 0.2, \Omega = 0.2, \mathbb{B} - \mathbb{A} = -\mathbb{A}, x = 1$.

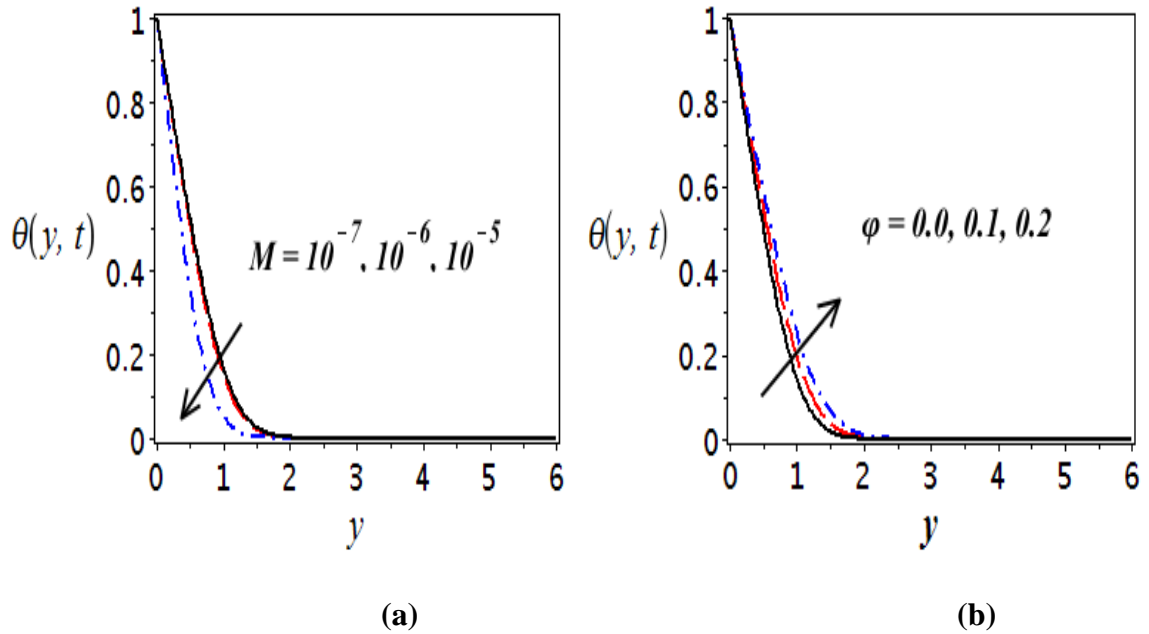


Fig. 3. 7. Influence of $\theta(y, t)$ for various parameters when (a) $\varphi = 0.0, K = 0.0$ and (b) $M = 10^{-7}, K = 0.0$.

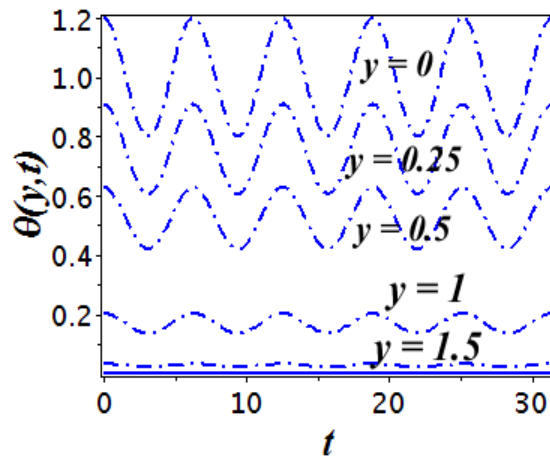


Fig. 3. 8. Time dependent flow $\theta(y, t)$ at different locations from the surface when $Cu - Water, \varphi = 0.1, K = 0.0, M = 10^{-7}, \varepsilon = 0.2, \Omega = 0.2, x = 1$.

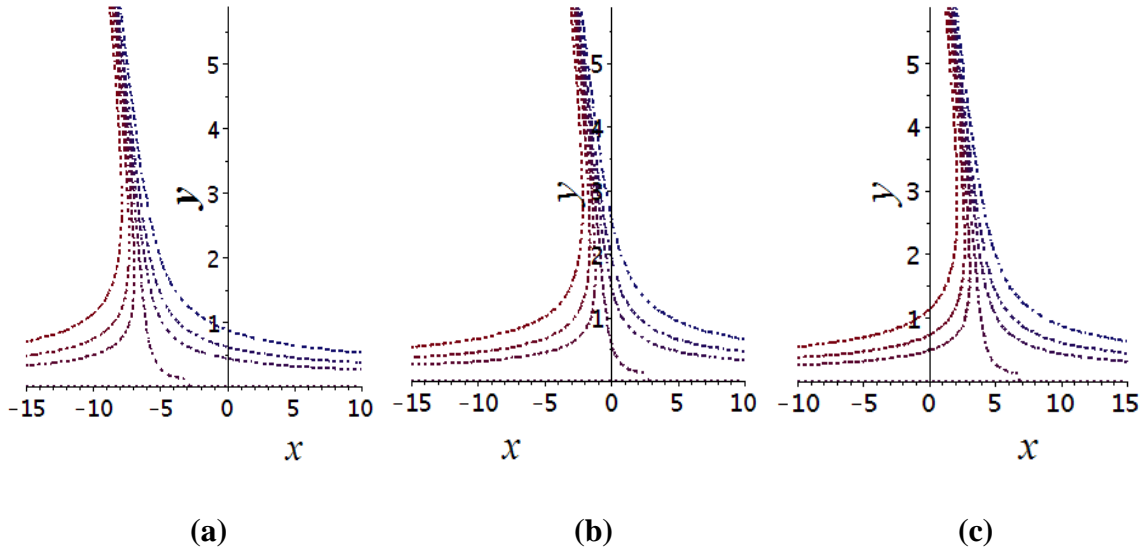


Fig. 3. 9. Shows the streamlines for *Cu – Water* nanofluid when $\frac{b}{a} = 1, M = 10^{-7}, K = 1, \Omega = 0.5, \varepsilon = 0.2, t = \pi$. (a) $\mathbb{B} - \mathbb{A} = -5 - \mathbb{A}$, (b) $\mathbb{B} - \mathbb{A} = 0$, (c) $\mathbb{B} - \mathbb{A} = 5 - \mathbb{A}$.

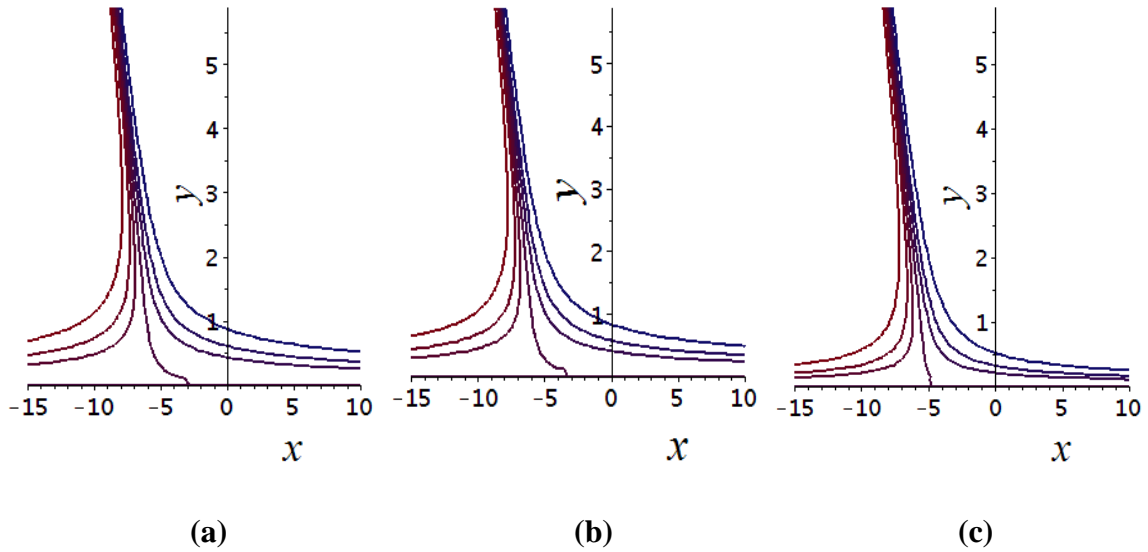


Fig. 3. 10. Shows the streamlines for *Cu – Water* nanofluid when $\frac{b}{a} = 1, \mathbb{B} - \mathbb{A} = -5 - \mathbb{A}, K = 1, \Omega = 0.5, \varepsilon = 0.2, t = \pi$. (a) $M = 10^{-7}$, (b) $M = 10^{-6}$, (c) $M = 10^{-5}$.

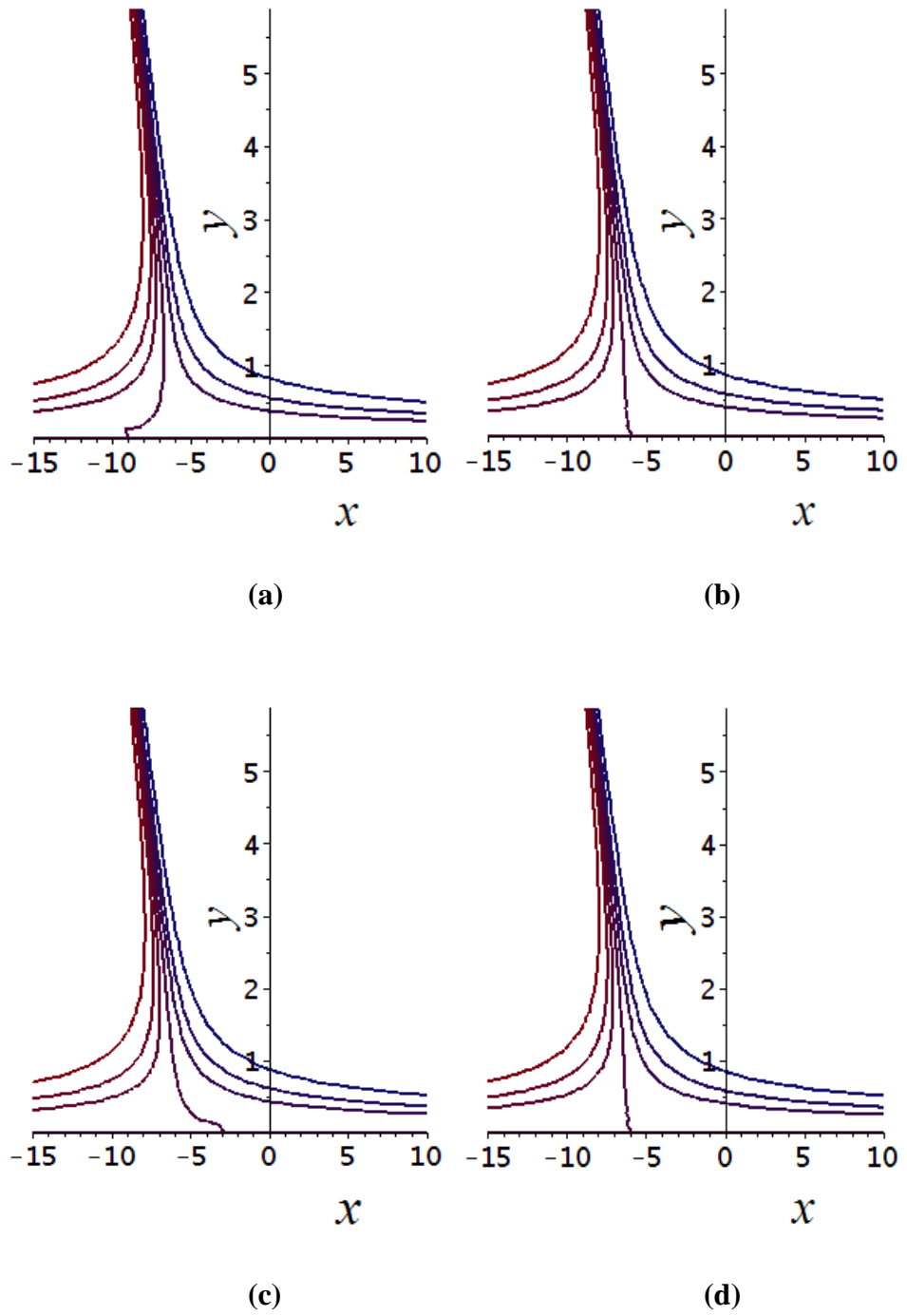


Fig. 3. 11. Shows the streamlines of $Cu - Water$ nanofluid when $\frac{b}{a} = 1$, $\mathbb{B} - \mathbb{A} = -5 - \mathbb{A}$, $K = 1$, $\Omega = 0.5$, $\varepsilon = 0.2$, $t = 0$. (a) $t = 0$, (b) $t = \frac{\pi}{2}$, (c) $t = \pi$, (d) $t = \frac{3\pi}{2}$.

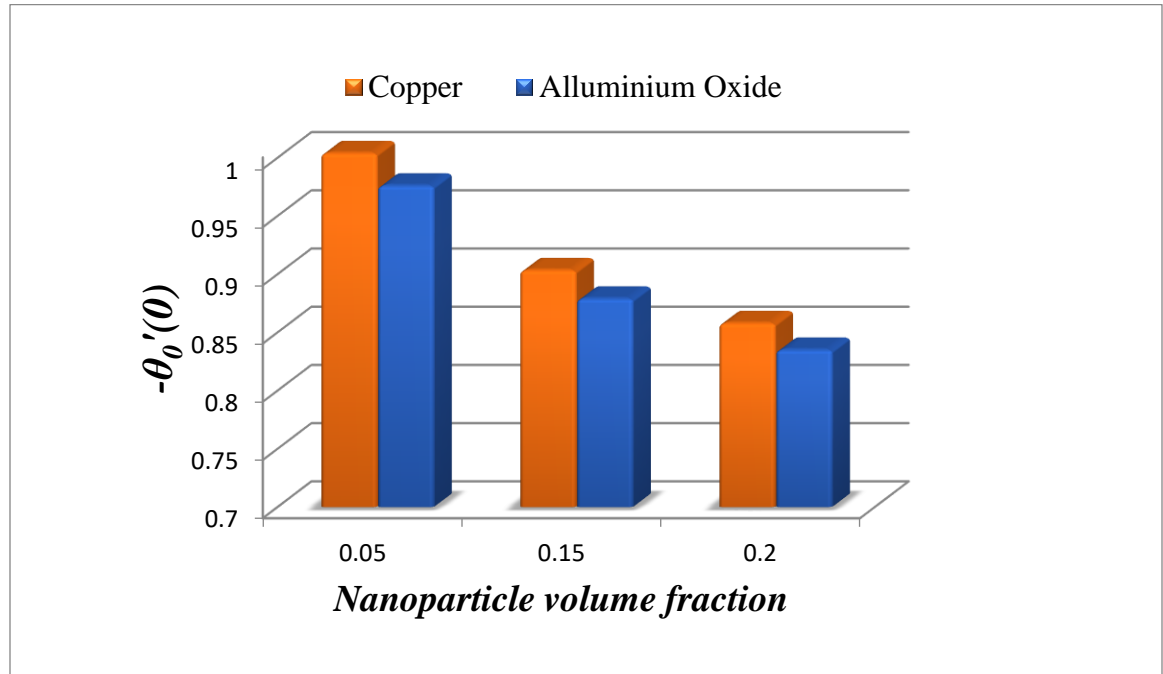


Fig. 3. 12. Bar graph comparison of two nanoparticles concentrations 5%, 15% and 20% respectively.

Table. 3. 1. Validation of results for $f''(0)$ when $\varphi = 0$ and $K = 0$.

M	\mathbb{A}		$f''(0)$	
	Present	[73]	Present	[73]
0	0.647901	0.6479	1.232588	1.2326
1	0.541007	0.5410	1.585331	1.5853
2	0.393589	0.3936	2.346663	2.3467
5	0.190729	0.1907	5.147964	5.1480
10	0.098774	0.0988	10.074741	10.0747

Table. 3. 2. Validation of results for $g_0'(0)$ when $\varphi = 0$ and $K = 0$.

Table 3.2.			
M	$\mathbb{B} - \mathbb{A}$	$g_0'(0)$	
		[73]	Present
0	$-\mathbb{A} = -0.647901$	1.4065	1.406545
	0	0.6080	0.607950
	$\mathbb{A} = 0.647901$	-0.1906	-0.190645
1	$-\mathbb{A} = -0.541007$	1.4240	1.423990
	0	0.5663	0.566316
	$\mathbb{A} = 0.541007$	-0.2913	-0.291360
2	$-\mathbb{A} = -0.393589$	1.4541	1.454064
	0	0.5304	0.530442
	$\mathbb{A} = 0.393589$	-0.3932	-0.393181
5	$-\mathbb{A} = -0.190729$	1.4880	1.488171
	0	0.5063	0.506303
	$\mathbb{A} = 0.190729$	-0.4754	-0.475564
10	$-\mathbb{A} = -0.098774$	1.4970	1.496769
	0	0.5016	0.501643
	$\mathbb{A} = 0.098774$	-0.4937	-0.493483

Table. 3. 3(a). Numerical value of \mathbb{A} and $f''(0)$.

<i>Cu – Water</i>						
M	K	φ	$n = 0.0$		$n = 0.5$	
			\mathbb{A}	$f''(0)$	\mathbb{A}	$f''(0)$
10^{-7}	1	0.1	0.722568	1.069269	0.647978	1.233009
10^{-6}			0.644688	1.264293	0.573809	1.440364
10^{-5}			0.142575	6.935249	0.116581	7.227920
10^{-7}	2		0.848297	0.868343	0.732395	1.09084
	3		0.950844	0.742678	0.808043	0.988713
	4		1.039219	0.655790	0.877179	0.910772
	1	0.05	0.782726	0.972330	0.696955	1.140483
		0.15	0.680741	1.139190	0.615133	1.293535
		0.2	0.657732	1.185850	0.599389	1.327287

Table. 3. 3(b). Numerical value of \mathbb{A} and $f''(0)$.

<i>Al₂O₃ – Water</i>						
M	K	φ	$n = 0.0$		$n = 0.5$	
			\mathbb{A}	$f''(0)$	\mathbb{A}	$f''(0)$
10^{-7}	1	0.1	0.846878	0.903951	0.762347	1.047950
10^{-6}			0.770550	1.040532	0.689359	1.194029
10^{-5}			0.185034	5.324346	0.152298	5.584560
10^{-7}	2		0.990380	0.730675	0.861656	0.927134
	3		1.107115	0.623266	0.950585	0.840333
	4		1.207568	0.549524	1.031693	0.774098
	1	0.05	0.861087	0.877879	0.769082	1.033635
		0.15	0.835022	0.919714	0.756813	1.050349
		0.2	0.833913	0.925333	0.753188	1.061526

Table. 3. 4(a). Numerical value of $g_0'(0)$.

<i>Cu – Water</i>						
M	K	φ	$n = 0.0$		$n = 0.5$	
			$\mathbb{B} - \mathbb{A}$	$g_0'(0)$	$\mathbb{B} - \mathbb{A}$	$g_0'(0)$
10^{-7}	1	0.1	-0.722568	1.271410	-0.647978	1.406550
			0	0.498790	0	0.607587
			0.722568	-0.273830	0.647978	-0.191375
10^{-6}			-0.644688	1.294936	-0.573809	1.408199
			0	0.479861	0	0.581705
			0.644688	-0.335214	0.573809	-0.244789
10^{-5}			-0.142575	1.459372	-0.116581	1.366378
			0	0.470574	0	0.523735
			0.142575	0.518223	0.116581	-0.318907
10^{-7}	2		-0.848297	1.185937	-0.732395	1.406516
			0	0.449325	0	0.607585
			0.848297	-0.287287	0.732395	-0.191346
	3		-0.950844	1.126700	-0.808043	1.406519
			0	0.420537	0	0.607598
			0.950844	-0.285624	0.808043	-0.191322
	4		-1.039219	1.083121	-0.877179	1.406571
			0	0.401646	0	0.607674
			1.039219	-0.279829	0.877179	-0.191222
	1	0.05	-0.782726	1.253428	-0.696955	1.406544
			0	0.489102	0	0.607715
			0.782726	-0.275223	0.696955	-0.191113
		0.15	-0.680741	1.253428	-0.615133	1.406544
			0	0.489102	0	0.607715
			0.680741	-0.275223	0.615133	-0.191113
		0.2	-0.657732	1.253428	-0.599389	1.406544
			0	0.489102	0	0.607715
			0.657732	-0.275223	0.599389	-0.191113

Table 3.4(b). Numerical value of $g_0'(0)$.

<i>Al₂O₃ – Water</i>						
<i>M</i>	<i>K</i>	φ	<i>n</i> = 0.0		<i>n</i> = 0.5	
			$\mathbb{B} - \mathbb{A}$	$g_0'(0)$	$\mathbb{B} - \mathbb{A}$	$g_0'(0)$
10^{-7}	1	0.1	- 0.838110	1.263658	- 0.754251	1.406554
			0	0.497639	0	0.607660
			0.838110	- 0.268379	0.754251	- 0.191234
10^{-6}			- 0.763937	1.282825	- 0.683338	1.407946
			0	0.481221	0	0.585292
			0.763937	- 0.320383	0.683338	- 0.237360
10^{-5}			- 0.184939	1.450722	- 0.152254	1.371608
			0	0.465719	0	0.520896
			0.184939	- 0.519283	0.152254	- 0.329814
10^{-7}	2		-0.980384	1.171577	-0.852508	1.406571
			0	0.447083	0	0.607713
			0.980384	-0.277409	0.852508	-0.191145
	3		-1.096144	1.109010	-0.940504	1.406727
			0	0.418007	0	0.607960
			1.096144	-0.272996	0.940504	-0.190805
	4		-1.195780	1.063927	-1.020783	1.407090
			0	0.399428	0	0.608598
			1.195780	-0.265071	1.020783	-0.189894
	1	0.05	-0.861087	1.247827	-0.769082	1.406550
			0	0.488260	0	0.607789
			0.861087	-0.271306	0.769082	-0.190972
		0.15	-0.835022	1.247827	-0.756813	1.406550
			0	0.488260	0	0.607789
			0.835022	-0.271306	0.756813	-0.190972
		0.2	-0.833913	1.247827	-0.753188	1.406550
			0	0.488260	0	0.607789
			0.833913	-0.271306	0.753188	-0.190972

Table 3. 5(a). Numerical value of $-\Phi_0'(0)$, $\Phi_2'(0)$ and $\Phi_4'(0)$.

<i>Cu – Water</i>								
<i>M</i>	<i>K</i>	φ	<i>n = 0.0</i>			<i>n = 0.5</i>		
			$-\Phi_0'(0)$	$\Phi_2'(0)$	$\Phi_4'(0)$	$-\Phi_0'(0)$	$\Phi_2'(0)$	$\Phi_4'(0)$
10^{-7}	1	0.1	0.691779	0.085912	0.010277	0.813191	0.093913	0.011531
10^{-6}			0.945615	0.050471	0.003659	1.083458	0.055256	0.003881
10^{-5}			6.877988	0.000465	0.000018	7.116813	0.010491	0.000744
10^{-7}	2		0.551502	0.069872	0.007756	0.719432	0.083075	0.010198
	3		0.466232	0.058929	0.006346	0.652080	0.075288	0.009240
	4		0.408703	0.051265	0.005471	0.600686	0.069334	0.008499
	1	0.05	0.625838	0.078389	0.009190	0.751624	0.087123	0.010723
		0.15	0.625838	0.078389	0.009190	0.751624	0.087123	0.010723
		0.2	0.625838	0.078389	0.009190	0.751624	0.087123	0.010723

Table 3.5(b). Numerical value of $-\Phi_0'(0)$, $\Phi_2'(0)$ and $\Phi_4'(0)$.

<i>Al₂O₃ – Water</i>								
<i>M</i>	<i>K</i>	φ	<i>n = 0.0</i>			<i>n = 0.5</i>		
			$-\Phi_0'(0)$	$\Phi_2'(0)$	$\Phi_4'(0)$	$-\Phi_0'(0)$	$\Phi_2'(0)$	$\Phi_4'(0)$
10^{-7}	1	0.1	0.589384	0.073201	0.008584	0.698279	0.080806	0.009934
10^{-6}			0.766655	0.047268	0.003592	0.888616	0.051682	0.003936
10^{-5}			5.270802	0.000533	0.000015	5.491650	0.006956	0.000369
10^{-7}	2		0.467838	0.058713	0.006477	0.617781	0.071474	0.008779
	3		0.394924	0.049220	0.005321	0.559961	0.064732	0.007922
	4		0.346119	0.042662	0.004559	0.515870	0.059506	0.007218
	1	0.05	0.567381	0.071016	0.008240	0.685102	0.079566	0.009805
		0.15	0.567381	0.071016	0.008240	0.685102	0.079566	0.009805
		0.2	0.567381	0.071016	0.008240	0.685102	0.079566	0.009805

Table 3. 6(a). Numerical value of $-\theta_0'(0)$, $\Theta_{12}'(0)$ and $\Theta_{14}'(0)$.

<i>Cu – Water</i>								
<i>M</i>	<i>K</i>	φ	<i>n = 0.0</i>			<i>n = 0.5</i>		
			$-\theta_0'(0)$	$\Theta_{12}'(0)$	$\Theta_{14}'(0)$	$-\theta_0'(0)$	$\Theta_{12}'(0)$	$\Theta_{14}'(0)$
10^{-7}	1	0.1	0.976002	0.625531	0.894378	1.010236	0.511496	0.817287
10^{-6}			1.014206	0.502684	0.810538	1.047785	0.415034	0.743960
10^{-5}			1.416020	0.094820	0.374691	1.434746	0.087727	0.361806
10^{-7}	2		0.926816	0.852550	1.026503	0.976897	0.628893	0.895597
	3		0.891638	1.077594	1.138896	0.950471	0.746466	0.965929
	4		0.864509	1.301745	1.238182	0.928661	0.864375	1.030293
	1	0.05	1.003951	0.899119	1.094526	1.043860	0.713781	0.987421
		0.15	0.903354	0.596328	0.841090	0.938019	0.479655	0.762802
		0.2	0.857919	0.490484	0.741267	0.890235	0.397167	0.674087

Table 3.6(b). Numerical value of $-\theta_0'(0)$, $\Theta_{12}'(0)$ and $\Theta_{14}'(0)$.

<i>Al₂O₃ – Water</i>								
<i>M</i>	<i>K</i>	φ	<i>n = 0.0</i>			<i>n = 0.5</i>		
			$-\theta_0'(0)$	$\Theta_{12}'(0)$	$\Theta_{14}'(0)$	$-\theta_0'(0)$	$\Theta_{12}'(0)$	$\Theta_{14}'(0)$
10^{-7}	1	0.1	0.932422	0.834821	1.016303	0.966518	0.675214	0.924473
10^{-6}			0.964089	0.686724	0.931296	0.997735	0.559994	0.850331
10^{-5}			1.360115	0.111887	0.405929	1.380663	0.102134	0.389729
10^{-7}	2		0.884116	1.152682	1.172595	0.933797	0.838537	1.017006
	3		0.849870	1.468078	1.304933	0.907950	1.002624	1.100002
	4		0.823621	1.782222	1.421429	0.886673	1.167569	1.175876
	1	0.05	0.976038	1.077483	1.185520	1.015805	0.849488	1.066400
		0.15	0.878960	0.709963	0.908840	0.913561	0.567020	0.821797
		0.2	0.835014	0.581655	0.799721	0.867296	0.467622	0.725061

3.5 Conclusion

In this exploration we characterize the flow and heat transport in micropolar nanofluid along oblique stagnation point over an oscillatory plate. Two different metallic nanoparticles are considered (Alumina and Copper) in base fluid water. The governing coupled system is solved numerically by using BVP solution method with the aid of Maple software shooting scheme along with fifth order Runge–Kutta–Fehlberg algorithm. Analysis has been made in order to report the influence of different parameters namely, nanoparticles volume fraction ϕ , Hartmann number M , and material parameter K on velocity, temperature, local wall shear stress and heat transfer rate are examined fixing the Prandtl number Pr (i.e. 6.2) for water. The key finding of current analysis is itemized as follows

- It is observed that the momentum boundary layer is thicker in the case of Al_2O_3 /water as compared to Cu /water. In addition, Al_2O_3 /water results show more surface temperature while Cu /water generates the lowest surface temperature.
- Thickness decline is found for momentum boundary layer against increasing value of nanoparticles volume fraction while inverse trend towards material parameter is observed. Further, the thickness of momentum boundary layer is thin for the case of weak concentration as compared to strong concentration.
- The local wall shear stress is the increasing function of Hartmann number and material parameter while it shows opposite attitude towards nanoparticles volume fraction. It was also noticed that $Cu - water$ with the comparison of $Al_2O_3 - water$ gives maximum local wall shear stress.
- The magnitude of heat transfer rate is significantly large for $Cu - water$ as compared to $Al_2O_3 - water$. On the other hand, the heat transfer rate near the plate surface is decreasing function of Hartmann number while opposite trend is found for both material parameter and nanoparticles volume fraction.
- The zero-skin fraction and stagnation point remarkably depend on $\mathbb{B} - \mathbb{A}$ and time t .

Chapter # 4

Model based study of SWCNT and MWCNT thermal conductivities effect on the heat transfer due to the oscillating wall conditions

4.1 Introduction

In this chapter, different proposed theoretical models for the thermal conductivity of Carbon nanotubes are analyzed. Both SWCNT and MWCNT are discussed in three types of base fluids namely ethylene glycol, engine oil and water. By using the fundamental governing laws and their modifications for the presence of solid concentrations are used to mathematically model the differential equations. The complicated coupled system of differential equations is transformed into non-dimensional form via a suitable similarity transformation. Then numerical results have been obtained by using the midpoint method with Richardson extrapolation enhancement. The numerical results can be computed when the length “ L ” and diameter “ d ” of CNT’s are $3\mu\text{m} \leq L \leq 70\mu\text{m}$ and $10\text{nm} \leq d \leq 40\text{nm}$.

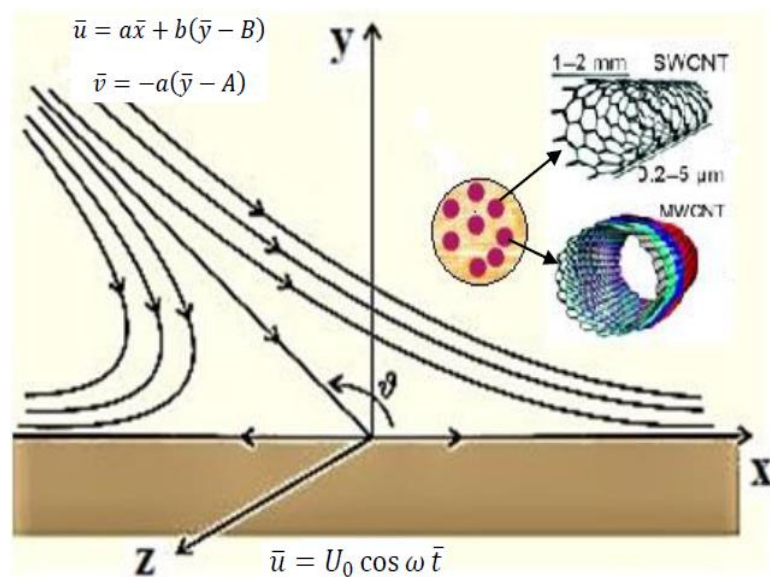


Fig. 4. 1. Functional Diagram.

4.2 Problem description and governing equations:

Consider the problem of stagnation point flow over an oscillatory surface with velocity $U_0 \cos \omega \bar{t}$. The \bar{x} -coordinate is taken horizontally and the \bar{y} -coordinate is considered perpendicular to horizontal direction and is pointed in outward direction towards the fluid as shown in **Fig. 4.1**. The fluid impinges obliquely to the oscillatory surface. It is assumed that free stream velocity is of the form $\bar{\mathbf{V}} = (a\bar{x} + b(\bar{y} - B), -a(\bar{y} - A), 0)$, where a and b are constant. The governing equations of fluid flow can be written as

$$\begin{aligned} \bar{\nabla} \cdot \bar{\mathbf{V}} &= 0, \\ \left(\frac{\partial \bar{\mathbf{V}}}{\partial \bar{t}} + (\bar{\mathbf{V}} \cdot \bar{\nabla}) \bar{\mathbf{V}} \right) &= -\frac{1}{\rho_{nf}} \bar{\nabla} \bar{p} + \frac{\mu_{nf}}{\rho_{nf}} \bar{\nabla}^2 \bar{\mathbf{V}}, \\ \left(\frac{\partial \bar{T}}{\partial \bar{t}} + (\bar{\mathbf{V}} \cdot \bar{\nabla}) \bar{T} \right) &= \alpha_{nf} \bar{\nabla}^2 \bar{T}, \end{aligned} \quad (4.1)$$

where μ_{nf}, ρ_{nf} and α_{nf} are defined in **Table 1.1**. For system (4.1) we append the boundary condition:

$$\begin{aligned} \bar{u} &= U \cos \omega \bar{t}, \quad \bar{v} = 0, \quad \bar{T} = \bar{T}_w + \epsilon(\bar{T}_w - \bar{T}_\infty) \text{Re}(e^{i\omega \bar{t}}) \quad \text{at } \bar{y} = 0, \\ \bar{u} &= a\bar{x} + b(\bar{y} - B), \quad \bar{v} = -a(\bar{y} - A), \quad \bar{T} = \bar{T}_\infty \quad \text{as } \bar{y} \rightarrow \infty. \end{aligned} \quad (4.2)$$

From (4.2)_{4,5}, the stagnation point is $(\frac{b}{a}(B - A), A)$ and hyperbolic streamlines asymptotes are

$$\bar{y} = -\frac{2a}{b}\bar{x} + 2B - A, \quad \bar{y} = A \quad (4.3)$$

They are also well known as degenerate stream-lines. Now, consider

$$\bar{v} = -a\bar{f}(\bar{y}), \quad \bar{u} = a\bar{x}\bar{f}'(\bar{y}) + b\bar{g}(\bar{y}, \bar{t}), \quad (4.4)$$

Eqs. (4.1)₂ and (4.2)_{1,2,4,5} can be written as

$$a\bar{x} \left[a\bar{f}'^2 - a\bar{f}\bar{f}'' - v_{nf}\bar{f}''' \right] + b[\bar{g}_{\bar{t}} + a(\bar{g}\bar{f}' - \bar{f}\bar{g}') - v_{nf}\bar{g}''] = -\frac{1}{\rho_{nf}} \frac{\partial \bar{p}}{\partial \bar{x}}, \quad (4.5)$$

$$a^2\bar{f}\bar{f}' + v_{nf}\bar{f}'' = -\frac{1}{\rho_{nf}} \frac{\partial \bar{p}}{\partial \bar{y}}, \quad (4.6)$$

$$\left. \begin{aligned} \bar{f}(0) = 0, \bar{f}'(0) = 0, \bar{g}(0, \bar{t}) = \frac{U}{b} \operatorname{Re}(e^{i\omega\bar{t}}), \\ \bar{g}'(\bar{y}, \bar{t}) = 1, \bar{f}'(\bar{y}) = 1, \quad \text{as } \bar{y} \rightarrow \infty. \end{aligned} \right\} \quad (4.7)$$

From (4.7)_{4,5} the values of $\bar{f}(\bar{y})$ and $\bar{g}(\bar{y}, \bar{t})$ can be calculated as

$$\bar{f}(\bar{y}) \sim \bar{y} - A, \quad \bar{g}(\bar{y}, \bar{t}) \sim \bar{y} - B. \quad (4.8)$$

From Eqs. (4.5-4.6), we find the pressure field as

$$\bar{p}_0 - \bar{p}(\bar{x}, \bar{y}) = \rho_{nf} \left\{ v_{nf} a\bar{f}' + \frac{a^2}{2} (\bar{x}^2 + \bar{f}^2 - 2\frac{b}{a}(B-A)\bar{x}) \right\}, \quad (4.9)$$

in which \bar{p}_0 is the stagnation pressure. From Eq. (4.9), it is clearly seen that maximum pressure occurs at the stagnation point in through-out the flow domain. Thus Eqs. (4.5)-(4.6) imply that

$$\begin{aligned} \frac{1}{a} v_{nf} \bar{f}'''' - \bar{f}'^2 + \bar{f}\bar{f}'' + 1 &= 0, \\ v_{nf} \bar{g}'' - \bar{g}\bar{f}' - \frac{1}{a} \bar{g}_{\bar{t}} + \bar{f}\bar{g}' &= (B - A). \end{aligned} \quad (4.10)$$

The following similarity variables are presented to make simpler the mathematical analysis of the problem

$$\begin{aligned} f(y) &= \sqrt{\frac{a}{v_f}} \bar{f} \left(\sqrt{\frac{v_f}{a}} y \right), \quad y = \sqrt{\frac{a}{v_f}} \bar{y}, \quad t = \omega \bar{t}, \\ g(y, t) &= \sqrt{\frac{a}{v_f}} \bar{g} \left(\sqrt{\frac{v_f}{a}} y, \frac{t}{\omega} \right) = g_0(y) + \varepsilon g_1(y) e^{it}, \end{aligned} \quad (4.11)$$

$$\theta(y, t) = \frac{T - T_\infty}{T_w - T_\infty} = \theta_0(y) + \varepsilon \theta_1(y) e^{it}.$$

Using the above similarity variables, Eqs. (4.10) and (4.1)₃ together with boundary conditions (4.7) and (4.2)_{3,6} reduce to

$$\begin{aligned} \frac{\mu_{nf}}{\mu_f} \frac{\rho_f}{\rho_{nf}} f''' - f'^2 + ff'' + 1 &= 0, \\ \frac{\mu_{nf}}{\mu_f} \frac{\rho_f}{\rho_{nf}} g_0'' + fg_0' - g_0f' - (\mathbb{B} - \mathbb{A}) &= 0, \\ \frac{\mu_{nf}}{\mu_f} \frac{\rho_f}{\rho_{nf}} g_1'' + fg_1' - g_1f' - i\Omega g_1 &= 0, \\ \frac{k_{nf}}{k_f} \theta_0'' + Pr \frac{(\rho C_p)_{nf}}{(\rho C_p)_f} f \theta_0' &= 0, \\ \frac{k_{nf}}{k_f} \theta_1'' + Pr \frac{(\rho C_p)_{nf}}{(\rho C_p)_f} f \theta_1' - i\Omega Pr \frac{(\rho C_p)_{nf}}{(\rho C_p)_f} \theta_1 &= 0, \end{aligned} \quad (4.12)$$

$$\left. \begin{aligned} f(0) = 0, f'(0) = 0, g_0(0) = 0, g_1(0) = 1, \theta_0(0) = 1 = \theta_1(0), \\ g_1(y) = 0, f'(y) = 1 = g_0'(y), \theta_0(y) = 0, \theta_1(y) = 0, \quad y \rightarrow \infty, \\ g(y) \sim y - \beta, f(y) \sim y - \alpha, \quad \text{as } y \rightarrow \infty, \end{aligned} \right\} \quad (4.13)$$

where

$$\mathbb{B} = B \sqrt{\frac{a}{v_f}}, \quad \mathbb{A} = A \sqrt{\frac{a}{v_f}}, \quad \Omega = \frac{\omega}{a}, \quad Pr = \frac{v_f}{k_f}, \quad \varepsilon = \frac{U}{b} \sqrt{\frac{a}{v_f}}.$$

The different models of effective thermal conductivity are

4.2.1 Hamilton and Crosser model [59]:

$$\frac{k_{nf}}{k_f} = \frac{k_s + (n-1)k_f + (n-1)\varphi(k_s - k_f)}{k_s + (n-1)k_f + (n-1)\varphi(k_s - k_f)}. \quad (4.14)$$

in which n represents the empirical value of particles shape.

Hamilton and Crosser simply correlate n as

$$n = 3\Lambda^{-\delta}, \quad (4.15)$$

where δ is an empirical parameter and Λ is the sphericity defined as

$$\Lambda = \frac{2e(\gamma)[1 - e^2(\gamma)]^{\frac{1}{6}}}{e(\gamma)\sqrt{1 - e^2(\gamma)} + \arcsin(e(\gamma))}, \quad e(\gamma) = \sqrt{1 - \frac{R^2 + \gamma}{(L/2)^2 + \gamma}}.$$

4.2.2 Yamada and Ota model [60]:

$$\frac{k_{nf}}{k_f} = \frac{1 + \frac{k_f L}{k_s R} \varphi^{0.2} + \left(1 - \frac{k_f}{k_s}\right) \varphi \frac{L}{R} \varphi^{0.2} + 2\varphi \frac{k_s}{k_s - k_f} \ln\left(\frac{k_s + k_f}{2k_f}\right)}{1 - \varphi + 2\varphi \frac{k_f}{k_s - k_f} \ln\left(\frac{k_s + k_f}{2k_f}\right)}, \quad (4.16)$$

where R and L are the radius and length of the nanotube, respectively

4.2.3 Xue model [62]:

$$\frac{k_{nf}}{k_f} = \frac{1 - \varphi + 2\varphi \frac{k_s}{k_s - k_f} \ln\left(\frac{k_s + k_f}{2k_f}\right)}{1 - \varphi + 2\varphi \frac{k_f}{k_s - k_f} \ln\left(\frac{k_s + k_f}{2k_f}\right)}, \quad (4.17)$$

The surface shear stress (C_f) and heat transfer rate (Nu) can be expressed as

$$C_f = \frac{\tau_w}{\frac{1}{2} \rho_f U_w^2}, \quad (4.19)$$

$$Nu = \frac{\bar{x} q_w}{k_f (\bar{T}_w - \bar{T}_\infty)},$$

where q_w , τ_w , are the surface heat flux and the wall shear stress, define as

$$\tau_w = \mu_{nf} \left. \frac{\partial \bar{u}}{\partial \bar{y}} \right|_{\bar{y}=0}, \quad (4.20)$$

$$q_w = -k_{nf} \left. \frac{\partial \bar{T}}{\partial \bar{y}} \right|_{\bar{y}=0}.$$

By the use of Eqs. (4.11), (4.19) and (4.20), we can write

$$\frac{1}{2}Re_{\bar{x}}C_f = \frac{\mu_{nf}}{\mu_f} \left[\sqrt{Re_{\bar{x}}} f''(0) + \frac{b}{a} g'_0(0) + \epsilon \frac{b}{a} e^{it} g'_1(0) \right],$$

$$(Re_{\bar{x}})^{-\frac{1}{2}} Nu = -\frac{k_{nf}}{k_f} \theta'_0(0) - \frac{k_{nf}}{k_f} \epsilon e^{it} \theta_1(0),$$

At the surface $\bar{y} = 0$, three points carry significant importance: the stagnation point towards which the separating streamline far away from the surface are directed, the position where maximum pressure is exerted $\bar{x} = \bar{x}_p$, and the position of zero tangential stress $\bar{x} = \bar{x}_s$. The equation of separating streamline which intersect the boundary is

$$x = \sqrt{\frac{a}{v_f}} \bar{x}, \quad x f(y) + \frac{b}{a} \int_0^y \{ g_0(s) + \epsilon e^{it} g_1(s) \} ds = 0, \quad (4.21)$$

From Eqs. (4.9) and (4.20), we see that

$$\begin{aligned} \bar{x}_p &= \frac{b}{a} \left(\frac{v_f}{a} \right)^{1/2} (\beta - \alpha), \\ \bar{x}_s &= -\frac{b}{a} \left(\frac{v_f}{a} \right)^{1/2} \frac{1}{f''(0)} (g'_0(0) + \epsilon e^{it} g'_1(0)). \end{aligned} \quad (4.22)$$

We note that \bar{x}_p does not depend on φ whereas \bar{x}_s depends on φ . The ratio

$$\frac{\bar{x}_p}{\bar{x}_s} = -(\mathbb{B} - \mathbb{A}) \frac{f''(0)}{(g'_0(0) + \epsilon e^{it} g'_1(0))}$$

is same for all angles of incidence.

4.3 Solution procedure:

Numerical solution of (4.12)₁ together with their boundary conditions in (4.13) has been solved numerically by means of midpoint method with the Richardson extrapolation enhancement.

For Eq. (4.12)₂ the solution is in the form [73]

$$g_0(y) = (\mathbb{A} - \mathbb{B})f' + C_1 f'' \Delta(y), \quad (4.23)$$

with

$$C_1 = f''(0)[g'_0(0) + (\beta - \alpha)f''(0)],$$

$$\Delta(y) = \int_0^y \text{Exp}\left(-\frac{v_f}{v_{nf}} \int_0^s f(\eta) d\eta\right) (f''(s))^{-2} ds.$$

Furthermore, the series solutions of equations (4.12)_{3,5} for small value of frequency Ω have been obtained [66]

$$g_1(y) = \sum_{n=0}^{\infty} (i\Omega)^n \Phi_n(y),$$

and

$$\theta_1(y) = \sum_{n=0}^{\infty} (i\Omega)^n \theta_{1n}(y).$$

In present problem, the real part of the solution is

$$g_1(y) = \Phi_0(y) - \Omega^2 \Phi_2(y) + \Omega^4 \Phi_4(y) \dots,$$

$$\theta_1(y) = \theta_{10}(y) - \Omega^2 \theta_{12}(y) + \Omega^4 \theta_{14}(y) \dots,$$

where

$$\begin{aligned} \frac{\mu_{nf}}{\mu_f} \frac{\rho_f}{\rho_{nf}} \Phi_0'' - \Phi_0 f' + f \Phi_0' &= 0 \\ \frac{\mu_{nf}}{\mu_f} \frac{\rho_f}{\rho_{nf}} \Phi_n'' - \Phi_n f' + f \Phi_n' &= \Phi_{n-1}, \quad n = 1, 2, 3 \dots \\ \Phi_0(0) = 1, \quad \Phi_0(\infty) &= 0 \\ \Phi_n(0) = 0, \quad \Phi_n(\infty) &= 0 \end{aligned} \quad] \quad (4.24)$$

and

$$\left. \begin{aligned} \frac{1}{Pr} \frac{k_{nf}}{k_f} \Theta_{1n}'' + \frac{(\rho C_p)_{nf}}{(\rho C_p)_f} (f \Theta_{1n}' - \Theta_{1(n-1)}) &= 0 \\ \Theta_{1n}(0) = 0, \quad \Theta_{1n}(\infty) &= 0 \end{aligned} \right\}, \quad n = 1, 2, 3 \dots \quad (4.25)$$

where $\Theta_{10}(y) = \theta_0(y)$ which can be obtained from (4.12)₄ as [23]

$$\theta_0(y) = \frac{I_{nf}(Pr, \infty) - I_{nf}(Pr, y)}{I_{nf}(Pr, \infty)}, \quad (4.26)$$

where

$$I_{nf}(Pr, y) = \int_0^y \text{Exp} \left(-Pr \frac{k_f}{k_{nf}} \frac{(\rho C_p)_{nf}}{(\rho C_p)_f} \int_0^s f(\eta) d\eta \right) ds,$$

and

$$I_{nf}(Pr, \infty) = \lim_{y \rightarrow \infty} I_{nf}(Pr, y).$$

The systems (4.19, 4.20) have been solved numerically using midpoint method with the Richardson extrapolation enhancement and the numerical integration for (4.18, 4.21) can be executed easily with aid of any mathematical software as [78].

4.4 Results and Discussion:

Numerical evaluation of the model equations for SWCNT and MWCNT is performed for three different base liquids namely engine oil, ethylene glycol and water. The solid volume fraction φ of the nanoparticles represents up to what fraction of whole liquid solid concentrations are incorporated. Keeping the fluid nature of base materials, it is kept less than 0.5. For water the value of the Prandtl number of water is kept constant at 6.2. The thermophysical properties of base fluids and the nanoparticles are shown in **Table 1.2**. In order to validate the numerical algorithm, the comparison of data is made for the particular case of Cu-Water nanofluid as shown in **Tables 4.1-4.2**. These results are in excellent agreement with the already reported results by [79]. It is convenient to mention that in the original Hamilton & Crosser model, the empirical parameter δ was set as $\delta = 1$. However, in the later studies by Yu et al. [80] and Jiang et al. [81], it was found that $\delta = 1.55$ was more suitable for CNT's

nanofluid. Therefore, in this study, δ is set as 1.55 and the ratio of length to diameter (L/d) is 500.

Figs. 4.2 depict velocity profiles of nanofluid flow in the unsteady domain when, $\varphi = 0.1$, $\mathbb{B} - \mathbb{A} = -\mathbb{A}$, $\varepsilon = 0.2$, $x = 1$, $\Omega = 0.2$. Generally; free stream velocity drives the flow due to the plate oscillation. At the surface the nanofluid is zero and gradually it approaches the free stream velocity as approaches infinity. It satisfies the boundary constraints which also show validity of obtained results. It is observed that $u(x, y, t)$ depicts the same oscillatory behavior as it was in source. Moreover, it is noticed that the amplitude of the oscillation has peak value at the wall and gradually it decreases as move away from the surface. **Figs. 4.3-4.5** are plotted for stream lines in the case of impinging fluids at different angles when $\frac{b}{a} = 1$, $\Omega = 0.5$, $\varepsilon = 0.2$, $t = \pi$. It intersects the surface $\bar{y} = 0$, at the point \bar{x}_s , which is the point of zero velocity that is stagnation point. Its location depends on the value of $\mathbb{B} - \mathbb{A}$, base fluid and time t . From **Fig. 4.3**, it can be observed that for positive value of $\mathbb{B} - \mathbb{A}$, the stagnation point appears on the right side of the plate form origin whereas the opposite behavior can be seen for negative value of $\mathbb{B} - \mathbb{A}$. **Figs. 4.4** predict that for some constant number $\mathbb{B} - \mathbb{A} = -2\mathbb{A}$, the stagnation point location appears in the neighborhood of -2 in case of SWCNT-Water nanofluid, whereas, it appears in the neighborhood of 0 for both SWCNT-Ethylene Glycol and SWCNT-Engine Oil nanofluid. The same situation can be seen for the consideration of MWCNT. Furthermore, the stagnation point has the oscillatory behavior w.r.t time t as seen in **Fig. 4.5**. Isotherms are plotted in **Figs. 4.6** when $\frac{b}{a} = 1$, $\Omega = 0.5$, $\varepsilon = 0.2$. It can be seen that Yamada and Ota model gives the highest temperature as compare to Hamilton & Crosser and Xue model. **Figs. 4.7(a-c)** represents the skin friction coefficient for different base fluids and time t . It can be observed that skin friction coefficient has sinusoidal variation with respect to time and furthermore, engine oil overrated the skin friction coefficient as compared to water and ethylene glycol. **Figs. 4.8-4.10** are constructed for the comparison of different thermal conductivity models. The comparison results show that Yamada model are definitely overrated, while Hamilton & Crosser model and Xue model distinctly underestimate the Nusselt number of CNT nanofluid. It is also seen that Nusselt number has sinusoidal variation with respect to t . It is observed from **Table. 4.4** that MWCNT produce higher skin friction coefficient than SWCNT. Furthermore, Ethylene glycol produced highest skin friction

coefficient followed by water while engine oil produced the lowest skin friction. **Table. 4.5** shows the numerical value of α and it is observed that α and skin friction has same behavior. **Tables. 4.5-4.8** shows the numerical value of Nusselt number for different base fluid and nanoparticles. From these, it is noticed that SWCNT produced the highest value of Nusselt number than MWCNT. Furthermore, ethylene glycol produced highest value of skin friction as compared to that of values for water while engine oil produced the highest Nusselt number. The thermal conductivity of Yamada model is overrated the Nusselt number as compared to Xue and Hamilton & Crosser models.

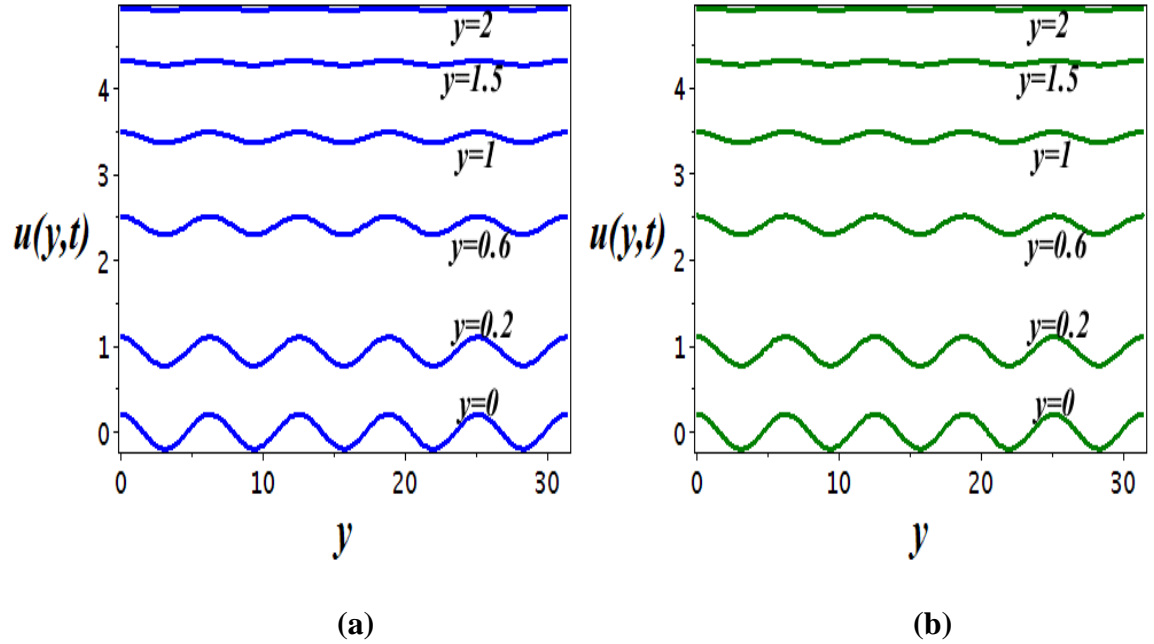


Fig. 4. 2. Time dependent flow of the velocity field $u(y, t)$ at different locations from the wall. The time period is $t \in [0, 10\pi]$ for (a) *SWCNT – Water*. (b) *MWCNT – Water*.

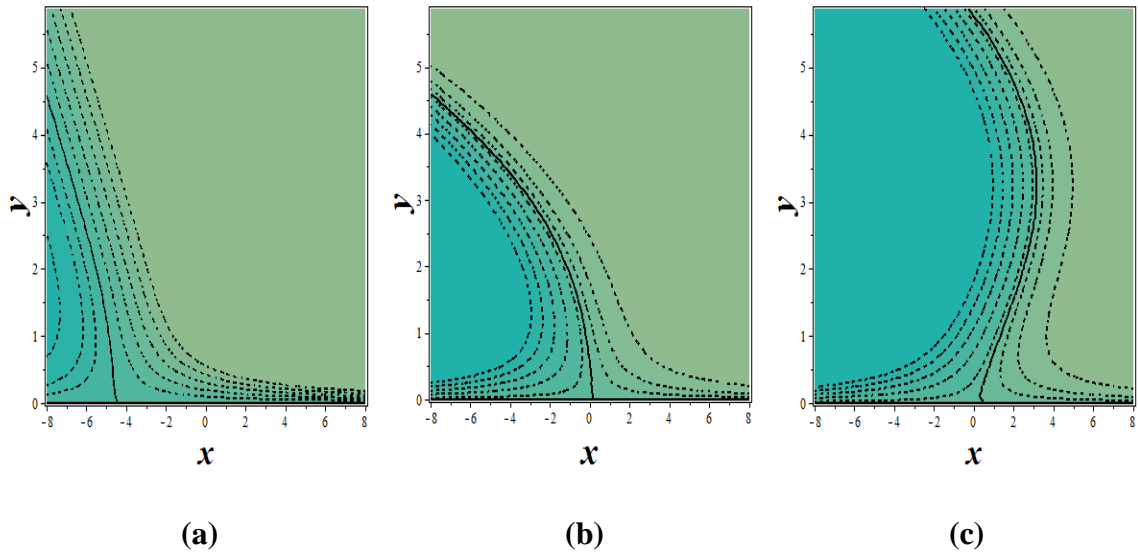


Fig. 4. 3. streamlines pattern for *SWCNT – Water* nanofluid. (a) $\mathbb{B} - \mathbb{A} = -6\mathbb{A}$, (b) $\mathbb{B} - \mathbb{A} = 0$, (c) $\mathbb{B} - \mathbb{A} = 4\mathbb{A}$.

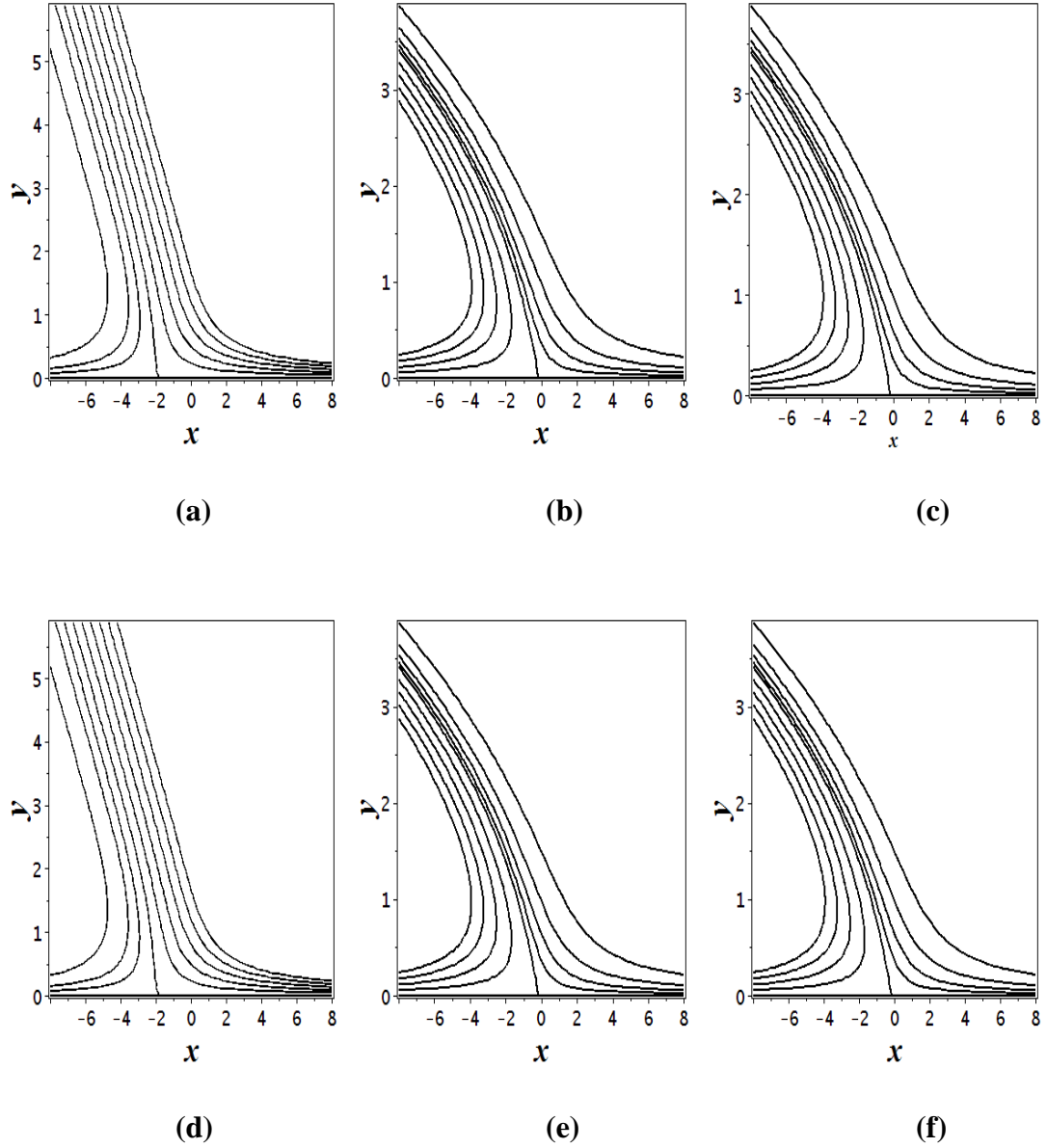


Fig. 4. 4. Streamlines pattern for nanofluids when $\mathbb{B} - \mathbb{A} = -2\mathbb{A}$. **(a)** SWCNT – Water, **(b)** SWCNT – Engine Oil, **(c)** SWCNT – Ethylene Glycol **(d)** MWCNT – Water, **(e)** MWCNT – Engine Oil, **(f)** MWCNT – Ethylene Glycol.

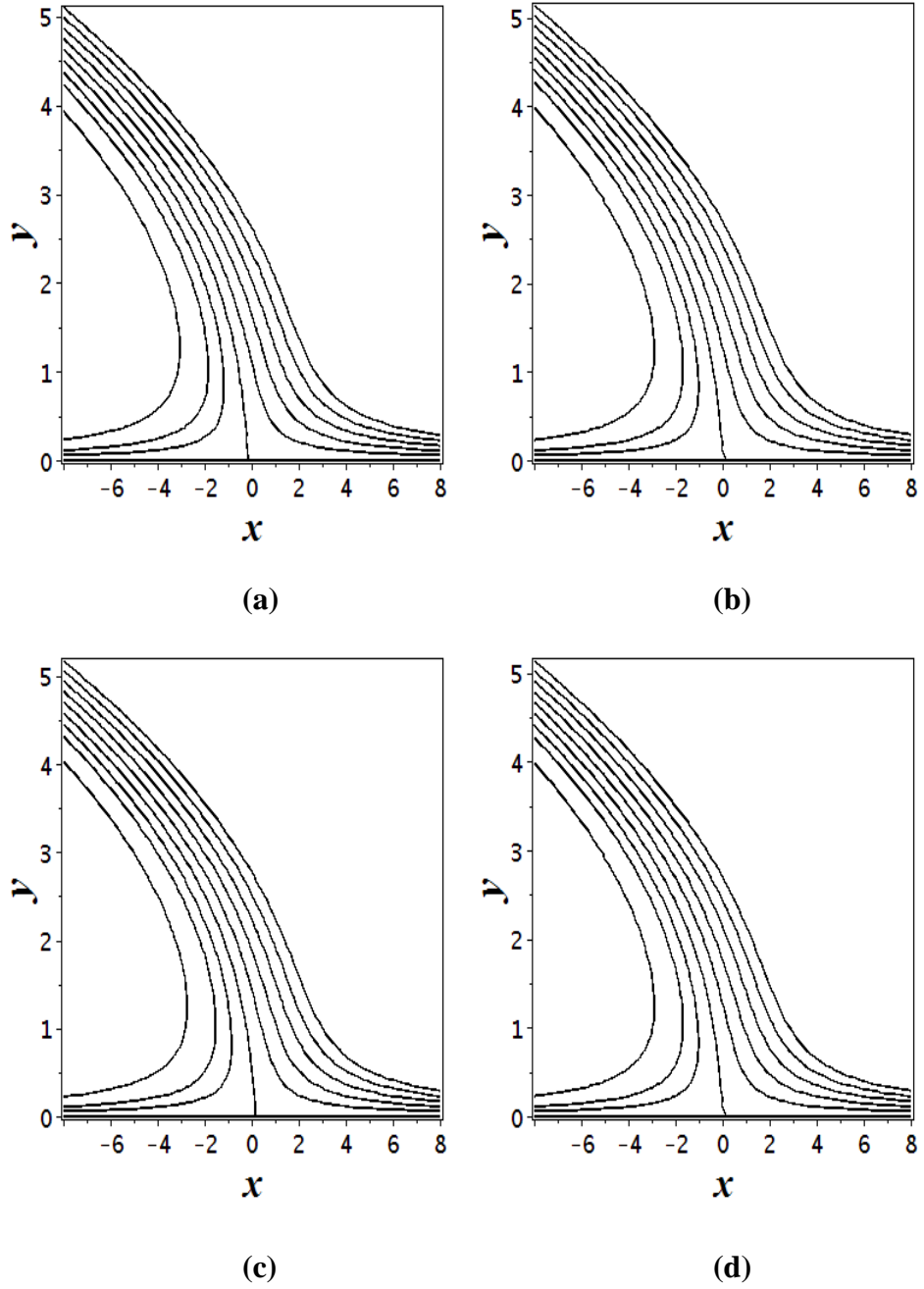


Fig. 4. 5. Streamlines of *SWCNT – Water* nanofluid when $\mathbb{B} - \mathbb{A} = 0$. **(a)** $t = 0$, **(b)** $t = \pi/2$, **(c)** $t = \pi$ **(d)** $t = 3\pi/2$.

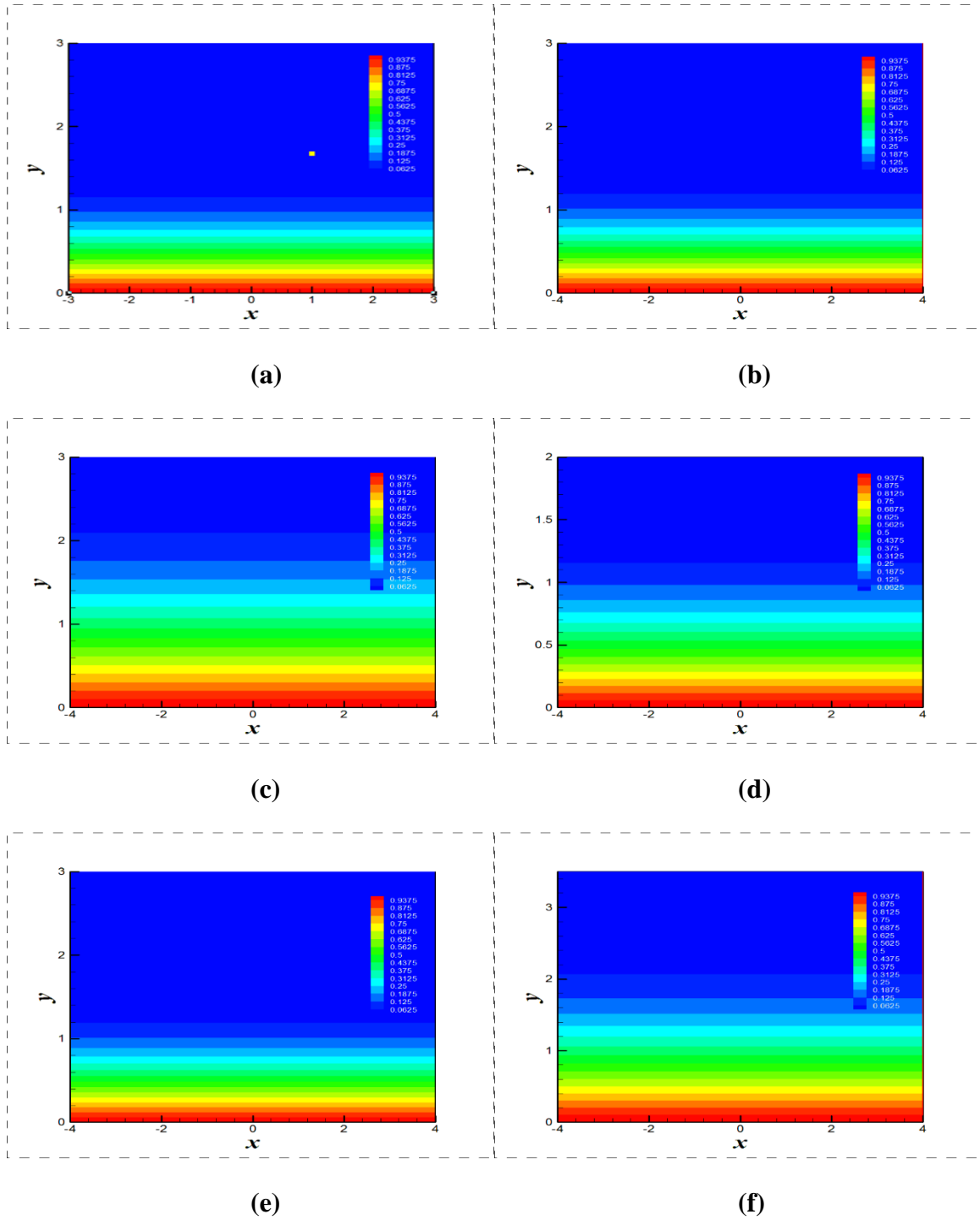


Fig. 4. 6. Variation of isotherms for different nanofluid models, (a) SWCNT, Hamilton & Crosser model, (b) SWCNT, Xue model, (c) SWCNT, Yamada & Otta model, (d) MWCNT, Hamilton & Crosser model, (e) MWCNT, Xue model, (f) MWCNT, Yamada & Otta.

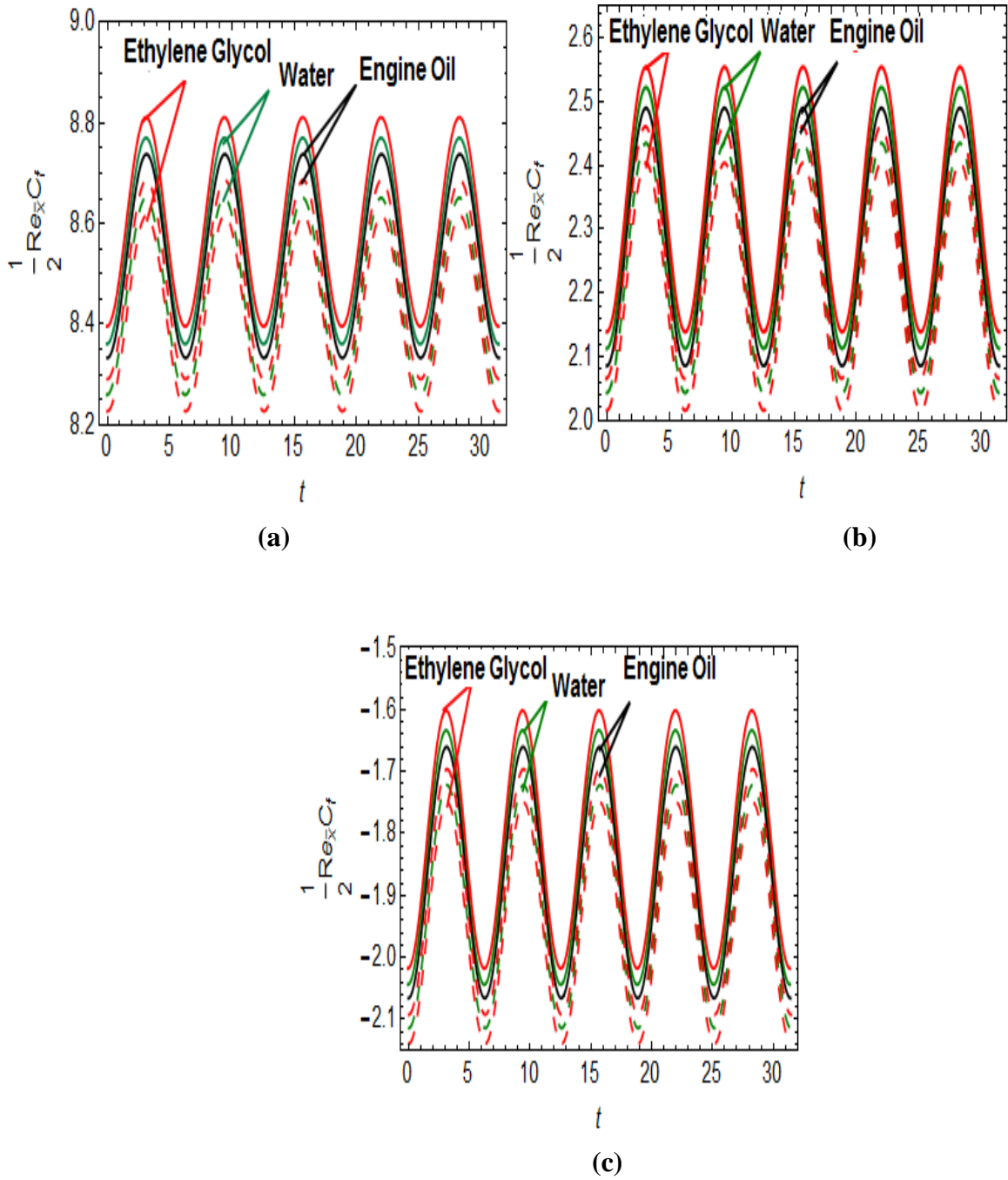


Fig. 4. 7. Shows the skin friction coefficient vs time for different value of *SWCNT* – *Water* nanofluid, (a) $B - A = -5A$, (b) $B - A = A$, (c) $B - A = 5A$. Solid lines for *MWCNT* and dotted lines for *SWCNT*

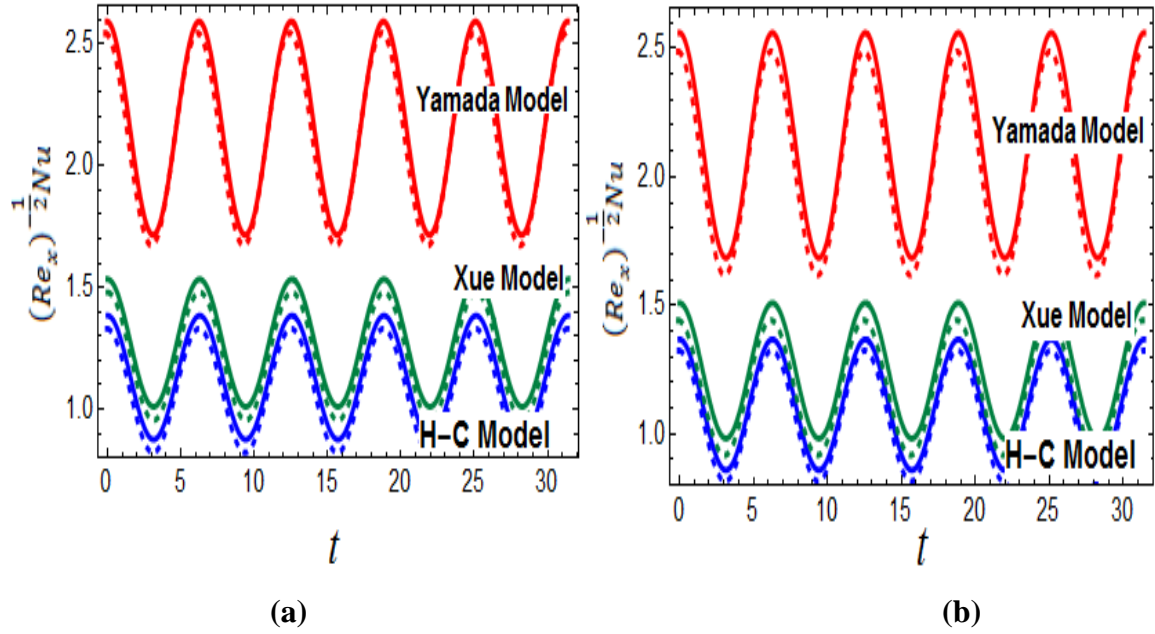


Fig. 4. 8. Shows the Nusselt number vs time for, **(a)** Ethylene Glycol, **(b)** Engine Oil, when $\Omega = 0.5, \varepsilon = 0.2$. SWCNT as nanoparticles.

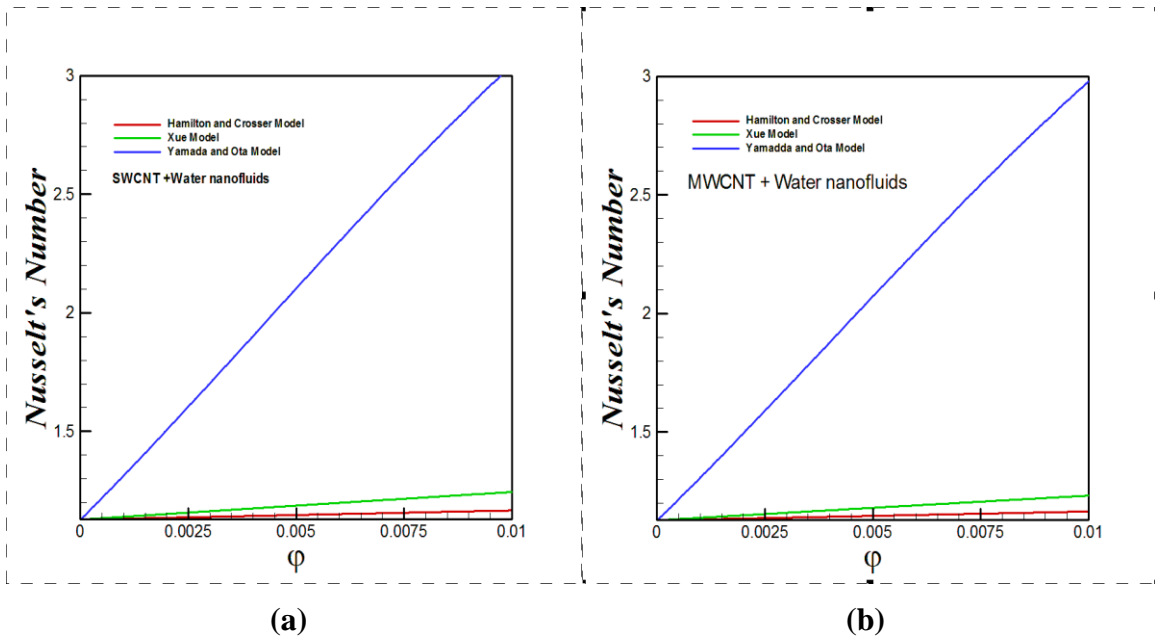


Fig. 4. 9. Comparison of different thermal conductivities models for CNT's nanofluids. **(a)** SWCNT-Water nanofluid, **(b)** MWCNT-Water nanofluid.

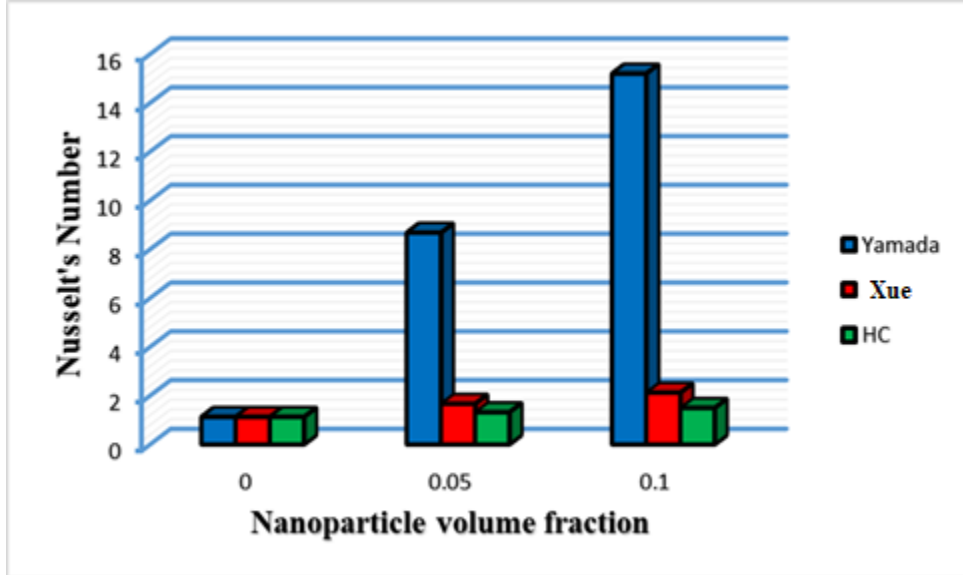


Fig. 4. 10. Bar graph comparison of various models for SWCNTs-water nanofluids when $t = \pi/2$.

Table. 4. 1. Validation of results for $f''(0)$.

φ	A		$f''(0)$	
	[79]	Present	[79]	Present
0.0	0.647900	0.647900	1.232587	1.232587
0.1	0.551523	0.551523	1.447977	1.447977
0.2	0.531918	0.531918	1.501345	1.501345

Table. 4. 2. Validation of results for $g_0'(0)$.

φ	$\mathbb{B} - \mathbb{A}$	$g_0'(0)$	
		[79]	Present
0.0	-0.647900	1.406544	1.406544
	0	0.607950	0.607950
	0.647900	-0.190644	-0.190644
0.1	-0.551523	1.406544	1.406544
	0	0.607949	0.607949
	0.551523	-0.190644	-0.190644
0.2	-0.531918	1.406544	1.406544
	0	0.607949	0.607949
	0.531918	-0.190644	-0.190644

Table. 4. 3. Skin friction variation when $\varepsilon = 0.5, \Omega = 0.5, t = 0, \mathbb{B} - \mathbb{A} = -\mathbb{A}$

φ	Water		Ethylene Glycol		Engine Oil	
	SWCNT	MWCNT	SWCNT	MWCNT	SWCNT	MWCNT
0	1.840537	1.840537	1.840537	1.840537	1.840537	1.840537
0.002	1.842736	1.845192	1.84341	1.845608	1.841921	1.844688
0.004	1.844963	1.849873	1.84631	1.850707	1.843337	1.848865
0.006	1.847218	1.854583	1.849235	1.855836	1.844785	1.853069
0.008	1.849501	1.85932	1.852187	1.860995	1.846265	1.857299
0.01	1.851812	1.864085	1.855165	1.866183	1.847776	1.861555

Table. 4. 4 Numerical values of α when $\varepsilon = 0.5, \Omega = 0.5, t = 0, \mathbb{B} - \mathbb{A} = -\mathbb{A}$

φ	Water		Ethylene Glycol		Engine Oil	
	SWCNT	MWCNT	SWCNT	MWCNT	SWCNT	MWCNT
0	0.647900	0.647900	0.647900	0.647900	0.647900	0.647900
0.002	0.648482	0.649131	0.64866	0.649241	0.648266	0.648998
0.004	0.649071	0.650368	0.649427	0.650588	0.648641	0.650102
0.006	0.649667	0.651611	0.650200	0.651942	0.649024	0.651212
0.008	0.65027	0.652861	0.650979	0.653302	0.649415	0.652328
0.01	0.65088	0.654116	0.651765	0.654669	0.649814	0.65345

Table. 4. 5. Numerical values of Nusselt number when water is considered as a base fluid and $\varepsilon = 0.5$, $\Omega = 0.5$, $t = 0$.

φ	H-C model		Xue model		Yamada model	
	SWCNT	MWCNT	SWCNT	MWCNT	SWCNT	MWCNT
0	1.127964	1.127964	1.127964	1.127964	1.127964	1.127964
0.002	1.135721	1.135432	1.151727	1.149193	1.498869	1.488021
0.004	1.143456	1.142877	1.175238	1.17021	1.906997	1.882497
0.006	1.151171	1.150301	1.198505	1.191022	2.302384	2.264089
0.008	1.158865	1.157701	1.22154	1.211636	2.681222	2.629316
0.01	1.166539	1.165081	1.24435	1.232059	3.044395	2.979113

Table. 4. 6. Numerical values of Nusselt number when Ethylene Glycol is considered as a base fluid and $\varepsilon = 0.5$, $\Omega = 0.5$, $t = 0$.

φ	H-C model		Xue model		Yamada and Ota model	
	SWCNT	MWCNT	SWCNT	MWCNT	SWCNT	MWCNT
0	1.127964	1.127964	1.127964	1.127964	1.127964	1.127964
0.002	1.135754	1.13552	1.154279	1.151799	1.504277	1.499455
0.004	1.143524	1.143054	1.180285	1.175371	1.919267	1.908311
0.006	1.151275	1.150568	1.205996	1.198691	2.321604	2.304388
0.008	1.159007	1.158062	1.231424	1.221768	2.707324	2.68388
0.01	1.16672	1.165535	1.256583	1.244613	3.077293	3.047685

Table. 4. 7. Numerical values of Nusselt number when Engine Oil is considered as a base fluid and $\varepsilon = 0.5$, $\Omega = 0.5$, $t = 0$.

Table 4.7. Numerical values of Nusselt number when Engine Oil is considered as a base fluid and $\varepsilon = 0.5$, $\Omega = 0.5$, $t = 0$.						
φ	Hamilton & Crosser model		Xue model		Yamada and Ota model	
	SWCNT	MWCNT	SWCNT	MWCNT	SWCNT	MWCNT
0	1.127964	1.127964	1.127964	1.127964	1.127964	1.127964
0.002	1.136149	1.135874	1.156284	1.153761	1.506449	1.503488
0.004	1.144319	1.143767	1.184271	1.179273	1.924321	1.917567
0.006	1.152474	1.151644	1.211942	1.204512	2.329807	2.31913
0.008	1.160614	1.159506	1.239313	1.229491	2.718867	2.704247
0.01	1.168741	1.167353	1.2663985	1.254222	3.092342	3.073788

4.5 Conclusion

This chapter is based on the comparison of three different models of effective thermal conductivity and density of nanofluid for three different base fluids namely; Ethylene Glycol, Water and Engine Oil in the presence of carbon nanotubes. The mathematical modelling is being done by using the fundamental governing laws of motion and heat transfer in the form of partial differential equations. A detailed analysis is presented for the unsteadiness effect on the velocity and temperature profiles by considering the oscillating boundary condition for the wall velocity and wall temperature. The important finding of the current study can be summarized as follows:

The isotherms pattern suggests that for both the cases of SWCNT and MWCNT the heat penetration depth proposed by Hamilton & Crosser and Xue model is almost equal, but the heat penetration appeared in isotherms by using the Yamada & Ota model is larger. When comparison is made among the SWCNT and MWCNT for the same model the heat penetration depth for the MWCNT is deeper. In the transient domain, the skin friction produced by Ethylene Glycol Carbon-nanofluid is higher as compared to the water and Engine Oil. Engine oil Carbon-nanofluid has the least skin friction coefficient. The Nusselt number prediction for the CNT's nanofluid is highest for Yamada & Ota model and was lowest for Hamilton &

Crosser model. A big difference is observed between the values of Yamada model and Hamilton & Crosser model. The skin friction behavior prediction is similar for all the three models and it shows decreasing trend with the increase in nanotubes volumetric concentration. Once again, the prediction by Yamada model is higher as compared to the other two models. Overall the skin friction offered due to the presence of MWCNT is higher as compared to the SWCNTs. It can be observed that the stagnation point location appears in the neighborhood of -2 in case of SWCNT-Water nanofluid, whereas, it appears in the neighborhood of 0 for both SWCNT-Ethylene Glycol and SWCNT-Engine Oil nanofluid. The same situation can be seen for the consideration of MWCNT. Furthermore, the stagnation point has the oscillatory behavior w.r.t time t .

Chapter # 5

Unsteady stagnation point flow of viscous nanofluids over the curved shrinking sheet: Existence of multiple solution

5.1 Introduction

This chapter examines possible existence of reverse flow situation in unsteady nanofluid flow over a curved surface. Alumina (Al_2O_3) and Ethylene glycol are considered as nanoparticles and base fluid, respectively. Mathematical form of the problem is obtained by using the fundamental form of governing equations for motion and heat transfer when solid concentrations are added to an ordinary liquid. The complicated coupled unsteady system is transformed into non-dimensional form by use relevant transformations. The solution of the nonlinear problem is produced by use of numerical scheme available in the form of BVP4C package in MATLAB. In the case of surface shrinking towards the surface a reverse flow situation is also developed and requires careful selection of solution by examining the stability of solution. Detailed stability analysis is done, and critical values are determined for possible existence of dual solutions. Various parameters variation is analyzed by plotting graphs and tables. The numerical values are also calculated for the reduced Nusselt number and skin friction due to variation in values of different flow parameters.

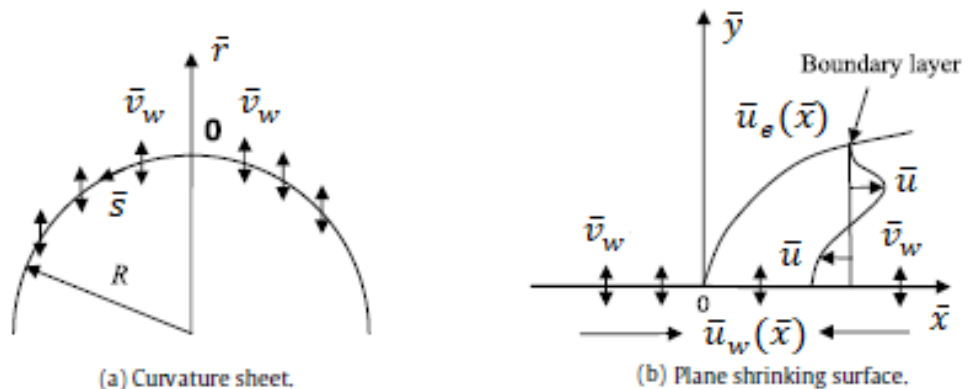


Fig. 5. 1. Geometry of the surfaces (a) Curved surface (b) Boundary layer shrinking surface.

5.2 Problem description and governing equations:

The geometry of the problem is based on the assumption that the flow is generated due to the motion of the curved surface of radius R and the nanofluid is considered above the curved surface. The curvilinear coordinates \bar{r} and \bar{s} are chosen as it is shown in *Fig. 5.1(a)*, the variation in values of R defines the curvedness of surface, the large values of R depict the slight curvedness in surface. The boundary layer formation in shrinking case is shown in *Fig. 1(b)*. However, the free stream velocity in *1(b)* is $\bar{u}_e(\bar{s})/1 - c\bar{t}$. The shrinking velocity of the surface is assumed to be $\bar{u}_w(\bar{s})/1 - c\bar{t}$ along the \bar{s} direction. Mass flux velocity is denoted by $\bar{v}_w(\bar{t})$, where $\bar{v}_w(\bar{t}) < 0$ is for the case of suction and $\bar{v}_w(\bar{t}) > 0$ is for the case of injection, respectively. Under the boundary layer assumption, the fundamental governing laws for motion and thermodynamics are given by, [57],

$$R \frac{\partial \bar{u}}{\partial \bar{s}} + \frac{\partial}{\partial \bar{r}} ((\bar{r} + R)\bar{v}) = 0 \quad (5.1)$$

$$\frac{1}{\rho_{nf}} \frac{\partial p}{\partial \bar{r}} = \frac{\bar{u}^2}{\bar{r} + R} \quad (5.2)$$

$$\frac{1}{\rho_{nf}} \frac{R}{\bar{r} + R} \frac{\partial p}{\partial \bar{s}} = v_{nf} \left(\frac{\partial^2 \bar{u}}{\partial \bar{r}^2} + \frac{1}{\bar{r} + R} \frac{\partial \bar{u}}{\partial \bar{r}} - \frac{\bar{u}}{(\bar{r} + R)^2} \right) - \frac{\partial \bar{u}}{\partial \bar{t}} - \bar{v} \frac{\partial \bar{u}}{\partial \bar{r}} - \frac{R\bar{u}}{\bar{r} + R} \frac{\partial \bar{u}}{\partial \bar{s}} - \frac{\bar{u}\bar{v}}{\bar{r} + R} \quad (5.3)$$

$$\alpha_{nf} \left(\frac{\partial^2 T}{\partial \bar{r}^2} + \frac{1}{\bar{r} + R} \frac{\partial T}{\partial \bar{r}} \right) - \frac{\partial T}{\partial \bar{t}} - \bar{v} \frac{\partial T}{\partial \bar{r}} - \frac{R\bar{u}}{\bar{r} + R} \frac{\partial T}{\partial \bar{s}} = 0 \quad (5.4)$$

According to the physical model the mathematical form of boundary constraints is

$$\bar{t} < 0: \bar{u} = 0, \bar{v} = 0, T = T_\infty \text{ for any } \bar{r} \text{ and } \bar{s}$$

$$\bar{t} \geq 0: \bar{v} = \bar{v}_w(\bar{t}) = -\sqrt{\frac{av_f}{1 - c\bar{t}}} S, \bar{u} = \frac{u_w(\bar{s})}{1 - c\bar{t}} = \frac{b\bar{s}}{1 - c\bar{t}}, T = T_w \text{ at } \bar{r} = 0 \quad (5.5)$$

$$\bar{u} \rightarrow \frac{\bar{u}_e(\bar{s})}{1 - c\bar{t}} = \frac{a\bar{s}}{1 - c\bar{t}}, \frac{\partial \bar{u}}{\partial \bar{s}} \rightarrow 0, T \rightarrow T_\infty \text{ as } \bar{r} \rightarrow \infty$$

where $c > 0$ for an accelerated sheet and $c < 0$ for a decelerated sheet, respectively. S is the constant wall mass transfer parameter, with $S > 0$ for suction and $S < 0$ for injection, respectively.

5.2.1 Steady-state case

Following similarity variables are used to non-dimensionalize the problem, where the primes symbol represents the derivative w.r.t to non-dimensional variable r , the use of transformation given below produce the non-dimensional form Eqs. (5.1)–(5.5).

$$\bar{u} = \frac{\bar{u}_e}{1 - c\bar{t}} f'(r), \quad \bar{v} = -\frac{R}{\bar{r} + R} \sqrt{\frac{v_f \bar{u}_e}{(1 - c\bar{t})\bar{s}}} f(r), \quad r = \sqrt{\frac{\bar{u}_e}{v_f(1 - c\bar{t})\bar{s}}} \bar{r} \quad c < 0 \quad (5.6)$$

$$\bar{p} = \frac{\rho_f \bar{u}_e^2}{(1 - c\bar{t})^2} p(r), \quad \theta(r) = \frac{T - T_\infty}{T_w - T_\infty} \quad]$$

$$\frac{\rho_f}{\rho_{nf}} \frac{\partial p}{\partial r} = \frac{1}{r + K} f'^2 \quad (5.7)$$

$$\frac{\rho_f}{\rho_{nf}} \frac{2K}{r + K} p = \frac{v_{nf}}{v_f} \left(f''' + \frac{1}{r + K} f'' - \frac{1}{(r + K)^2} f' \right) - \frac{K}{r + K} f'^2 + \frac{K}{r + K} f f''$$

$$+ \frac{K}{(r + K)^2} f f' - \Omega \left(f' + \frac{r}{2} f'' \right) \quad (5.8)$$

$$\frac{1}{Pr} \frac{k_{nf}}{k_f} \frac{(\rho C_p)_f}{(\rho C_p)_{nf}} \left(\theta'' + \frac{1}{r + K} \theta' \right) + \frac{K}{r + K} f \theta' - \Omega \frac{r}{2} \theta' = 0 \quad (5.9)$$

where $K = R \sqrt{a/[v_f(1 - c\bar{t})]}$ is the unsteady curvature parameter. Mukhopadhyay and Andersson [82] assumed R in terms of characteristic radius of curved surface i.e. $R = R_0 \sqrt{1 - c\bar{t}}$, where R_0 is the characteristic radius of the curvature sheet. Thus, $K = R \sqrt{a/v_f}$ is the constant dimensionless curvature parameter and $\Omega = c/a$, $Pr = v_f/\alpha_f$, $\beta = b/a$ are the unsteadiness parameter, Prandtl number and stretching/shrinking parameter, respectively, with $\beta < 0$ for shrinking and $\beta > 0$ indicate stretching. In this chapter, we assume only decelerating

shrinking sheet with $\Omega \leq 0$ and $\beta < 0$. Also, the constants relating to the properties of the nanofluids are given in **Table 1.1-1.2**.

Simultaneously solving Eqs. 5.7-5.8 to eliminate the pressure term

$$f^{iv} + \frac{2}{r+K}f''' - \frac{1}{(r+K)^2}f'' - \frac{1}{(r+K)^3}f' + \frac{v_f}{v_{nf}} \left[\frac{K}{r+K}(ff''' - f'f'') + \frac{K}{(r+K)^2}(ff'' - f'^2) - \frac{K}{(r+K)^3}ff' - \frac{\Omega}{r+K}\left(f' + \frac{r}{2}f''\right) - \frac{\Omega}{2}(3f'' + rf''') \right] = 0 \quad (5.10)$$

$$\frac{1}{Pr} \frac{k_{nf}}{k_f} \frac{(\rho C_p)_f}{(\rho C_p)_{nf}} \left(\theta'' + \frac{1}{r+K}\theta' \right) + \frac{K}{r+K}f\theta' - \Omega \frac{r}{2}\theta' = 0 \quad (5.11)$$

and corresponding boundary constraints are

$$\begin{aligned} f(0) = S, \quad f'(0) = \beta, \quad \theta(0) = 1 \\ f'(r) = 1, \quad f''(r) = 0, \quad \theta(r) = 0 \text{ as } r \rightarrow \infty \end{aligned} \quad (5.12)$$

Eq. (5.8) can be used to calculate the pressure

$$\begin{aligned} p = \left(\frac{\rho_f}{\rho_{nf}} \frac{2K}{r+K} \right)^{-1} \left[\frac{v_{nf}}{v_f} \left(f''' + \frac{1}{r+K}f'' - \frac{1}{(r+K)^2}f' \right) - \frac{K}{r+K}f'^2 \right. \\ \left. + \frac{K}{r+K}ff'' + \frac{K}{(r+K)^2}ff' - \Omega \left(f' + \frac{r}{2}f'' \right) \right] \end{aligned} \quad (5.13)$$

In flow along the surface the important parameters to determine the flow and heat transfer behavior are the skin friction coefficient C_f and the local Nusselt's number Nu_L . The shear stress at the curved surface is given by τ_w and heat flux through curved surface is denoted by q_w and are defined below

$$C_{fr} = \frac{\tau_w}{\frac{1}{2}\rho_f \bar{u}_e^2(\bar{S})}, \quad Nu_L = \frac{\bar{S}q_w}{k_f(T_w - T_\infty)} \quad (5.14)$$

$$\tau_w = \mu_{nf} \left(\frac{\partial \bar{u}}{\partial \bar{r}} - \frac{\bar{u}}{\bar{r} + R} \right) \Big|_{\bar{r}=0}, \quad q_w = -k_{nf} \frac{\partial T}{\partial \bar{r}} \Big|_{\bar{r}=0} \quad (5.15)$$

Using transformation in Eqs. (5.6), (5.14) and (5.15) takes the following form

$$C_f = \frac{\mu_{nf}}{\mu_f} \left(f''(0) - \frac{\beta}{K} \right), \quad Nu = -\frac{k_{nf}}{k_f} \theta'(0) \quad (5.16)$$

where $C_f = (1 - c \bar{t})^{3/2} (Re_{\bar{s}})^{1/2} C_{fr}$, and $Nu = (1 - c \bar{t})^{1/2} (Re_{\bar{s}})^{-1/2} Nu_L$ are the reduced skin friction coefficient and reduced local Nusselt number. $Re_{\bar{s}} = \bar{u}_e(\bar{s}) \bar{s} / \nu_f$ is the localized Reynolds number.

If the curvature parameter $K \rightarrow \infty$ & $\Omega = 0$, the case of plane surface flow is obtained, and the governing equations takes the following form

$$\left. \begin{aligned} \frac{\mu_{nf}}{\mu_f} \frac{\rho_f}{\rho_{nf}} f''' - f'^2 + ff'' + 1 &= 0 \\ \frac{1}{Pr} \frac{k_{nf}}{k_f} \frac{(\rho C_p)_f}{(\rho C_p)_{nf}} \theta'' + f\theta' &= 0 \end{aligned} \right\} \quad (5.17)$$

$$\left. \begin{aligned} f(0) = S, \quad f'(0) = \beta, \quad \theta(0) = 1 \\ f'(\eta) = 1, \quad \theta(\eta) = 0 \text{ as } r \rightarrow \infty \end{aligned} \right\} \quad (5.18)$$

5.3 Stability analysis

The Weidman et al. [23] and Roşca & Pop [82] showed the possible existence of multiple solutions. Stability analysis needs to be carried out to determine which one of them are stable and for what range of parameters. A dimensionless time variable τ is introduced to model the problem for stability analysis. Non-dimensional parameters in terms of τ are given below

$$\left. \begin{aligned} \bar{u} &= \frac{\bar{u}_e}{1 - c \bar{t}} f'(r, \tau), \quad \bar{v} = -\frac{R}{\bar{r} + R} \sqrt{\frac{v_f \bar{u}_e}{(1 - c \bar{t}) \bar{s}}} f(r, \tau), \\ r &= \sqrt{\frac{\bar{u}_e}{v_f (1 - c \bar{t}) \bar{s}}} \bar{r}, \quad c < 0 \\ \bar{p} &= \frac{\rho_f \bar{u}_e^2}{(1 - c \bar{t})^2} p(r, \tau), \quad \theta(r, \tau) = \frac{T - T_\infty}{T_w - T_\infty}, \quad \tau = c \bar{t} \end{aligned} \right\} \quad (5.19)$$

so that Eqs. (5.3,5.5) can be written as

$$\begin{aligned} \frac{\partial^4 f}{\partial r^4} + \frac{2}{r + K} \frac{\partial^3 f}{\partial r^3} - \frac{1}{(r + K)^2} \frac{\partial^2 f}{\partial r^2} - \frac{1}{(r + K)^3} \frac{\partial f}{\partial r} \\ + \frac{v_f}{v_{nf}} \left[\frac{K}{r + K} \left(f \frac{\partial^3 f}{\partial r^3} - \frac{\partial f}{\partial r} \frac{\partial^2 f}{\partial r^2} \right) \right. \\ + \frac{K}{(r + K)^2} \left(f \frac{\partial^2 f}{\partial r^2} - \left(\frac{\partial f}{\partial r} \right)^2 \right) - \frac{K}{(r + K)^3} f \frac{\partial f}{\partial r} \\ - \frac{\Omega}{r + K} \left(\frac{\partial f}{\partial r} + \frac{r}{2} \frac{\partial^2 f}{\partial r^2} \right) - \frac{\Omega}{2} \left(3 \frac{\partial^2 f}{\partial r^2} + r \frac{\partial^3 f}{\partial r^3} \right) \\ \left. - \frac{(1 - c \bar{t})}{r + K} \frac{\partial^2 f}{\partial r \partial \tau} - (1 - c \bar{t}) \frac{\partial^3 f}{\partial r^2 \partial \tau} \right] = 0 \end{aligned} \quad (5.20)$$

$$\begin{aligned} \frac{1}{Pr} \frac{k_{nf}}{k_f} \frac{(\rho C_p)_f}{(\rho C_p)_{nf}} \left(\frac{\partial^2 \theta}{\partial r^2} + \frac{1}{r + K} \frac{\partial \theta}{\partial r} \right) + \frac{K}{r + K} f \frac{\partial \theta}{\partial r} - \Omega \frac{r}{2} \frac{\partial \theta}{\partial r} \\ - (1 - c \bar{t}) \frac{\partial \theta}{\partial \tau} = 0 \end{aligned} \quad (5.21)$$

$$f(0, \tau) = S, \quad \frac{\partial f(0, \tau)}{\partial r} = \beta, \quad \theta(0, \tau) = 1 \quad (5.22)$$

$$\frac{\partial f(r, \tau)}{\partial r} = 1, \quad \frac{\partial^2 f(r, \tau)}{\partial r^2} = 0, \quad \theta(r, \tau) = 0 \text{ as } r \rightarrow \infty$$

In order to examine the stability of the solution the steady flow solutions are $f(r) = f_0(r)$ and $\theta(r) = \theta_0(r)$ satisfying the boundary-value problem (5.10-5.12), the complete solution can be written as

$$f(r, \tau) = f_0(r) + e^{-\alpha \tau} F(r, \tau) \quad (5.23)$$

$$\theta(r, \tau) = \theta_0(r) + e^{-\alpha \tau} \theta_1(r, \tau) \quad (5.24)$$

where α is an unknown eigenvalue parameter. the unsteady part of solution $F(r, \tau)$ and $\theta_1(r, \tau)$ are relatively small compared to $f_0(r)$ and $\theta_0(r)$. using Eqs. (5.23-5.24) into Eqs. (5.20-5.22), the linearized form of the equations is obtained as follows

$$\begin{aligned}
& \frac{\partial^4 F}{\partial r^4} + \frac{2}{r+K} \frac{\partial^3 F}{\partial r^3} - \frac{1}{(r+K)^2} \frac{\partial^2 F}{\partial r^2} - \frac{1}{(r+K)^3} \frac{\partial F}{\partial r} \\
& + \frac{v_f}{v_{nf}} \left[\frac{K}{r+K} \left(f_0 \frac{\partial^3 F}{\partial r^3} - f_0' \frac{\partial^2 F}{\partial r^2} - f_0'' \frac{\partial F}{\partial r} + f_0''' F \right) \right. \\
& + \frac{K}{(r+K)^2} \left(f_0 \frac{\partial^2 F}{\partial r^2} - 2f_0' \frac{\partial F}{\partial r} + f_0'' F \right) \\
& - \frac{K}{(r+K)^3} \left(f_0 \frac{\partial F}{\partial r} + f_0' F \right) - \frac{\Omega}{r+K} \left(\frac{\partial F}{\partial r} + \frac{r}{2} \frac{\partial^2 F}{\partial r^2} \right) \\
& - \frac{\Omega}{2} \left(3 \frac{\partial^2 F}{\partial r^2} + r \frac{\partial^3 F}{\partial r^3} \right) + \frac{(1-c\bar{t})}{\eta+K} \left(\alpha \frac{\partial F}{\partial r} - \frac{\partial^2 F}{\partial r \partial \tau} \right) \\
& \left. + (1-c\bar{t}) \left(\alpha \frac{\partial^2 F}{\partial r^2} - \frac{\partial^3 F}{\partial r^2 \partial \tau} \right) \right] = 0
\end{aligned} \tag{5.25}$$

$$\begin{aligned}
& \frac{1}{Pr} \frac{k_{nf}}{k_f} \frac{(\rho C_p)_f}{(\rho C_p)_{nf}} \left(\frac{\partial^2 \theta_1}{\partial r^2} + \frac{1}{r+K} \frac{\partial \theta_1}{\partial r} \right) + \frac{K}{r+K} \left(f_0 \frac{\partial \theta_1}{\partial r} + F \theta_0' \right) \\
& - \Omega \frac{r}{2} \frac{\partial \theta_1}{\partial r} + (1-c\bar{t}) \left(\alpha \theta_1 - \frac{\partial \theta_1}{\partial \tau} \right) = 0
\end{aligned} \tag{5.26}$$

$$F(0, \tau) = 0, \quad \frac{\partial F(0, \tau)}{\partial \eta} = 0, \quad \theta_1(0, \tau) = 1 \tag{5.27}$$

$$\frac{\partial F(r, \tau)}{\partial r} = 0, \quad \frac{\partial^2 F(r, \tau)}{\partial r^2} = 0, \quad \theta_1(r, \tau) = 0 \text{ as } r \rightarrow \infty$$

By putting $\tau = 0$ the steady state f_0 and θ_0 are achieved, $F = F_0(r)$ and $\theta_1 = \Theta(r)$ determines the growth or decay of the solution for examining the stability of solution (5.23-5.24).

$$\begin{aligned}
F_0^{iv} + \frac{2}{r+K} F_0''' - \frac{1}{(r+K)^2} F_0'' - \frac{1}{(r+K)^3} F_0' \\
+ \frac{v_f}{v_{nf}} \left[\frac{K}{r+K} (f_0 F_0''' - f_0' F_0'' - f_0'' F_0' + f_0''' F_0) \right. \\
+ \frac{K}{(r+K)^2} (f_0 F_0'' - 2f_0' F_0' + f_0'' F_0) \\
- \frac{K}{(r+K)^3} (f_0 F_0' + f_0' F_0) - \frac{\Omega}{r+K} \left(F_0' + \frac{r}{2} F_0'' \right) \\
\left. - \frac{\Omega}{2} (3F_0'' + rF_0''') + \frac{\alpha}{r+K} F_0' + \alpha F_0'' \right] = 0
\end{aligned} \tag{5.28}$$

$$\begin{aligned}
\frac{1}{Pr} \frac{k_{nf}}{k_f} \frac{(\rho C_p)_f}{(\rho C_p)_{nf}} \left(\Theta'' + \frac{1}{r+K} \Theta' \right) + \frac{K}{r+K} (f_0 \Theta' + F_0 \theta_0') - \Omega \frac{r}{2} \Theta' \\
+ \alpha \Theta = 0
\end{aligned} \tag{5.29}$$

$$\begin{aligned}
F_0(0) = 0, \quad F_0'(0) = 0, \quad \Theta(0) = 1 \\
F_0''(r) = 0, \quad F_0'''(r) = 0, \quad \Theta(r) = 0 \text{ as } r \rightarrow \infty
\end{aligned} \tag{5.30}$$

It should be stated that for specific values of S, K, Ω and β , the stability of the steady solution $f_0(r)$ and $\theta_0(r)$ is analyzed by using the smallest of the eigenvalues α . According to Roşca [83], the range of possible eigenvalues can be obtained by relaxing the condition on $F_0(r)$ to $F_0''(r) = 0$ as $r \rightarrow \infty$ and an additional condition $F_0'''(0) = 1$ for solving Eq. (5.28). Infinite number of eigenvalues $\alpha_1 < \alpha_2 < \dots < \alpha_n < \dots$ are obtained when satisfying the boundary condition $F_0''(r) = 0$ as $r \rightarrow \infty$.

It is found that for shrinking curved surface case $\beta < 0$, offers dual solutions when $\alpha_1 > 0$ and $\tau \rightarrow \infty$ (steady-state solution). In this case the upper solution branch is found to be stable and physically possible. However, $\alpha_1 < 0$ causes disturbance in the solution and the lower branch of solution shows instability as $\tau \rightarrow \infty$. This solution is not found to be stable and hence not possible in the current flow situation.

5.4 Results and discussion

The system of governing equations for the nanofluid flow over a curved stretching/shrinking surface have been solved by implementing bvp4c package available in MATLAB for a range of parameter values involved in the mathematical equations. This package is based on the finite difference scheme by implementing three-stage Lobatto IIIa

scheme having fourth-order accuracy. The error control is based on the residual error appearing during continuous solution. The tolerance level is set to the order of 10^{-7} . A good initial guess is important to start the process because of the existence of dual solution. The guess is chosen in such a way that it should satisfy the boundary constraints given in Eq. (5.12) and show asymptotically convergent behavior. Any reasonable initial guess can be taken for the upper solution branch because the scheme is ultimately producing the convergent solution. However, any guess is not able to produce the convergent solution for the case of $\beta < 0$. In order to avoid this problem a suitable set of parameter values are chosen by trial approach to choose suitable guess for obtaining the second solution. This solution is taken as an initial guess to produce solution for different variations in parameter values. The suitable values of boundary layer region are taken to make sure that the infinity condition is satisfied at faraway from surface. Here $r = r_\infty = 20$ to produce the upper solution branch and $r = r_\infty$ is taken to be in the range of 40–80 to produce lower solution branch. The solution is verified against all the boundary constraints and tolerance level of 10^{-7} . The validation of code is done by comparing the results for the reduced case by Nazar et al. [84] in **Table 5.2**, which shows an excellent agreement.

The effects of the important parameters β, φ, S and Ω are presented in the form of graphs against the dimensionless velocity, shear stress profiles and temperature profiles see **Figs. 5.2–5.5**. It can be clearly seen that for the case of lower branch solution the boundary layer thickness is larger as compared to the one for upper branch solution. It is also observed that the wall shear stress shows increasing behavior against the increasing values of S when upper branch solution is considered. However, a different behavior is observed for $\beta (< 0)$ (**Fig. 5.2(a)**). (**Fig. 5.2(b), 5.3(b), 5.4(b)**) show the behavior for the lower branch solution. Finally, **Figs. 5.5** display the temperature profiles for decelerating shrinking sheet with $\Omega \leq 0$ and mass transfer parameter S . The thermal boundary layer has decreasing trend against both the parameters. All the conditions at the surface are satisfied as well as the asymptotically converging behavior is observed for far field boundary condition. The terms upper (first) and lower (second) branch solutions is being taken from the figures (5.7-5.13) It was expected that the upper solution branch will be stable as compared with the lower solution branch. From **Figs 5.6-5.8** It is seen that there exists more than one solution for different range of β values.

Two solutions exist for $\beta > \beta_c$, unique solution for $\beta = \beta_c$ and no solution exists for $\beta < \beta_c$, the subscript c represent the critical value. The critical point of β changes with the variation in $|\Omega|$, φ and S . **Fig. 5.9** shows the variation of C_f with respect to Ω for several values of S when $K = 200$, $\beta = -0.5$, $\varphi = 0.2$. It can be observed from this Fig that there are two solutions when $\Omega > \Omega_c$, one solution when $\Omega = \Omega_c$ and no solutions when $\Omega < \Omega_c$. Its critical point value also increases with increase in S . The suction parameter S plays an important role in delaying the separation near the surface. The variation of C_f with respect to K for several values of β is shown in **Fig. 5.10**. It is observed from this figure that dual solutions will exist for different ranges of curvature parameter as well. Once again two solutions appear when $K > K_c$, one solution for $K = K_c$ and no solutions for $K < K_c$. The critical point value of curvature also changes with change in $|\beta|$. **Figs 5.11-5.13** show the dual solution and critical value of Nusselt number for range of parameter values involved in equation. It is found that the consideration of upper branch solution results in higher value of Nusselt number as compared to that of produced by using lower branch of solution. Further it is also noticed that the suction parameter is causing the wideness in the range of Nusselt number values for which the solution exists. At the end of graphical section streamlines are plotted to analyze the flow pattern if the upper or lower branch solutions are considered. The streamline pattern suggests for the upper branch (stable) solution a normal stagnation point flow was occurring (**Fig. 5.14a (1-3)**). While streamlines suggest the situation of reverse flow when the lower branch solution is considered (**Fig. 5.14b (1-3)**). The stream lines are clearly showing that flow region is divided into two sub-regions one where flow is like a normal stagnation point flow and other showing the reverse flow region. The isotherms for the nanofluid flow over curved surface are shown in **Fig.5.15** for a range of different parameters. Finally, a tabular form of eigen values (for selected values of S and β) are given in **Table (5.2-5.3)** for which stability analysis is performed. It is noticed that for the case of upper branch solution all the smallest eigen values are positive while they are negative for the lower branch solution. This concludes that the upper branch solution is more stable compared to the lower branch solution.

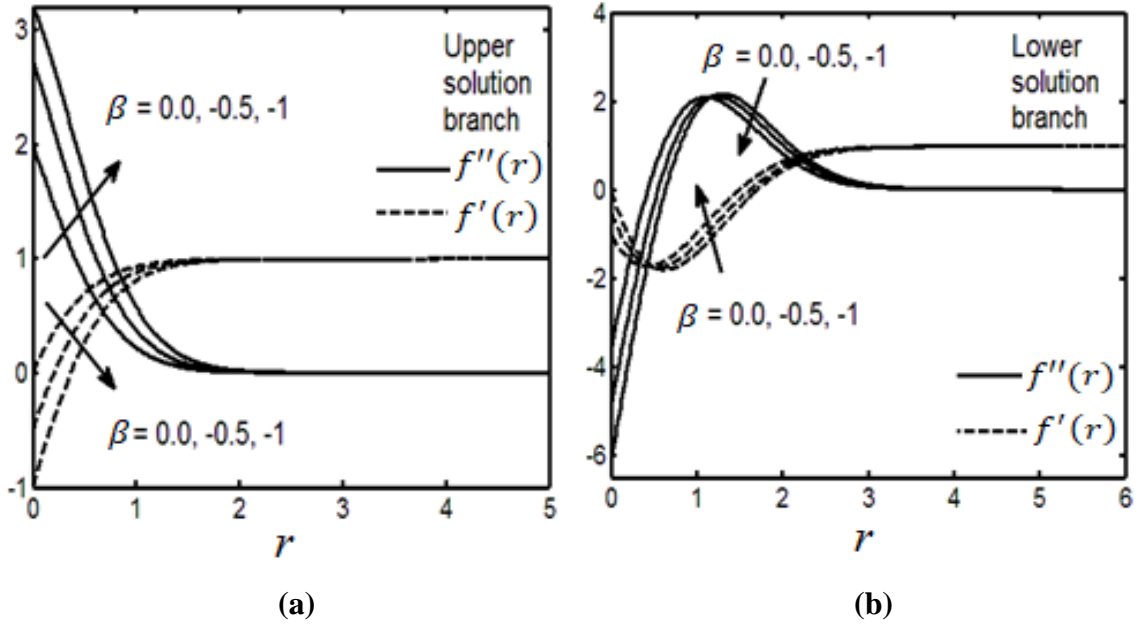


Fig. 5. 2. Plot showing the behaviour of $f'(r)$ & $f''(r)$ with respect to β .

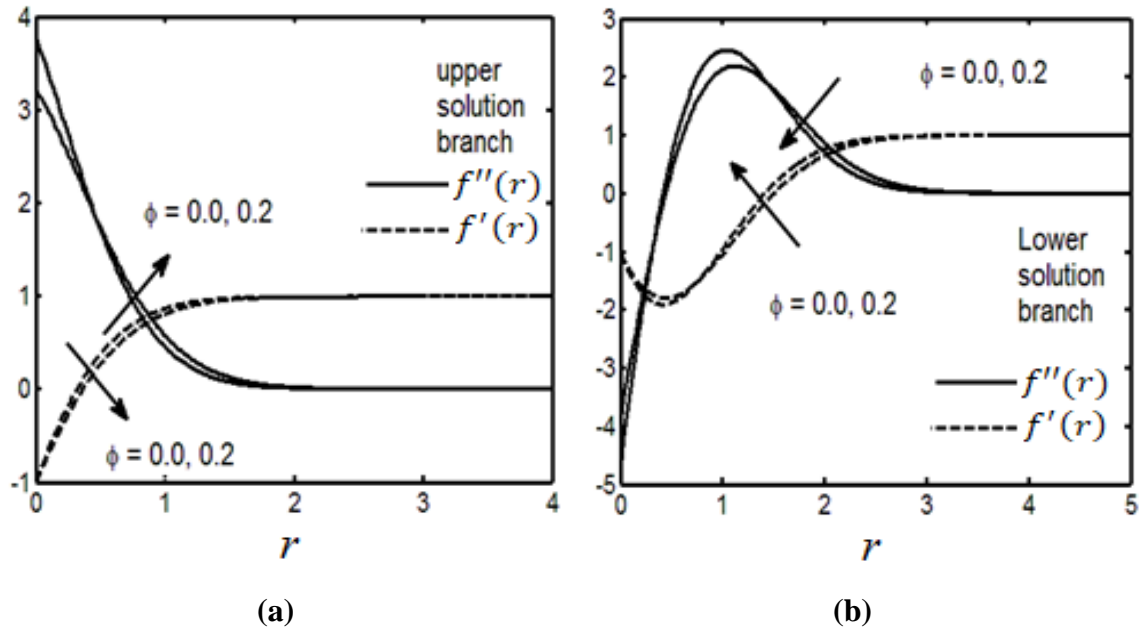


Fig. 5. 3. Plot showing the behaviour of $f'(r)$ & $f''(r)$ with respect to ϕ .

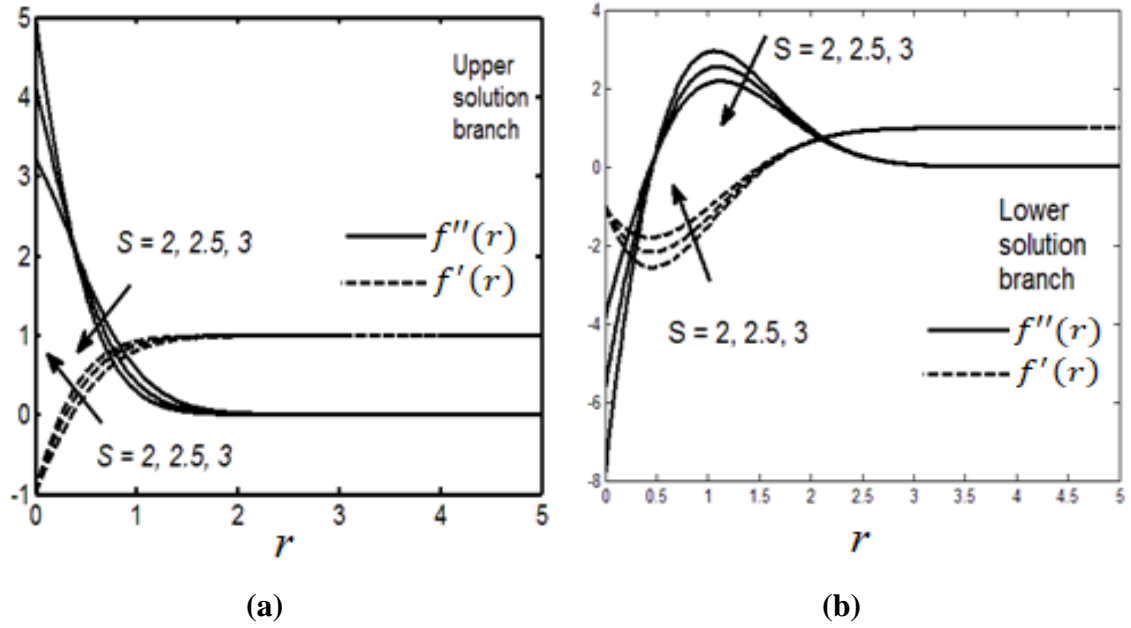


Fig. 5. 4. Plot showing the behaviour of $f'(r)$ & $f''(r)$ with respect to S .

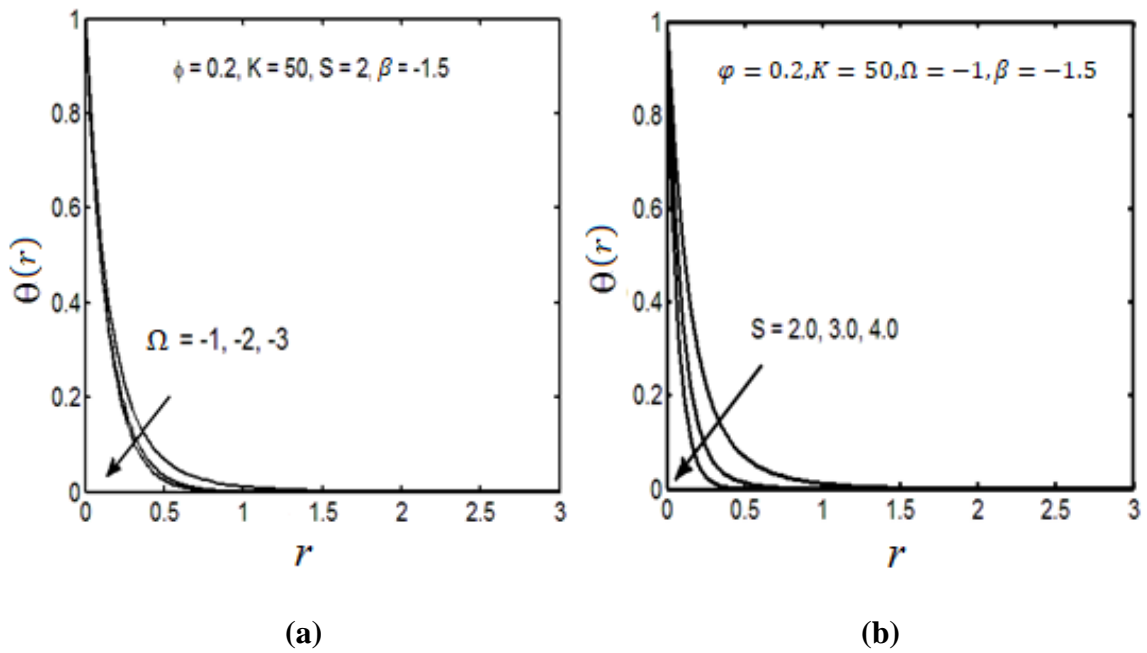


Fig. 5. 5. Plot showing the behaviour of $\theta(r)$ with respect to Ω & S .

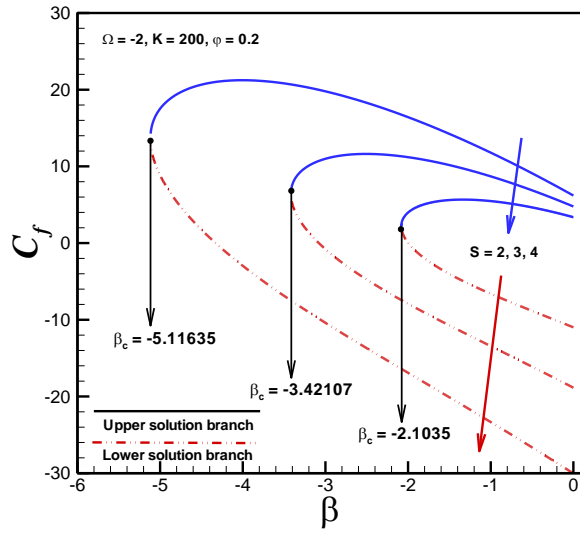


Fig. 5. 6. Variation of C_f with respect to β for several values of S .

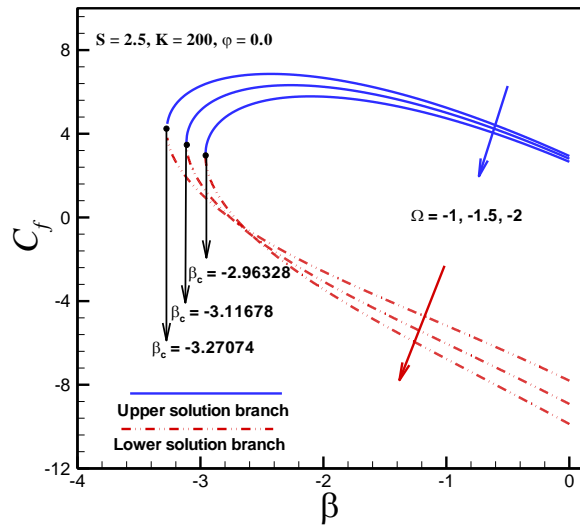


Fig. 5. 7. Variation of C_f with respect to β for several values of Ω .

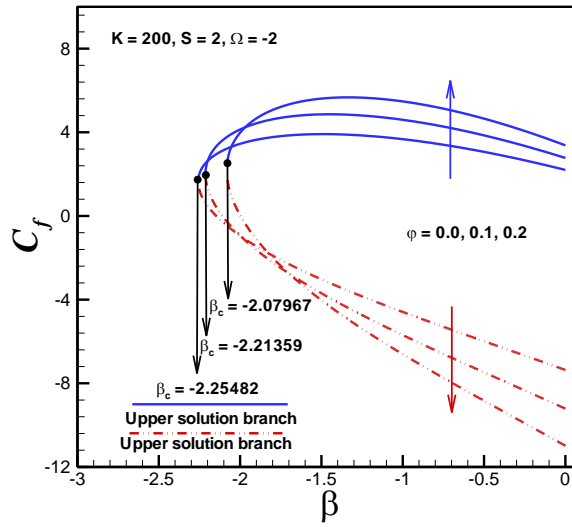


Fig. 5. 8. Variation of C_f with respect to β for several values of φ .

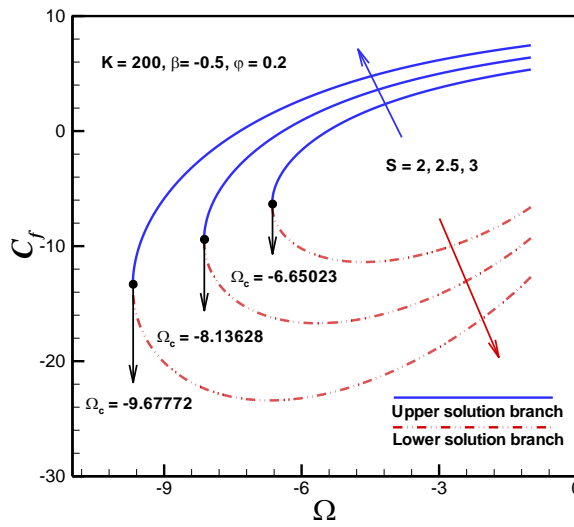


Fig. 5. 9. Variation of C_f with respect to Ω for several values of S .

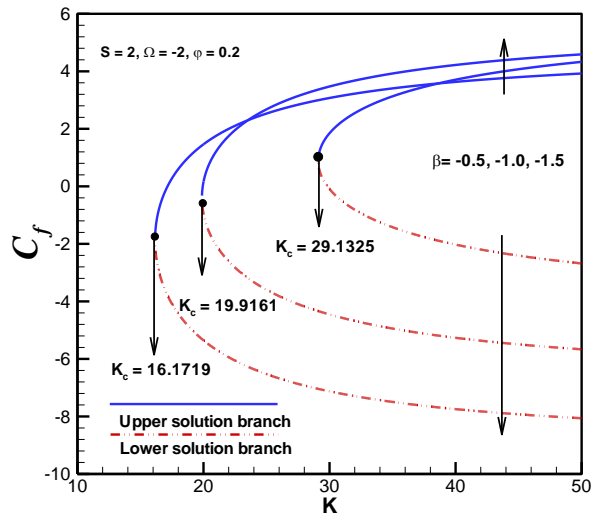


Fig. 5. 10. Variation of C_f with respect to K for several values of β .

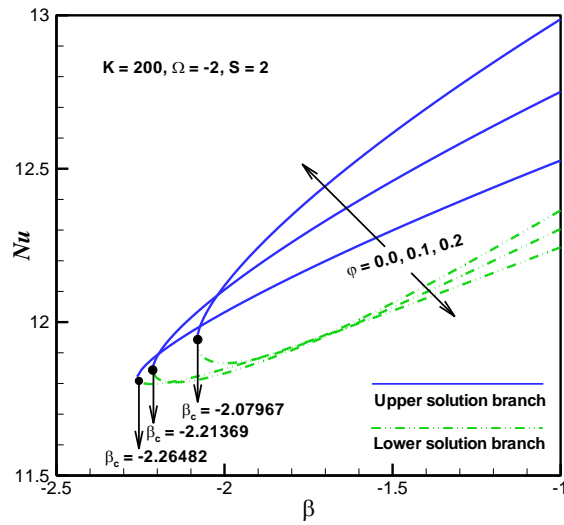


Fig. 5. 11. Variation of Nu with respect to β for several values of ϕ .

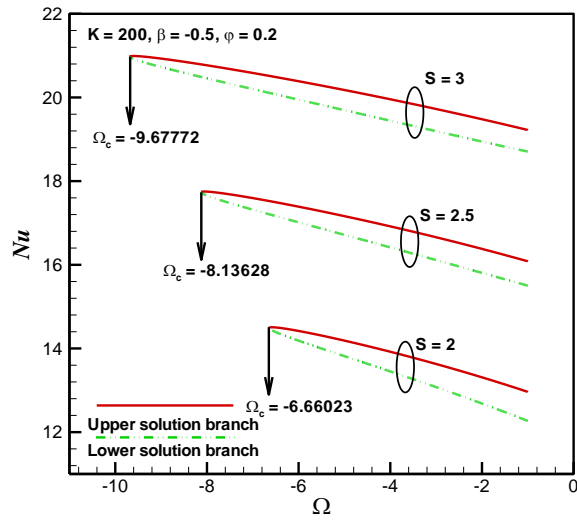


Fig. 5.12. Variation of Nu with respect to Ω for several values of S .

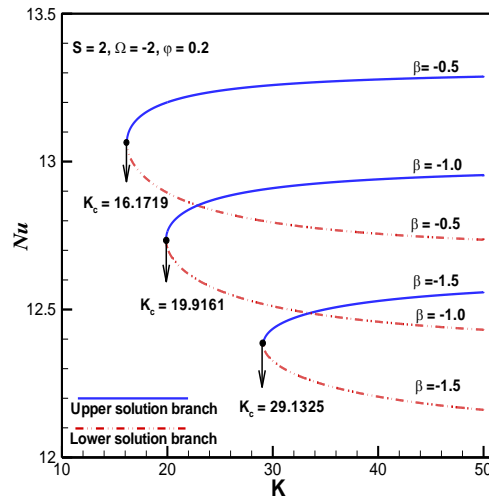


Fig. 5.13. Variation of Nu with respect to K for several values of β .

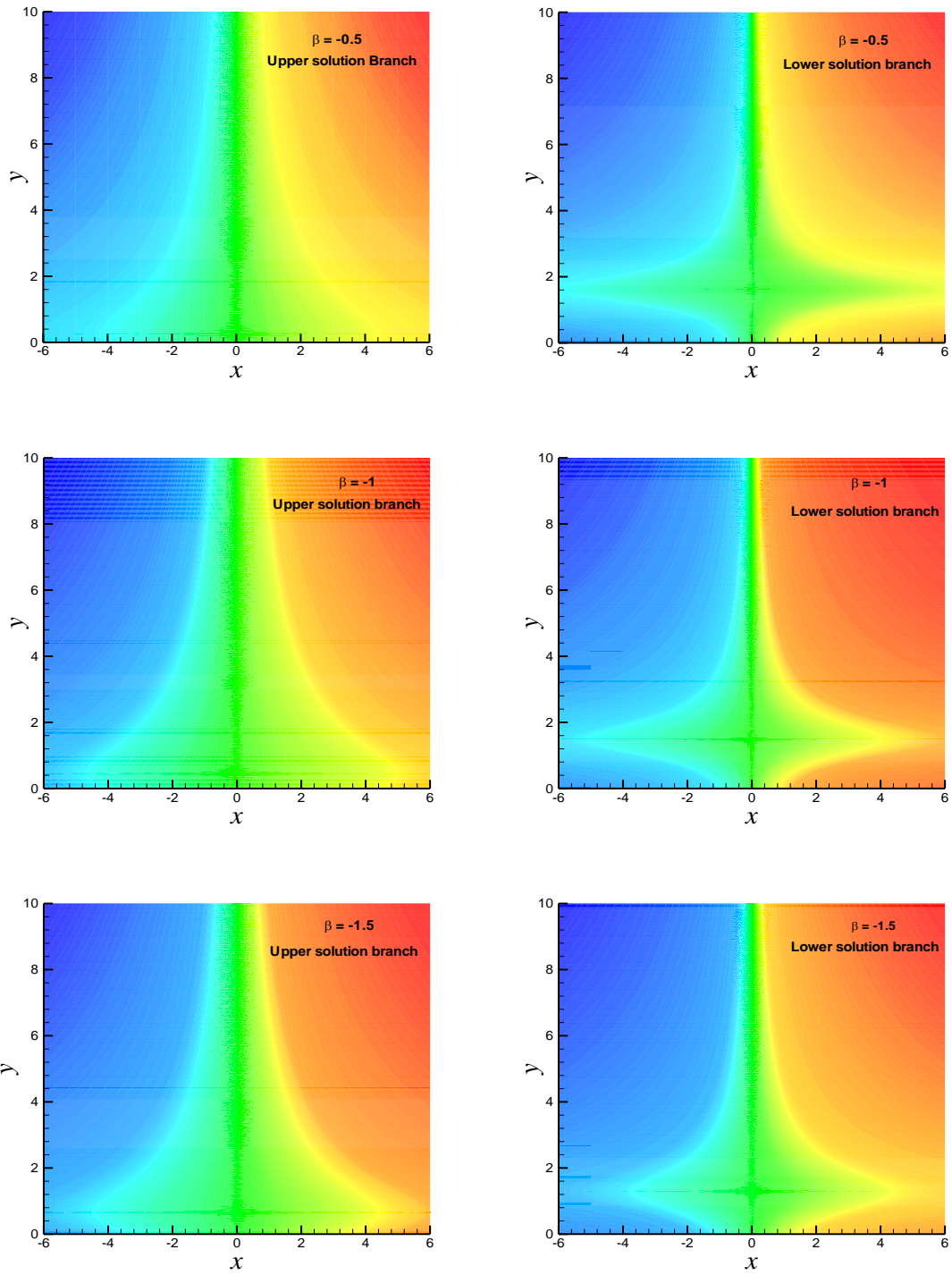
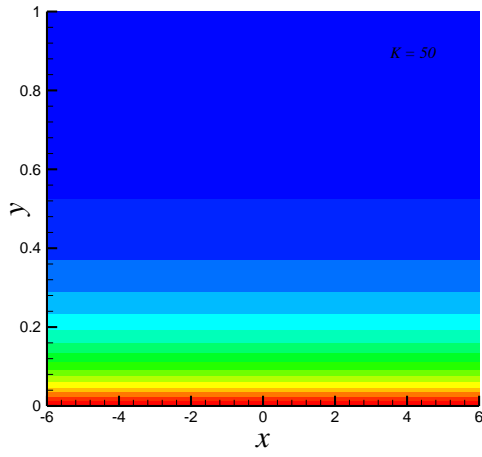
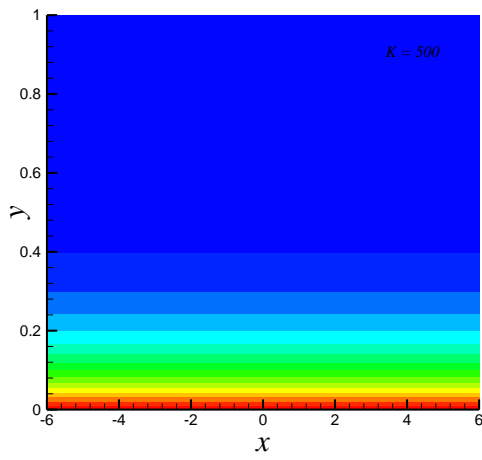


Fig. 5. 14. Stream lines pateren for several values of β when $S = 2, K = 50, \varphi = 0.2, \Omega = -2$.



(a)



(b)

Fig. 5. 15. Isotherms for several values of K when $S = 2, \beta = -1.5, \varphi = 0.2, \Omega = -2, Pr = 6.2$.

Table. 5. 1. Numerical Values of C_f with $K = \infty, S = 0$ and $\varphi = 0$ (regular fluid), Results in parenthesis () are the second (lower branch) solutions.

β	C_f	
	Present	Nazar et al [84]
-0.2	1.37389	-
-0.25	1.40224	1.40224
-0.3	1.42758	-
-0.35	1.44975	-
-0.4	1.46861	-
-0.45	1.48399	-
-0.5	1.49567	1.49567
-0.55	1.50344	-
-0.6	1.50703	-
-0.7	1.50036	-
-0.75	1.4893	1.48930
-0.8	1.47239	-
-0.9	1.41808	-
-0.95	1.3786	-
-1	1.32882	1.32882
-1.05	1.26623	-
-1.1	1.18668 (0.049229)	1.18668 (0.04920)
-1.15	1.08223 (0.116702)	1.08223 (0.116702)
-1.2	0.932477 (0.23365)	0.93247 (0.23363)

Table. 5. 2. Comparison of eigenvalues α for different β when $S = 0, \varphi = 0.0, K = \infty, \Omega = 0$.

β	Upper branch solution		Lower branch solution	
	[84]	Present	[84]	Present
-1	1.3690	1.369044	-	-
-1.1	1.0463	1.046348	-0.8437	-0.843697
-1.2	0.5780	0.577960	-0.5173	-0.512109
-1.24	0.2121	0.212053	-0.2036	-0.203639
-1.245	0.1030	0.102975	-0.1010	-0.100958
-1.246	0.0622	0.062157	-0.0614	-0.061418

Table. 5. 3. Smallest eigenvalues α at selected values of S and β when $\varphi = 0.2, K = 200, \Omega = -2$.

S	β	Upper solution branch	Lower solution branch
1.5	0.0	1.492433	-
	-0.1	1.181180	-0.180752
	-0.2	1.037085	-0.114800
	-0.3	0.947922	-0.046200
2.0	0.0	2.171598	-0.481961
	-0.1	1.514339	-0.46323
	-0.2	1.313345	-0.436906
	-0.3	1.198322	-0.404290

5.5 Conclusion

A theoretical study of unsteady viscous nanofluid flow over a curved shrinking surface with mass suction has been analyzed. Alumina (Al_2O_3) and Ethylene glycol are considered as nanoparticles and base fluids, respectively. The corresponding flow equations are reduced to a system of nonlinear coupled ordinary differential equations which contain the flow parameters, curvature parameter, mass suction parameter, unsteadiness parameter, nanoparticles volume fraction, shrinking parameters and Prandtl number Pr . The reduced system of ODE's is solved numerically by using bvp4c scheme in MATLAB. The numerical results are obtained for the physical parameters the reduced skin friction and the reduced local Nusselt number against different values of flow parameters. From this study we get the following remarks:

1. Dual solution exists for shrinking curved surface.
2. The critical values β_c of shrinking parameter (β) depends upon φ, K, Ω and S.
3. The mass suction parameter S decrease the range of shrinking parameter, β , and unsteadiness parameter, Ω , for which solution exist.
4. The range of solution interval for curvature parameter K found compatible with lesser values of shrinking parameter (Ω).
5. The critical point $|\beta_c|$ decrease for nanoparticle volume fraction (φ).
6. The streamline pattern for the upper branch (stable) solutions is similar to normal stagnation point flow.
7. Reversed flow is appearing in the case of the lower branch solutions.
8. The upper branch solutions have positive eigenvalue while all the lower branch solutions have negative eigenvalue.

9. The upper branch solution is physically realizable (stable) while the lower branch is not physically realizable (unstable).

Chapter # 6

Analysis of unsteady non-axisymmetric Homann stagnation point flow of nanofluid and possible existence of multiple solutions

6.1 Introduction

This chapter examines the unsteady 3D non-axisymmetric Homann flow of an electrically conducting nanofluids in the presence of buoyancy forces. We consider the uniform external magnetic field, \mathbf{B}_0 , by neglecting induced magnetic field and examines the three possible directions of \mathbf{B}_0 which coincides with the direction of axes. A similarity solution is derived which involve the dimensionless parameters $\varphi, M, \omega, \gamma$ and λ . We have treated the case for forced convection when $\lambda = 0$ which arise from the singularity $\gamma = \mp 1$. We found that, for large γ and λ , the leading terms of the solutions are independent of M and ω , and the effects of φ in that solutions are negligible. Numerical results are found for illustrative values of all the flow parameters by using bvp4c scheme in MATLAB.

6.2 Problem formulation

Consider the unsteady MHD asymmetric Homan stagnation point flow of a homogeneous, electrically conducting and incompressible inviscid fluid over a flat vertical wall. It is assumed that the external flow is

$$\begin{aligned}\bar{u}(\bar{t}, \bar{x}, \bar{y}) &= \frac{1}{1 - c\bar{t}}(a\bar{x} + b\bar{y}), \quad \bar{v}(\bar{t}, \bar{x}, \bar{y}) = \frac{1}{1 - c\bar{t}}(b\bar{x} + a\bar{y}), \\ \bar{w}(\bar{t}, \bar{z}) &= \frac{-2a\bar{z}}{1 - c\bar{t}}\end{aligned}\tag{6.1}$$

$c > 0$ represent an accelerated flow and $c < 0$ a decelerated flow, and, $\bar{y} - axis$ measured in the gravity direction and $\bar{z} - axis$ measured in the normal direction to the $\bar{x}\bar{y} - plane$.

The horizontal velocities \bar{u} and \bar{v} in system (1) can be written as in matrix form

$$\begin{pmatrix} \bar{u} \\ \bar{v} \end{pmatrix} = \frac{1}{1 - c\bar{t}} \begin{pmatrix} a & b \\ b & a \end{pmatrix} \begin{pmatrix} \bar{x} \\ \bar{y} \end{pmatrix}\tag{6.2}$$

To obtain the principal axis of the system, we diagonalized the coefficient matrix in (6.2) by using the results from linear algebra. The velocity components (\bar{u}', \bar{v}') in the direction of principal axes (\bar{x}', \bar{y}') is then given by

$$\begin{pmatrix} \bar{u}' \\ \bar{v}' \end{pmatrix} = \frac{1}{1 - c\bar{t}} \begin{pmatrix} \lambda_1 & 0 \\ 0 & \lambda_2 \end{pmatrix} \begin{pmatrix} \bar{x}' \\ \bar{y}' \end{pmatrix}.\tag{6.3}$$

Rotating the coordinates $(\bar{x}, \bar{y}, \bar{z})$ to the principal axes $(\bar{x}', \bar{y}', \bar{z}')$, we get the outer potential flow

$$\begin{aligned}\bar{u}'(\bar{t}, \bar{x}', \bar{y}') &= \frac{1}{1 - c\bar{t}}(a + b)\bar{x}', \quad \bar{v}'(\bar{t}, \bar{x}', \bar{y}') = \frac{1}{1 - c\bar{t}}(a - b)\bar{y}', \\ \bar{w}(\bar{t}, \bar{z}') &= \frac{-2a\bar{z}'}{1 - c\bar{t}}\end{aligned}\tag{6.4}$$

It is difficult to find the asymptotic behavior of solutions by considering the outer flow (6.1). For this purpose, we preferred to formulate the problem along the principal axes, without loss of generality, and after dropping the prime notation in (6.4), we arrive at

$$\bar{u}(\bar{t}, \bar{x}, \bar{y}) = \frac{a}{1 - c\bar{t}}(1 + \gamma)\bar{x}, \quad \bar{v}(\bar{t}, \bar{x}, \bar{y}) = \frac{a}{1 - c\bar{t}}(1 - \gamma)\bar{y}, \quad \bar{w}(\bar{t}, \bar{z}) = \frac{-2a\bar{z}}{1 - c\bar{t}} \quad (5)$$

where $\gamma = b/a$ represent the ratio of shear-to-strain rate

6.2.1 The flow of an inviscid fluid

The equations overseeing such a flow within the existence of the gravity forces are:

$$\begin{aligned} \rho_0 \left(\frac{\partial \mathbf{V}}{\partial \bar{t}} + (\mathbf{V} \cdot \nabla) \mathbf{V} \right) &= -\nabla \bar{p} + \frac{1}{\mu_e} (\nabla \times \mathbf{B}) \times \mathbf{B} + \rho_0 \mathbf{g}_0 \\ \frac{1}{\mu_e} (\nabla \times \mathbf{B}) &= \sigma_e (\mathbf{E} + \mathbf{V} \times \mathbf{B}) \\ \nabla \cdot \mathbf{V} = \mathbf{0}, \quad \nabla \times \mathbf{E} = \mathbf{0}, \quad \nabla \cdot \mathbf{E} = \mathbf{0}, \quad \nabla \cdot \mathbf{B} = \mathbf{0} \end{aligned} \quad (6.6)$$

where \mathbf{g}_0 is the gravity acceleration.

We suppose that a uniform external magnetic field \mathbf{B} is impressed and that the electric field is absent. Further we assume that the magnetic Reynolds number is very small, so that the induced magnetic field is negligible in comparison with the imposed field. Then

$$(\nabla \times \mathbf{B}) \times \mathbf{B} \simeq \sigma_e \mu_e (\mathbf{V} \times \mathbf{B}_0) \times \mathbf{B}_0$$

In the results, we will use the modified pressure p^* given by $p^* = \bar{p} + \rho_0 \mathbf{g}_0 \bar{y}$. As in [20] one can prove that the steady three-dimensional stagnation point flow is possible if, and only if, \mathbf{B}_0 is parallel to one of the axes.

If $\mathbf{B}_0 = B_0 \hat{\mathbf{i}}$, we deduce

$$\begin{aligned} p_0 - p^* &= \rho_0 \left(\frac{\partial}{\partial \bar{t}} \int \bar{u} \partial \bar{x} + \frac{v^2}{2} \right) + \rho_0 \frac{\alpha}{2} \frac{a}{(1 - c\bar{t})^2} ((1 - \gamma)\bar{y}^2 - 2\bar{z}^2) + \\ &\quad \sigma_e \frac{1}{2} \frac{a}{1 - c\bar{t}} B_0^2 ((1 - \gamma)\bar{y}^2 - 2\bar{z}^2). \end{aligned} \quad (6.7)$$

If $\mathbf{B}_0 = B_0 \hat{\mathbf{j}}$, we obtain

$$\begin{aligned} p_0 - p^* &= \rho_0 \left(\frac{\partial}{\partial \bar{t}} \int \bar{v} \partial \bar{y} + \frac{v^2}{2} \right) + \rho_0 \frac{\alpha}{2} \frac{a}{(1 - c\bar{t})^2} ((1 + \gamma)\bar{x}^2 - 2\bar{z}^2) + \\ &\quad \sigma_e \frac{\alpha}{2} \frac{a}{1 - c\bar{t}} B_0^2 ((1 + \gamma)\bar{x}^2 - 2\bar{z}^2). \end{aligned} \quad (6.8)$$

If $\mathbf{B}_0 = B_0 \hat{\mathbf{k}}$, we arrive at

$$p_0 - p^* = \rho_0 \left(\frac{\partial}{\partial \bar{t}} \int \bar{w} d\bar{z} + \frac{v^2}{2} \right) + \frac{\alpha}{2} \frac{a}{(1-c\bar{t})^2} \left((1+\gamma)\bar{x}^2 + (1-\gamma)\bar{y}^2 \right) + \sigma_e \frac{1}{2} \frac{a}{1-c\bar{t}} B_0^2 \left((1+\gamma)\bar{x}^2 + (1-\gamma)\bar{y}^2 \right). \quad (6.9)$$

From Eqs. (6.7-6.9), we notice that the modified pressure along the wall $\bar{z} = 0$ takes its maximum value in the stagnation point.

6.2.2 Newtonian nanofluids: analysis of the flow

In order to study the electrically conducting Newtonian nanofluids we neglect the induced magnetic and apply the Boussinesq approximation. Consider that $o\bar{x}\bar{y}$ plane is vertical ($o\bar{y}$ vertical upward), then the flow equations can be written as

$$\left. \begin{aligned} \rho_{nf} \left(\frac{\partial \mathbf{V}}{\partial \bar{t}} + (\mathbf{V} \cdot \nabla) \mathbf{V} \right) &= -\nabla \bar{p} + \mu_{nf} \nabla^2 \mathbf{V} + \sigma_{nf} (\mathbf{V} \times \mathbf{B}_0) \times \mathbf{B}_0 - (\rho\beta)_{nf} (\bar{T} - \bar{T}_0) \mathbf{g}_0 \\ (\rho C_p)_{nf} \left(\frac{\partial \bar{T}}{\partial \bar{t}} + (\mathbf{V} \cdot \nabla) \bar{T} \right) &= k_{nf} \nabla^2 \bar{T} \\ \frac{1}{\mu_e} (\nabla \times \mathbf{B}) &= \sigma_e (\mathbf{E} + \mathbf{V} \times \mathbf{B}) \\ \nabla \cdot \mathbf{V} = \mathbf{0}, \quad \nabla \times \mathbf{E} = \mathbf{0}, \quad \nabla \cdot \mathbf{E} = \mathbf{0}, \quad \nabla \cdot \mathbf{B} = \mathbf{0} \end{aligned} \right\}, \quad (6.10)$$

As for as we concerned, the condition at boundary (wall) for \mathbf{V} and \bar{T} , we propose:

$$\mathbf{V}|_{\bar{z}=0} = \mathbf{0}, \quad \bar{T}|_{\bar{z}=0} = \bar{T}_w(\bar{t}, \bar{y}) = \frac{D\bar{y}}{1-c\bar{t}} + \bar{T}_0. \quad (6.11)$$

where D is constant. If the constant D is negative (positive), then the wall $\bar{z} = 0$ is colder (hotter) than the surroundings at $\bar{y} > 0$, while it is hotter (colder) than the surroundings at $\bar{y} < 0$.

Assume the steady state behavior of solutions

$$\begin{aligned} \bar{u} &= \frac{a}{1-c\bar{t}} (1+\gamma)\bar{x}\bar{f}'(\bar{z}), \quad \bar{v} = \frac{a}{1-c\bar{t}} (1-\gamma)\bar{y}\bar{g}'(\bar{z}), \\ \bar{w} &= \frac{-a}{1-c\bar{t}} [(1+\gamma)\bar{f}(\bar{z}) + (1-\gamma)\bar{g}(\bar{z})], \quad \bar{T} - \bar{T}_0 = \frac{D\bar{y}}{1-c\bar{t}} T(\bar{z}). \end{aligned} \quad (6.12)$$

where $\bar{f}(\bar{z})$, $\bar{g}(\bar{z})$, $T(\bar{z})$ are sufficiently regular unknown and prime represents derivative with respect to \bar{z} .

From Eqs. (6.7-6.9), we found that it is more suitable from a physical point of view by applying the external magnetic field normal to the wall. Therefore, we begin with $\mathbf{B}_0 = B_0 \hat{\mathbf{k}}$ so that Eq. (6.10)₁ become

$$\begin{aligned} \frac{\partial \bar{p}}{\partial \bar{x}} = -\rho_{nf} \left\{ \frac{\alpha a}{(1 - c\bar{t})^2} (1 + \gamma) \bar{x} \bar{f}' \right. \\ + \frac{a^2}{(1 - c\bar{t})^2} (1 + \gamma)^2 \bar{x} (\bar{f}')^2 - v_{nf} \left(\frac{a}{1 - c\bar{t}} (1 + \gamma) \bar{x} \bar{f}''' \right) \\ - \frac{a^2}{(1 - c\bar{t})^2} (1 + \gamma)^2 \bar{x} \bar{f}'' [(1 + \gamma) \bar{f} + (1 - \gamma) \bar{g}] \\ \left. + \frac{\sigma_{nf}}{\rho_{nf}} B_0^2 \frac{a}{1 - c\bar{t}} (1 + \gamma) \bar{x} \bar{f}' \right\} \end{aligned} \quad (6.13)$$

$$\begin{aligned} \frac{\partial \bar{p}}{\partial \bar{y}} = -\rho_{nf} \left\{ \frac{ca}{(1 - c\bar{t})^2} (1 - \gamma) \bar{y} \bar{g}' \right. \\ + \frac{a^2}{(1 - c\bar{t})^2} (1 - \gamma)^2 \bar{y} (\bar{g}')^2 - v_{nf} \left(\frac{a}{1 - c\bar{t}} (1 - \gamma) \bar{y} \bar{g}''' \right) \\ - \frac{a^2}{(1 - c\bar{t})^2} (1 - \gamma)^2 \bar{y} \bar{g}'' [(1 + \gamma) \bar{f} + (1 - \gamma) \bar{g}] \\ \left. + \frac{\sigma_{nf}}{\rho_{nf}} B_0^2 \frac{a}{1 - c\bar{t}} (1 - \gamma) \bar{y} \bar{g}' + \beta_{nf} \frac{D\bar{y}}{1 - c\bar{t}} T \mathbf{g}_0 \right\} \end{aligned} \quad (6.14)$$

$$\begin{aligned} \frac{\partial \bar{p}}{\partial \bar{z}} = -\rho_{nf} \left\{ \frac{-ca}{(1 - c\bar{t})^2} [(1 + \gamma) \bar{f} + (1 - \gamma) \bar{g}] \right. \\ + \frac{a^2}{(1 - c\bar{t})^2} [(1 + \gamma) \bar{f} + (1 - \gamma) \bar{g}] [(1 + \gamma) \bar{f}' \\ \left. + (1 - \gamma) \bar{g}'] + v_{nf} \left(\frac{a}{1 - c\bar{t}} [(1 + \gamma) \bar{f}'' + (1 - \gamma) \bar{g}''] \right) \right\} \end{aligned} \quad (6.15)$$

Further the conditions (11) provides

$$\bar{f}'(0) = 0, \bar{f}(0) = 0, \bar{g}'(0) = 0, \bar{g}(0) = 0, T(0) = 1. \quad (6.16a)$$

Furthermore, as usual, when studying the stagnation point flow for viscous nanofluids, we presume that the free stream flow has the similar behavior as for an inviscid fluid flow at the temperature \bar{T}_0 whose velocity is specified by (6.5). Thus, to solve (6.16a) we add the subsequent conditions

$$\bar{f}'(\bar{z}) = 1, \quad \bar{g}'(\bar{z}) = 1, \quad T(\bar{z}) = 0 \quad \text{as } \bar{z} \rightarrow \infty. \quad (6.16b)$$

To find the pressure field we integrate (6.15) and suppose that, the pressure \bar{p} away from the surface has the similar behavior as for an inviscid fluid (see (6.5)) and same modified pressure as in section (6.2.1). We then obtain the modified pressure field as

$$\begin{aligned} p^* = p_0 - \rho_{nf} & \left\{ \frac{-ca}{(1-c\bar{t})^2} \left[(1+\gamma) \int_0^{\bar{z}} \bar{f} d\bar{z} + (1-\gamma) \int_0^{\bar{z}} \bar{g} d\bar{z} \right] \right. \\ & + \frac{a^2}{2(1-c\bar{t})^2} [(1+\gamma)\bar{f} + (1-\gamma)\bar{g}]^2 + v_{nf} \left(\frac{a}{1-c\bar{t}} [(1+\gamma)\bar{f}' \right. \\ & \left. \left. + (1-\gamma)\bar{g}'] \right) \right. \\ & + \left[\frac{ca}{(1-c\bar{t})^2} (1+\gamma) + \frac{a^2}{(1-c\bar{t})^2} (1+\gamma)^2 \right. \\ & \left. + \frac{\sigma_{nf}}{\rho_{nf}} B_0^2 \frac{a}{1-c\bar{t}} (1+\gamma) \right] \frac{\bar{x}^2}{2} \\ & + \left[\frac{ca}{(1-c\bar{t})^2} (1-\gamma) + \frac{a^2}{(1-c\bar{t})^2} (1-\gamma)^2 \right. \\ & \left. + \frac{\sigma_{nf}}{\rho_{nf}} B_0^2 \frac{a}{1-c\bar{t}} (1-\gamma) \right] \frac{\bar{y}^2}{2} \left. \right\}, \end{aligned} \quad (6.17)$$

where p^* is modified pressure and p_0 is stagnation pressure. In consideration of (6.17) we obtain a system of ordinary differential equations

$$\begin{aligned}
v_{nf} \frac{1 - c\bar{t}}{a} \bar{f}'''' + \bar{f}'' [(1 + \gamma)\bar{f} + (1 - \gamma)\bar{g}] - (1 + \gamma) [(\bar{f}')^2 - 1] \\
- \omega [\bar{f}' - 1] - \frac{\sigma_{nf} \rho_f}{\sigma_f \rho_{nf}} M^2 [\bar{f}' - 1] = 0,
\end{aligned} \tag{6.18}$$

$$\begin{aligned}
v_{nf} \frac{1 - c\bar{t}}{a} \bar{g}'''' + \bar{g}'' [(1 + \gamma)\bar{f} + (1 - \gamma)\bar{g}] - (1 - \gamma) [(\bar{g}')^2 - 1] \\
- \omega [\bar{g}' - 1] - \frac{\sigma_{nf} \rho_f}{\sigma_f \rho_{nf}} M^2 [\bar{g}' - 1] + \frac{\beta_{nf}}{\beta_f} (1 - \gamma) \lambda T = 0,
\end{aligned} \tag{6.19}$$

$$\begin{aligned}
\frac{1}{Pr} \frac{k_{nf}}{k_f} \frac{(\rho C_p)_f}{(\rho C_p)_{nf}} \frac{(1 - c\bar{t})v_f}{a} T'' - \omega T - (1 - \gamma) \bar{g}' T \\
+ [(1 + \gamma)\bar{f} + (1 - \gamma)\bar{g}] T' = 0,
\end{aligned} \tag{6.20}$$

where

$$\begin{aligned}
M^2 = \frac{(1 - c\bar{t})\sigma_f B_0^2}{a\rho_f}, \lambda = \frac{D\beta_f g_0(1 - c\bar{t})}{a^2(1 - \gamma)^2}, \omega = \frac{c}{a}, Pr = \frac{(\rho C_p)_f v_f}{k_f} \\
B_0 = \frac{B_{00}}{\sqrt{(1 - c\bar{t})}}, \quad D = \frac{D_0}{(1 - c\bar{t})}.
\end{aligned}$$

For the current study we assumed a decelerated flow with $\omega \leq 0$. Now it is suitable to write the flow equations in dimensionless form. For this, we use

$$\begin{aligned}
f(z) &= \sqrt{\frac{a}{v_f(1 - c\bar{t})}} \bar{f} \left(\sqrt{\frac{v_f(1 - c\bar{t})}{a}} z \right), \\
g(z) &= \sqrt{\frac{a}{v_f(1 - c\bar{t})}} \bar{g} \left(\sqrt{\frac{v_f(1 - c\bar{t})}{a}} z \right), \\
z &= \sqrt{\frac{a}{v_f(1 - c\bar{t})}} \bar{z}, \quad \theta(z) = T \left(\sqrt{\frac{v_f(1 - c\bar{t})}{a}} z \right).
\end{aligned} \tag{6.21}$$

Thus, Eqs. (6.18-6.20) transformed to

$$\begin{aligned} \frac{v_{nf}}{v_f} f'''' + f''^{[(1+\gamma)f+(1-\gamma)g]} - (1+\gamma)[(f')^2 - 1] - \omega[f' - 1] \\ - \frac{\sigma_{nf}}{\sigma_f} \frac{\rho_f}{\rho_{nf}} M^2 [f' - 1] = 0, \end{aligned} \quad (6.22)$$

$$\begin{aligned} \frac{v_{nf}}{v_f} g'''' + g''^{[(1+\gamma)f+(1-\gamma)g]} - (1-\gamma)[(g')^2 - 1] - \omega[g' - 1] \\ - \frac{\sigma_{nf}}{\sigma_f} \frac{\rho_f}{\rho_{nf}} M^2 [g' - 1] + \frac{\beta_{nf}}{\beta_f} (1-\gamma)\lambda\theta = 0, \end{aligned} \quad (6.23)$$

$$\frac{1}{Pr} \frac{k_{nf}}{k_f} \frac{(\rho C_p)_f}{(\rho C_p)_{nf}} \theta'' - \omega\theta - (1-\gamma)g'\theta + [(1+\gamma)f + (1-\gamma)g]\theta' = 0. \quad (6.24)$$

The boundary conditions in dimensionless form become

$$\left. \begin{aligned} f(0) = 0, f'(0) = 0, g(0) = 0, g'(0) = 0, \theta(0) = 1, \\ f'(z) = 1, g'(z) = 1, \theta(z) = 0 \quad \text{as } z \rightarrow \infty. \end{aligned} \right\} \quad (6.25)$$

The solution can be easily obtained for the other two cases of MHD by the same calculation procedure. Once we get the solutions then the two-dimensional boundary-layer displacement thickness $\delta_{\bar{x}}$ and $\delta_{\bar{y}}$ can be computed from the relation [85]

$$\left. \begin{aligned} \sqrt{\frac{a}{v_f(1-c\bar{t})}} \delta_{\bar{x}} = \int_0^\infty [1 - f'(z)] dz = A, \\ \sqrt{\frac{a}{v_f(1-c\bar{t})}} \delta_{\bar{y}} = \int_0^\infty [1 - g'(z)] dz = B. \end{aligned} \right\} \quad (6.26)$$

We can find the three-dimensional boundary-layer displacement thickness δ_1 at the stagnation point [9], from the following expression

$$\sqrt{\frac{a}{v_f(1-c\bar{t})}} \delta_1 = \frac{(1+\gamma)A + (1-\gamma)B}{2} = C. \quad (6.27)$$

The main quantities of attention are the values of $f''(0)$, $g''(0)$ and $\theta'(0)$ which evaluate the skin friction coefficient in x and y direction and the surface temperature gradient. Our aim

is to see, how the values of $f''(0), g''(0), \theta'(0), A, B$ and C vary in term of the flow parameters? We have taken the fixed Prandtl number ($Pr = 6.2$) in the present computation.

6.3 Results

The boundary value problem given by (6.22-6.25) have been solved numerically using `bvp4c` in MATLAB [20]. We start with the case of forced convection by considering $\lambda = 0$, because of the singularity in Eq. (6.23) at $\gamma = 1$, to find the solutions in the neighborhood of $\gamma = 1$. We have considered water as a base fluid and Cupper (Cu) as a nanoparticle whereas the thermophysical properties of base fluid and nanoparticles are given in Table 1.1-1.2.

6.3.1 Forced convection, $\lambda = 0$

To find the solutions to (6.22-6.25) for $\lambda = 0$, which arise from singularities $\gamma \rightarrow \mp 1$, we consider $\gamma = 1 - \delta$ and look for a solution valid for small δ by writing $g = \delta^{-1}G$. Eqs (6.22-6.23) and (6.25) becomes

$$\begin{aligned} \frac{v_{nf}}{v_f} f'''' + f''[(2 - \delta)f + G] - (2 - \delta)[(f')^2 - 1] - \omega[f' - 1] \\ - \frac{\sigma_{nf} \rho_f}{\sigma_f \rho_{nf}} M^2 [f' - 1] = 0, \end{aligned} \quad (6.28)$$

$$\begin{aligned} \frac{v_{nf}}{v_f} G'''' + G''[(2 + \delta)f + G] - [(G')^2 - \delta] - \omega[G' - \delta] \\ - \frac{\sigma_{nf} \rho_f}{\sigma_f \rho_{nf}} M^2 [G' - \delta] = 0, \end{aligned} \quad (6.29)$$

$$\left. \begin{aligned} f(0) = 0, f'(0) = 0, G(0) = 0, G'(0) = 0, \\ f'(z) = 1, G'(z) = \delta \quad \text{as } z \rightarrow \infty. \end{aligned} \right\} \quad (6.30)$$

Comparing the like powers of δ in Eqs. (6.28) to (6.30), the leading terms f_0 and G_0 satisfying

$$\begin{aligned} \frac{v_{nf}}{v_f} f_0'''' + f_0'' [2f_0 + G_0] - 2[(f_0')^2 - 1] - \omega[f_0' - 1] \\ - \frac{\sigma_{nf}}{\sigma_f} \frac{\rho_f}{\rho_{nf}} M^2 [f_0' - 1] = 0, \end{aligned} \quad (6.31)$$

$$\frac{v_{nf}}{v_f} G_0'''' + G_0'' [2f_0 + G_0] - (G_0')^2 - \omega G_0' - \frac{\sigma_{nf}}{\sigma_f} \frac{\rho_f}{\rho_{nf}} M^2 G_0' = 0, \quad (6.32)$$

$$\left. \begin{aligned} f_0(0) = 0, f_0'(0) = 0, G_0(0) = 0, G_0'(0) = 0, \\ f_0'(z) = 1, G_0'(z) = 0 \quad \text{as } z \rightarrow \infty. \end{aligned} \right\} \quad (6.33)$$

Now suppose $G_0''(0) = -a_0$ for some constant $a_0 > 0$; then we can find $G_0 = a_0 \bar{G}_0$ to obtain

$$\begin{aligned} \frac{v_{nf}}{v_f} f_0'''' + f_0'' [2f_0 + a_0 \bar{G}_0] - 2[(f_0')^2 - 1] - \omega[f_0' - 1] \\ - \frac{\sigma_{nf}}{\sigma_f} \frac{\rho_f}{\rho_{nf}} M^2 [f_0' - 1] = 0, \end{aligned} \quad (6.34)$$

$$\frac{v_{nf}}{v_f} \bar{G}_0'''' + \bar{G}_0'' [2f_0 + a_0 \bar{G}_0] - a_0 (\bar{G}_0')^2 - \omega \bar{G}_0' - \frac{\sigma_{nf}}{\sigma_f} \frac{\rho_f}{\rho_{nf}} M^2 \bar{G}_0' = 0, \quad (6.35)$$

$$\left. \begin{aligned} f_0(0) = 0, f_0'(0) = 0, \bar{G}_0(0) = 0, \bar{G}_0'(0) = 0, \quad \bar{G}_0''(0) = -1, \\ f_0'(z) = 1, \bar{G}_0'(z) = 0 \quad \text{as } z \rightarrow \infty. \end{aligned} \right\} \quad (6.36)$$

The problem given by (6.34)-(6.36) is an eigenvalue problem for a_0 . For $\varphi = \omega = M = 0$, Merkin et. al [21] found that $a_0 = 1.78068$ and $f_0''(0) = 1.66588$. We are interested the solution of Eqs. (6.34) to (6.36) for different φ , ω , and M . Generally, we can write

$$f''(0) = f_0''(0) + \dots, \quad g''(0) = -a_0(1 - \gamma)^{-1} + \dots \quad \text{as } \gamma \rightarrow 1. \quad (6.37)$$

We now exploit the symmetry, given in [19], of $\gamma \rightarrow -\gamma$, $g \rightarrow f$ and $f \rightarrow g$ to extend this analysis to show that there is also singularity as $\gamma \rightarrow -1$. Taking the same procedure, we find

$$f''(0) = -a_0(1 - \gamma)^{-1} + \dots, \quad g''(0) = \bar{G}_0'' + \dots \quad \text{as } \gamma \rightarrow -1. \quad (6.38)$$

To generate further numerical solutions close to $\gamma = \mp 1$ we use the integration of expression in (6.37) and (6.38).

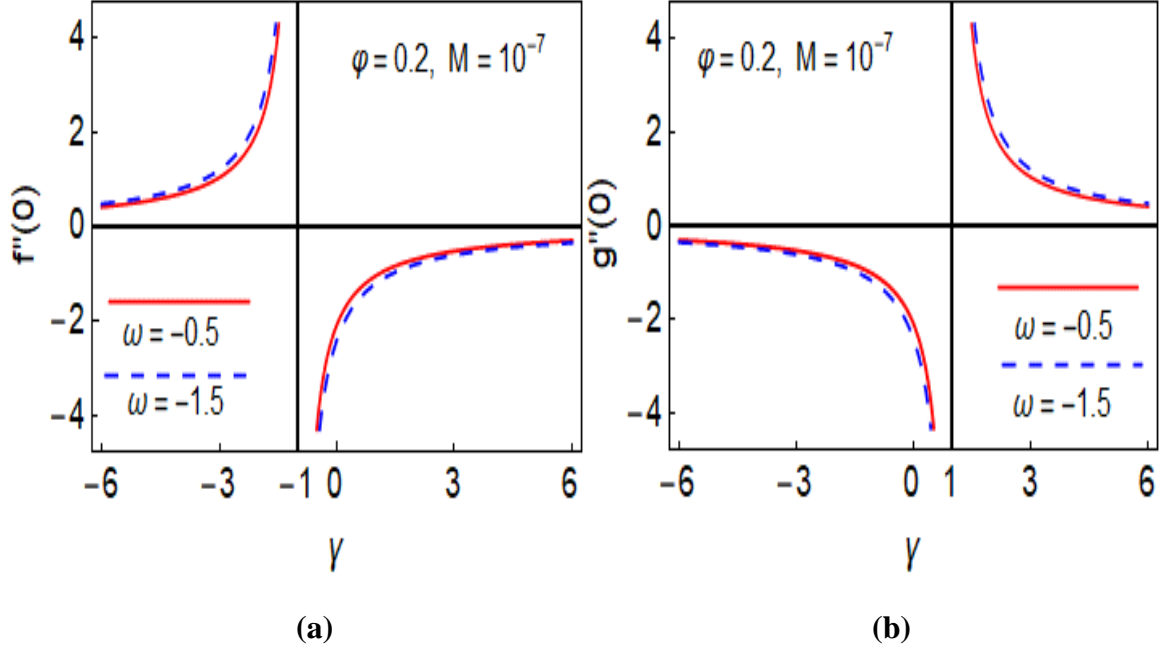


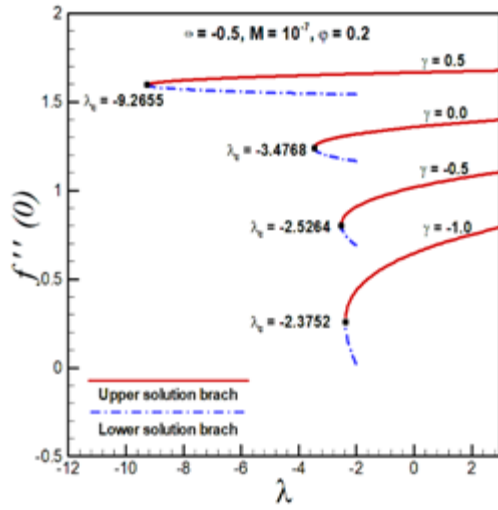
Fig. 6. 1. Forced convection: Plots (a) $f''(0)$ and (b) $g''(0)$ against γ for different ω obtained from the numerical integration of (6.34)-(6.36).

The singular nature of f and g are clearly seen in **Fig 6.1**. The asymptotes of $f''(0)$ and (b) $g''(0)$ against large $|\gamma|$ are in the neighborhoods $(-0.2,0.2)$ when $\omega = -0.5$ and $(-0.3,0.3)$ when $\omega = -1.5$. It is seen that ω influence the solution behavior but there is no longer variation in the solutions against ϕ and M , so we cannot discuss it.

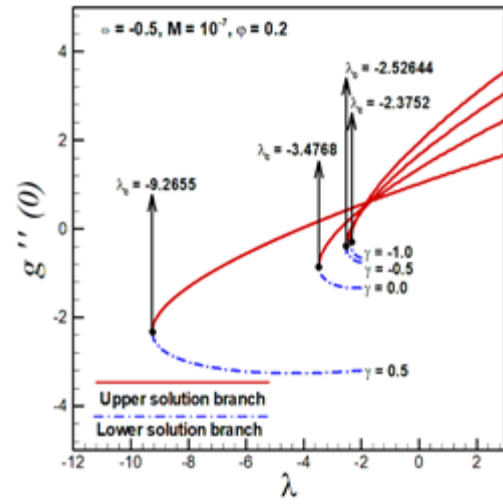
6.3.2 Numerical results

In this section we have discussed the solution to Eqs. (6.22)-(6.25) against different flow parameters for representative values of $\gamma > 1$ and $\gamma < 1$ nothing for $\gamma = 1$ that the solution is independent of λ as discussed in section 6.3.1. The important highlight of these consequences is the existence of critical values λ_c of λ which separate the solution branches by making saddle-node at $\lambda = \lambda_c$. These critical values depend on γ, ϕ, ω and M . The upper branch solutions of $g''(0)$, as seen in **Fig 6.2(b)**, continues to large λ . Also, $f''(0)$ and $-\theta'(0)$ increase for positive λ . It is found that the critical point $|\lambda_c|$ rapidly increase its value when γ enters in the neighbourhood of 1. To increase the value of deceleration the flow physical parameters $f''(0), g''(0)$ and $-\theta'(0)$ show its decreasing behaviour as we expect. The critical values λ_c also depend on the unsteadiness parameter ω and found that the critical point changes from opposing direction ($\lambda < 0$) to assisting direction ($\lambda > 0$) if we increase the rate of deceleration

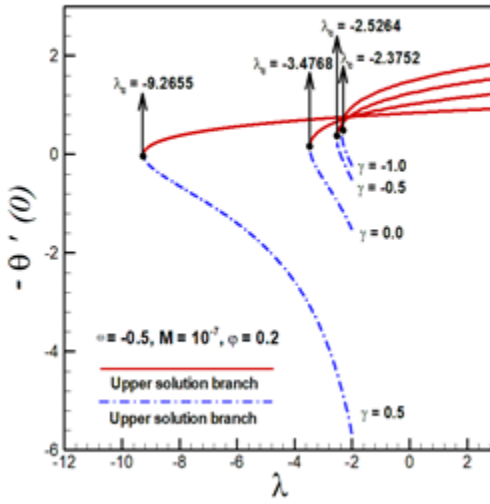
(ω) , as shown in **Fig 6.5**. **Fig 6.7** exhibits the two dimensional displacement thickness A and B and the three dimensional displacement thickness C over the range $-10 \leq \gamma \leq 10$. The thickness A and B are always positive and achieve the maximum values $A = 0.999$ and $B \sim 0.85$ at $\gamma_{mA} \sim -2.47$ and $\gamma_{mB} \sim 4.5$, respectively. Beyond these points it appear that A and B decrease monotonically with increasing $|\gamma|$.



(a)



(b)



(c)

Fig. 6. 2. Plots (a) $f'''(0)$, (b) $g''(0)$ and (c) $-\theta'(0)$ against λ for different γ obtained from the numerical integration of (6.22)-(6.25).

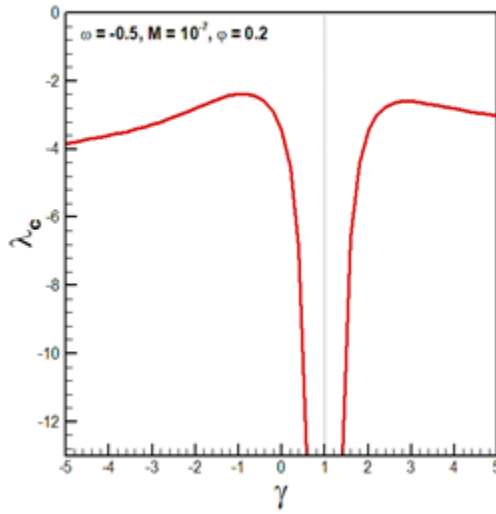
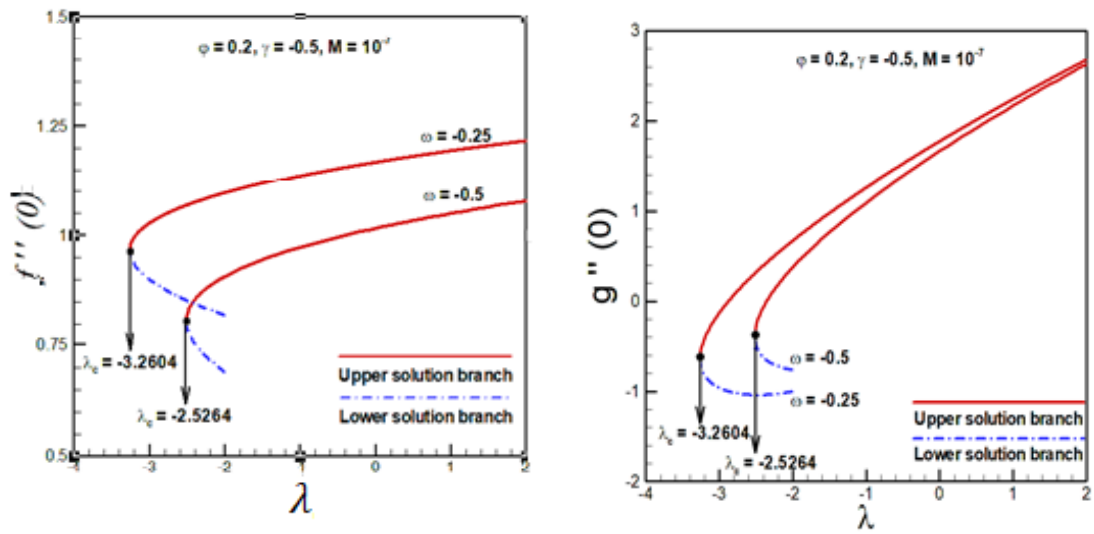
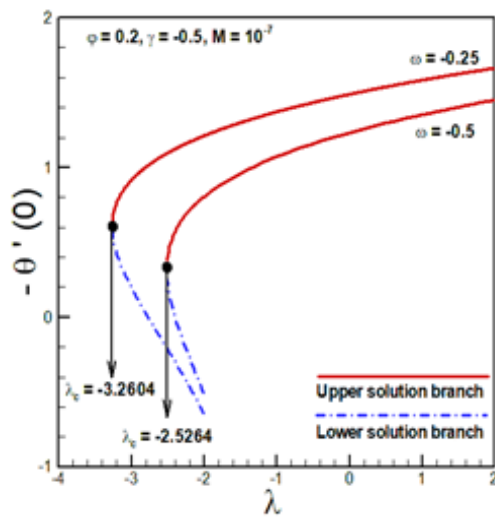


*Fig. 6. 3. Critical values:*a plot of λ_c against γ .



(a)

(b)



(c)

Fig. 6. 4. Plots (a) $f''(0)$, (b) $g''(0)$ and $-\theta'(0)$ against λ for different ω obtained from the numerical integration of (6.22)-(6.25).

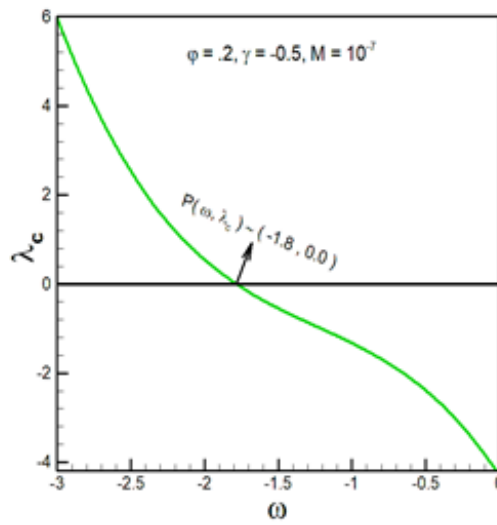


Fig. 6. 5. Critical values: a plot of λ_c against ω .

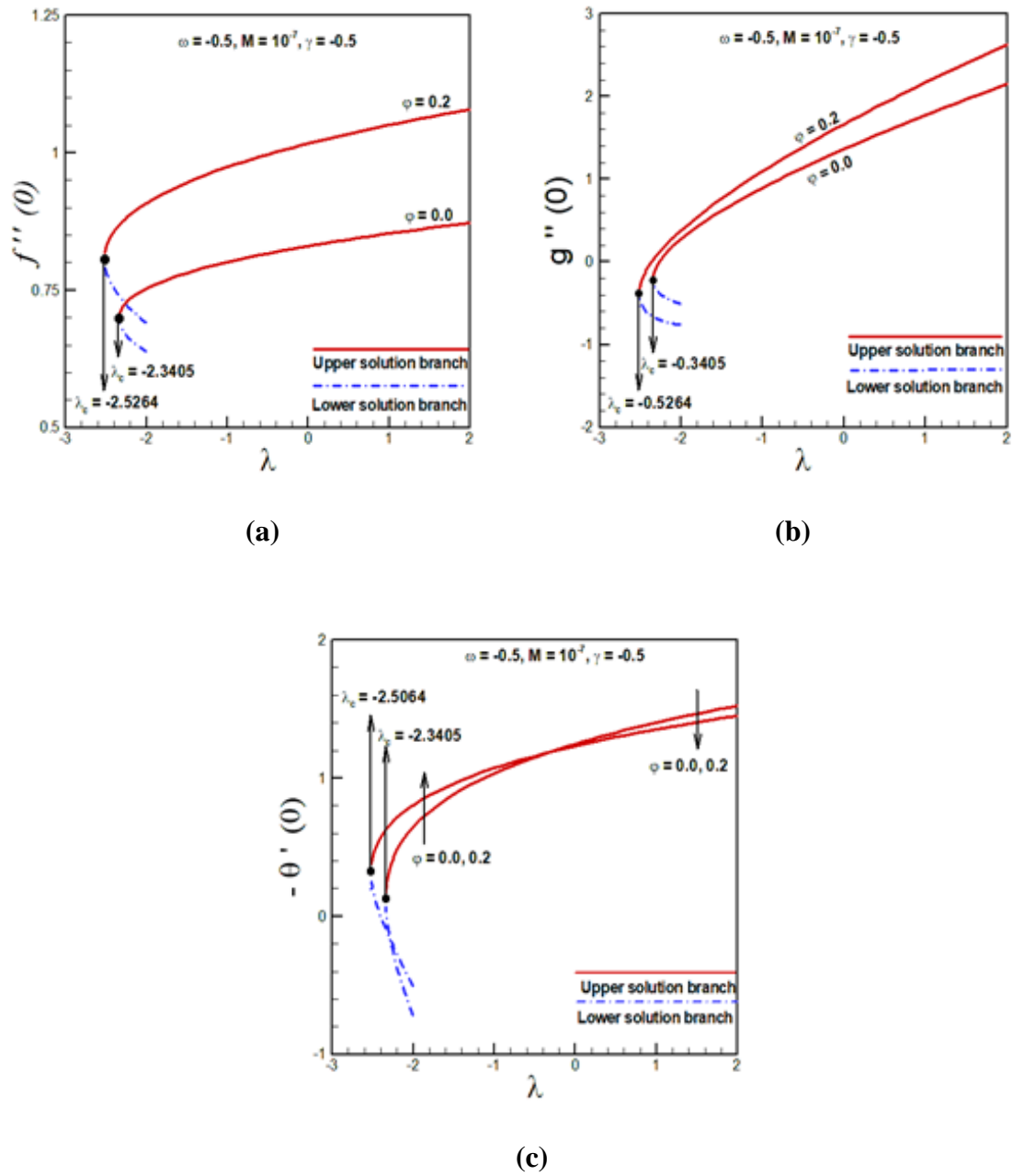


Fig. 6. 6. Plots (a) $f''(0)$, (b) $g''(0)$ and $-\theta'(0)$ against λ for different ϕ obtained from the numerical integration of (6.22)-(6.25).

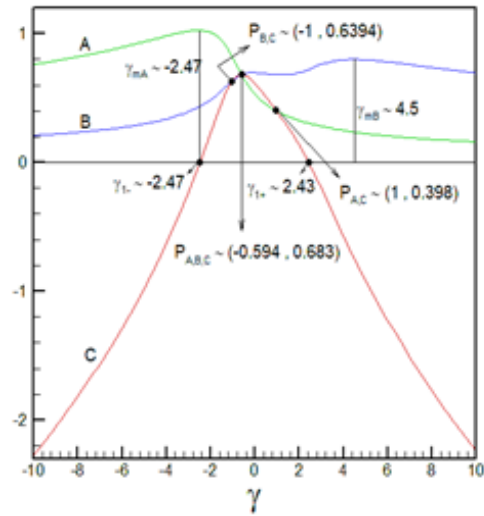


Fig. 6. 7. Variation of the displacement thickness A, B and C with γ when $\varphi = 0.2, \lambda = -2, \omega = -0.5, M = 10^{-7}$, obtained from (6.26)-(6.27).

6.3.3 Free convection limit, λ large

We assume that $\gamma \neq 1$ and to obtain a solution for $\lambda \gg 1$ we put [21]

$$f = \lambda^{1/4}\Phi, \quad g = \lambda^{1/4}\Psi, \quad \eta = \lambda^{1/4}y \quad (6.39)$$

Eqs. (6.22)-(6.25) becomes

$$\begin{aligned} \frac{v_{nf}}{v_f} \Phi'''' + \Phi''[(1+\gamma)\Phi + (1-\gamma)\Psi] - (1+\gamma)[(\Phi')^2 - \lambda^{-1}] \\ - \omega[\lambda^{-1/2}\Phi' - \lambda^{-1}] - \frac{\sigma_{nf} \rho_f}{\sigma_f \rho_{nf}} M^2[\lambda^{-1/2}\Phi' - \lambda^{-1}] = 0 \end{aligned} \quad (6.40)$$

$$\begin{aligned} \frac{v_{nf}}{v_f} \Psi'''' + \Psi''[(1+\gamma)\Phi + (1-\gamma)\Psi] - (1-\gamma)[(\Psi')^2 - \lambda^{-1}] \\ - \omega[\lambda^{-1/2}\Psi' - \lambda^{-1}] - \frac{\sigma_{nf} \rho_f}{\sigma_f \rho_{nf}} M^2[\lambda^{-1/2}\Psi' - \lambda^{-1}] \end{aligned} \quad (6.41)$$

$$+ \frac{\beta_{nf}}{\beta_f} (1-\gamma)\theta = 0$$

$$\frac{1}{Pr} \frac{k_{nf}}{k_f} \frac{(\rho C_p)_f}{(\rho C_p)_{nf}} \theta'' - \omega \lambda^{-1/2} \theta - (1-\gamma)g'\theta + [(1+\gamma)\Phi + (1-\gamma)g]\theta' = 0 \quad (6.42)$$

$$\left. \begin{aligned} \Phi(0) = 0, \Phi'(0) = 0, \Psi(0) = 0, \Psi'(0) = 0, \theta(0) = 1 \\ \Phi'(\eta) = \lambda^{-1/2}, \Psi'(\eta) = \lambda^{-1/2}, \theta(\eta) = 0 \quad \text{as } \eta \rightarrow \infty \end{aligned} \right\} \quad (6.43)$$

where prime denotes differentiation with respect to η .

An expansion in power of $\lambda^{-1/2}$ (see [21]) we obtain the leading order terms

$$\frac{v_{nf}}{v_f} \Phi_0'''' + (1-\gamma)\Psi_0\Phi_0'' = 0, \quad (6.44)$$

$$\frac{v_{nf}}{v_f} \Psi_0'''' + (1-\gamma)\Psi_0\Psi_0'' - (1-\gamma)(\Psi_0')^2 + \frac{\beta_{nf}}{\beta_f} (1-\gamma)\theta = 0, \quad (6.45)$$

$$\frac{1}{Pr} \frac{k_{nf}}{k_f} \frac{(\rho C_p)_f}{(\rho C_p)_{nf}} \theta_0'' - (1-\gamma)\Psi_0'\theta_0 + (1-\gamma)\Psi_0\theta_0' = 0, \quad (6.46)$$

$$\left. \begin{aligned} \Phi_0(0) = 0, \Phi_0'(0) = 0, \Psi_0(0) = 0, \Psi_0'(0) = 0, \theta_0(0) = 1 \\ \Phi_0'(\eta) = 1, \Psi_0'(\eta) = 0, \theta_0(\eta) = 0 \quad \text{as } \eta \rightarrow \infty \end{aligned} \right\} \quad (6.47)$$

Further, we can remove γ from Eqs. (6.44)-(6.48) by writing

$$\Psi_0 = (1 - \gamma)^{-1/2} \bar{\Psi}_0, \quad \bar{\eta} = (1 - \gamma)^{1/2} \eta \quad \text{if } \gamma < 1, \quad (6.48)$$

and

$$\Psi_0 = -(-(1 - \gamma))^{-1/2} \bar{\Psi}_0, \quad \bar{\eta} = (-(1 - \gamma))^{1/2} \eta \quad \text{if } \gamma > 1, \quad (6.49)$$

to obtain

$$\frac{v_{nf}}{v_f} \Phi_0''' + \bar{\Psi}_0 \Phi_0'' = 0, \quad (6.50)$$

$$\frac{v_{nf}}{v_f} \bar{\Psi}_0''' + \bar{\Psi}_0 \bar{\Psi}_0'' - (\bar{\Psi}_0')^2 + \frac{\beta_{nf}}{\beta_f} \theta = 0, \quad (6.51)$$

$$\frac{1}{Pr} \frac{k_{nf}}{k_f} \frac{(\rho C_p)_f}{(\rho C_p)_{nf}} \theta_0'' + \bar{\Psi}_0 \theta_0' - \bar{\Psi}_0' \theta_0 = 0, \quad (6.52)$$

$$\left. \begin{aligned} \Phi_0(0) = 0, \Phi_0'(0) = 0, \bar{\Psi}_0(0) = 0, \bar{\Psi}_0'(0) = 0, \theta_0(0) = 1 \\ \Phi_0'(\eta) = 1, \bar{\Psi}_0'(\eta) = 0, \theta_0(\eta) = 0 \quad \text{as } \eta \rightarrow \infty \end{aligned} \right\} \quad (6.53)$$

here prime denotes differentiation with respect to $\bar{\eta}$.

To find solution for $\gamma < 1$, we set

$$\left. \begin{aligned} f'''(0) = (1 - \gamma)^{\frac{1}{2}} \lambda^{\frac{3}{4}} \Phi_0''(0) + \dots, \quad g''(0) = (1 - \gamma) \lambda^{\frac{1}{4}} \bar{\Psi}_0''(0) + \dots \\ \theta_0'(0) = (1 - \gamma)^{1/2} \lambda^{1/4} \theta_0'(0) + \dots \end{aligned} \right\}, \quad (6.54)$$

and for $\gamma > 1$

$$\left. \begin{aligned} f''(0) = (-(1 - \gamma))^{\frac{1}{2}} \lambda^{\frac{3}{4}} \Phi_0''(0) + \dots, \quad g''(0) = |1 - \gamma| \lambda^{\frac{1}{4}} \bar{\Psi}_0''(0) + \dots \\ \theta_0'(0) = (-(1 - \gamma))^{1/2} \lambda^{1/4} \theta_0'(0) + \dots \end{aligned} \right\}, \quad (6.55)$$

A numerical integration of Eqs. (6.50)-(6.53) gives for $\varphi \in [0, 0.2]$, $\Phi_0''(0) = 0.230955$, $\bar{\Psi}_0''(0) = 0.517641$ and $\theta_0'(0) = 1.024012$ so that, when $\gamma < 1$

$$\left. \begin{aligned} f''(0) &= 0.230955(1-\gamma)^{\frac{1}{2}}\lambda^{\frac{3}{4}} + \dots, & g''(0) &= 0.517641(1-\gamma)\lambda^{\frac{1}{4}} + \dots, \\ \theta_0'(0) &= 1.024012(1-\gamma)^{1/2}\lambda^{1/4} + \dots, \end{aligned} \right\} \quad (6.54a)$$

and when $\gamma > 1$

$$\left. \begin{aligned} f''(0) &= 0.230955(-(1-\gamma))^{\frac{1}{2}}\lambda^{\frac{3}{4}} + \dots, & g''(0) &= 0.517641|1-\gamma|\lambda^{\frac{1}{4}} + \dots \\ \theta_0'(0) &= 1.024012(-(1-\gamma))^{1/2}\lambda^{1/4} + \dots, \end{aligned} \right\} \quad (6.55a)$$

as $\lambda \rightarrow \infty$. These results are consistent with the values seen in **Fig 2**.

6.3.4 Asymptotic for large γ

The asymptotic behavior of solution for $\gamma \gg 1$ is obtained by the change of variables

$$f(y) = \epsilon F(\zeta), \quad g = \epsilon H(\zeta), \quad \zeta = \epsilon^{-1}z \quad (6.56)$$

where $\epsilon = \gamma^{-1/2} \ll 1$. By making use of these transformation, we obtain from (6.22)-(6.25)

$$\begin{aligned} \frac{v_{nf}}{v_f} F''' + F''[(\epsilon^2 + 1)F + (\epsilon^2 - 1)H] - (\epsilon^2 + 1)[(F')^2 - 1] - \omega\epsilon^2[F' - 1] \\ - \frac{\sigma_{nf}}{\sigma_f} \frac{\rho_f}{\rho_{nf}} M^2 \epsilon^2 [F' - 1] = 0 \end{aligned} \quad (6.57)$$

$$\begin{aligned} \frac{v_{nf}}{v_f} H''' + H''[(\epsilon^2 + 1)F + (\epsilon^2 - 1)H] - (\epsilon^2 - 1)[(H')^2 - 1] - \omega\epsilon^2[H' - 1] \\ - \frac{\sigma_{nf}}{\sigma_f} \frac{\rho_f}{\rho_{nf}} M^2 \epsilon^2 [H' - 1] + \frac{\beta_{nf}}{\beta_f} (\epsilon^2 - 1)\lambda\theta = 0 \end{aligned} \quad (6.58)$$

$$\frac{1}{Pr} \frac{k_{nf}}{k_f} \frac{(\rho C_p)_f}{(\rho C_p)_{nf}} \theta'' - \omega\epsilon^2\theta - (\epsilon^2 - 1)H'\theta + [(\epsilon^2 + 1)F + (\epsilon^2 - 1)H]\theta' = 0 \quad (6.59)$$

$$\left. \begin{aligned} F(0) = 0, F'(0) = 0, H(0) = 0, H'(0) = 0, \theta(0) = 1 \\ F'(\zeta) = 1, H'(\zeta) = 1, \theta(\zeta) = 0 \quad \text{as } \zeta \rightarrow \infty \end{aligned} \right\} \quad (6.60)$$

where prime denotes differentiation with respect to ζ . Positing the regular perturbation expansion (see [21]), we get the lowest order system

$$\frac{v_{nf}}{v_f} F_0''' + F_0'' F_0 - (F_0')^2 + 1 - F_0'' H_0 = 0, \quad (6.61)$$

$$\frac{v_{nf}}{v_f} H_0''' - H_0'' H_0 + (H_0')^2 - 1 + H_0'' F_0 - \frac{\beta_{nf}}{\beta_f} \lambda \theta = 0, \quad (6.62)$$

$$\frac{1}{Pr} \frac{k_{nf}}{k_f} \frac{(\rho C_p)_f}{(\rho C_p)_{nf}} \theta_0'' - H_0 \theta_0' + H_0' \theta_0 + F_0 \theta_0' = 0, \quad (6.63)$$

$$\left. \begin{aligned} F_0(0) = 0, F_0'(0) = 0, H_0(0) = 0, H_0'(0) = 0, \theta_0(0) = 1 \\ F_0'(\zeta) = 1, H_0'(\zeta) = 1, \theta_0(\zeta) = 0 \quad \text{as } \zeta \rightarrow \infty \end{aligned} \right\} \quad (6.64)$$

This furnishes the large γ leading behavior for the shear stress parameters

$$\left. \begin{aligned} f''(0) \sim \gamma^{\frac{1}{2}} F_0''(0) + \dots, \quad g''(0) \sim \gamma^{\frac{1}{2}} H_0''(0) + \dots, \\ \theta_0'(0) \sim \gamma^{\frac{1}{2}} \theta_0'(0) + \dots \end{aligned} \right\} \quad (6.65)$$

and found that

Table. 6. 1. Numerical values of physical parameters obtained from Eqs. (6.61)-(6.64) when $\varphi = 0.2$

λ	$F_0''(0)$	$H_0''(0)$	$-\theta_0'(0)$
2.0	1.546306	-1.39591	1.289627
1.5	1.540641	-1.21789	1.248234
1.0	1.534529	-1.03243	1.201338
0	1.52027	-0.62871	1.06969
-1.0	1.470081	0.267444	0.140489
-1.5	1.465408	0.454667	0.353976
-2.0	1.464168	0.592279	0.521576

Also, for λ -large we can apply transformation (6.39) in Eqs. (6.61)-(6.64) to obtain Eqs. (6.50)-(6.53) at leading order, giving in the limit of large γ and λ ,

$$\left. \begin{aligned} f''(0) = 0.230955 \gamma^{\frac{1}{2}} \lambda^{\frac{3}{4}} + \dots, \quad g''(0) = 0.517641 \gamma^{\frac{1}{2}} \lambda^{\frac{1}{4}} + \dots, \\ \theta_0'(0) = 1.024012 \gamma^{\frac{1}{2}} \lambda^{1/4} + \dots, \end{aligned} \right\} \quad (6.66)$$

And for displacement thickness one finds

$$\left. \begin{aligned} A &\sim \gamma^{\frac{1}{2}} A_0 \\ B &\sim \gamma^{\frac{1}{2}} B_0 \\ C &\sim \frac{(1+\gamma)A_0 + (1-\gamma)B_0}{2\gamma^{\frac{1}{2}}} \end{aligned} \right\}. \quad (6.67)$$

where A_0 and B_0 should be find by solving Eqs. (6.61)-(6.64) and defined as,

$$\left. \begin{aligned} \int_0^\infty [1 - f'(\zeta)] d\zeta &= A_0 \\ \int_0^\infty [1 - g'(\zeta)] d\zeta &= B_0 \end{aligned} \right\}. \quad (6.68)$$

Thus when $\gamma \rightarrow \infty$, then the shear stress parameter grows without bound and the displacement thickness A and B tends to zero. Also, the leading behavior for C tends to negative infinity as $\gamma \rightarrow \infty$ as

$$C \sim -\frac{1}{2}(B_0 - A_0)\gamma^{\frac{1}{2}}. \quad (6.69)$$

6.4 Conclusion

A theoretical study of unsteady non-axisymmetric Homann stagnation point flow of nanofluids has been analyzed under the assumption of buoyancy forces and external magnetic field. The corresponding flow equations are reduced to a system of nonlinear coupled ordinary differential equations which contain the flow parameters, the nanoparticles volume fraction φ , the unsteadiness parameter ω , the buoyancy parameter λ , Hartmann number M , Prandtl number Pr and shear-to-strain ratio γ (represents the strength of the potential flow of inviscid fluid). Since the reduce system of ODE's contain a singularity at $\gamma = \mp 1$, so first we treated the case of forced convection flow by taking $\lambda = 0$ and get the numerical results by using `bvp4c` scheme in MATLAB. The numerical results are obtained for the physical parameters $f''(0)$, $g''(0)$ and $-\theta'(0)$ against different values of flow parameters. Finally, we use the perturbation to see the behavior of flow for large values of buoyancy parameter λ and for large strength of potential flow γ . From this study we get the following remarks:

1. Dual solution exists for the opposing flow.
2. In free convection flow, the singular nature of f and g at $\gamma = \mp 1$ is observed for all values of unsteadiness parameter ω while the impact of nanoparticle volume fraction φ and Hartmann number M are negligible.
3. The critical values λ_c of λ depends upon φ , γ , ω and M .
4. The critical point $|\lambda_c|$ rapidly increase its value when γ enters in the neighborhood of 1.
5. The nanoparticle volume fraction φ increase the range of λ for which the solution exist.

6. Againsts the unsteadiness parameter ω , the critical points λ_c changes from opposing ($\lambda < 0$) to assisnting flow ($\lambda > 0$).
7. The boundary layer thickness A and B are always positive and achieve its maximum values $A = 0.99$ at $\gamma \sim - 2.47$ and $B = 0.85$ at $\gamma \sim - 4.5$.
8. The three-dimensional boundary layer thickness C intersect the boundary layers A and B at approximately $\gamma \sim - 0.594$ and also at that point, C attain its maximum value.
9. The impacts of nanoparticle volume fraction φ , Hartmann number M and unsteadiness parameter ω are negligible in the solution of free convection limit (λ large) and large asymptotic behavior of γ .

7 Bibliography

1. Brimmo, A. T., & Qasaimeh, M. A. (2017). Stagnation point flows in analytical chemistry and life sciences. *RSC Advances*, 7(81), 51206-51232.
2. Hiemenz, K. (1911). Die Grenzschicht an einem in den gleichformigen Flussigkeitsstrom eingetauchten geraden Kreiszyylinder. *Dinglers Polytech. J.*, 326, 321-324.
3. Howarth, L. (1934). On the calculation of steady flow in the boundary layer near the surface of a cylinder in a stream (No. ARC-R/M-1632). AERONAUTICAL RESEARCH COUNCIL LONDON (UNITED KINGDOM).
4. Homann, F. (1936). Einfluß großer Zähigkeit bei Strömung um Zylinder. *Forschung auf dem Gebiet des Ingenieurwesens A*, 7(1), 1-10.
5. Howarth, L. (1951). CXLIV. The boundary layer in three dimensional flow.—Part II. The flow near a stagnation point. *The London, Edinburgh, and Dublin Philosophical Magazine and Journal of Science*, 42(335), 1433-1440.
6. Howarth, L. (1951). XXV. The boundary layer in three dimensional flow.—Part I. Derivation of the equations for flow along a general curved surface. *The London, Edinburgh, and Dublin Philosophical Magazine and Journal of Science*, 42(326), 239-243.
7. Rott, N. (1956). Unsteady viscous flow in the vicinity of a stagnation point. *Quarterly of Applied Mathematics*, 13(4), 444-451.
8. JT Stuart. (1959). The viscous flow near a stagnation point when the external flow has uniform vorticity. *Journal of the Aerospace Sciences*, 26(2), 124-125.
9. Davey, A. (1961). Boundary-layer flow at a saddle point of attachment. *Journal of Fluid Mechanics*, 10(4), 593-610.
10. Rosenhead, L. (Ed.). (1963). *Laminar boundary layers: an account of the development, structure, and stability of laminar boundary layers in incompressible fluids, together with a description of the associated experimental techniques.* Clarendon Press.
11. Davey, A., & Schofield, D. (1967). Three-dimensional flow near a two-dimensional stagnation point. *Journal of Fluid Mechanics*, 28(1), 149-151.

12. Libby, P. A. (1967). Heat and mass transfer at a general three-dimensional stagnation point. *AIAA Journal*, 5(3), 507-517.
13. Schofield, D., & Davey, A. (1967). Dual solutions of the boundary-layer equations at a point of attachment. *Journal of Fluid Mechanics*, 30(4), 809-811.
14. Libby, P. A. (1976). Laminar flow at a three-dimensional stagnation point with large rates of injection. *AIAA Journal*, 14(9), 1273-1279.
15. Matunobu, Y. O. (1977). Structure of pulsatile Hiemenz flow and temporal variation of wall shear stress near the stagnation point. I. *Journal of the Physical Society of Japan*, 42(6), 2041-2049.
16. Matunobu, Y. O. (1977). Structure of pulsatile Hiemenz flow and temporal variation of wall shear stress near the stagnation point. II. *Journal of the Physical Society of Japan*, 43(1), 326-329.
17. Tamada, K. (1979). Two-dimensional stagnation-point flow impinging obliquely on a plane wall. *Journal of the Physical Society of Japan*, 46(1), 310-311.
18. Dorrepaal, J. M. (1986). An exact solution of the Navier-Stokes equation which describes non-orthogonal stagnation-point flow in two dimensions. *Journal of Fluid Mechanics*, 163, 141-147.
19. Weidman, P. D. (2012). Non-axisymmetric Homann stagnation-point flows. *Journal of Fluid Mechanics*, 702, 460-469.
20. Borrelli, A., Giancesio, G., Patria, M. C., Roşca, N. C., Roşca, A. V., & Pop, I. (2017). Buoyancy effects on the 3D MHD stagnation-point flow of a Newtonian fluid. *Communications in Nonlinear Science and Numerical Simulation*, 43, 1-13.
21. Lok, Y. Y., Merkin, J. H., & Pop, I. (2017). Mixed convection non-axisymmetric Homann stagnation-point flow. *Journal of Fluid Mechanics*, 812, 418-434.
22. Merkin, J. H., Najib, N., Bachok, N., Ishak, A., & Pop, I. (2017). Stagnation-point flow and heat transfer over an exponentially stretching/shrinking cylinder. *Journal of the Taiwan Institute of Chemical Engineers*, 74, 65-72.
23. Weidman, P. D., & Ma, Y. P. (2016). The competing effects of wall transpiration and stretching on Homann stagnation-point flow. *European Journal of Mechanics-B/Fluids*, 60, 237-241.

24. Nandy, S. K., Mahapatra, T. R., & Pop, I. (2015). Unsteady separated stagnation-point flow over a moving porous plate in the presence of a variable magnetic field. *European Journal of Mechanics-B/Fluids*, 53, 229-240.
25. Mehmood, R., Nadeem, S., & Akbar, N. S. (2013). Non-orthogonal stagnation point flow of a micropolar second grade fluid towards a stretching surface with heat transfer. *Journal of the Taiwan Institute of Chemical Engineers*, 44(4), 586-595.
26. Weidman, P. (2017). Impinging rotational stagnation-point flows. *International Journal of Non-Linear Mechanics*, 88, 97-101.
27. Giantesio, G. (2013). MHD stagnation-point flow (Doctoral dissertation, Università degli Studi di Ferrara).
28. Hewitt, R. E., Duck, P. W., & Stow, S. R. (2002). Continua of states in boundary-layer flows. *Journal of Fluid Mechanics*, 468, 121-152.
29. Ziabakhsh, Z., Domairry, G., & Ghazizadeh, H. R. (2009). Analytical solution of the stagnation-point flow in a porous medium by using the homotopy analysis method. *Journal of the Taiwan Institute of Chemical Engineers*, 40(1), 91-97.
30. Weidman, P. D. (2012). Obliquely-intersecting Hiemenz flows: a new interpretation of Howarth stagnation-point flows. *Fluid Dynamics Research*, 44(6), 065509.
31. Khan, I., Saeed, K., & Khan, I. (2017). Nanoparticles: Properties, applications and toxicities. *Arabian Journal of Chemistry*.
32. Choi, S. U., & Eastman, J. A. (1995). Enhancing thermal conductivity of fluids with nanoparticles (No. ANL/MSD/CP--84938; CONF-951135--29). Argonne National Lab., IL (United States).
33. Masuda, H., Ebata, A., & Teramae, K. (1993). Alteration of thermal conductivity and viscosity of liquid by dispersing ultra-fine particles. Dispersion of Al₂O₃, SiO₂ and TiO₂ ultra-fine particles.
34. Buongiorno, J. (2006). Convective transport in nanofluids. *Journal of heat transfer*, 128(3), 240-250.
35. Hussain, S. T., Nadeem, S., & Haq, R. U. (2014). Model-based analysis of micropolar nanofluid flow over a stretching surface. *The European Physical Journal Plus*, 129(8), 161.

36. Timofeeva, E. V., Routbort, J. L., & Singh, D. (2009). Particle shape effects on thermophysical properties of alumina nanofluids. *Journal of Applied Physics*, 106(1), 014304.
37. Vajravelu, K., Prasad, K. V., Lee, J., Lee, C., Pop, I., & Van Gorder, R. A. (2011). Convective heat transfer in the flow of viscous Ag–water and Cu–water nanofluids over a stretching surface. *International Journal of Thermal Sciences*, 50(5), 843-851.
38. Ramzan, M., Bilal, M., & Chung, J. D. (2017). Radiative flow of Powell-Eyring magneto-nanofluid over a stretching cylinder with chemical reaction and double stratification near a stagnation point. *PloS one*, 12(1), e0170790.
39. Haq, R. U., Nadeem, S., Khan, Z. H., & Noor, N. F. M. (2015). Convective heat transfer in MHD slip flow over a stretching surface in the presence of carbon nanotubes. *Physica B: condensed matter*, 457, 40-47.
40. Hussain, S. T., Khan, Z. H., & Nadeem, S. (2016). Water driven flow of carbon nanotubes in a rotating channel. *Journal of Molecular Liquids*, 214, 136-144.
41. Kardri, M. A., Bachok, N., Arifin, N. M., & Ali, F. M. (2017, January). Boundary layer flow and heat transfer over a stretching cylinder in a copper-water nanofluid. In *AIP Conference Proceedings* (Vol. 1795, No. 1, p. 020012). AIP Publishing.
42. Rashad, A. M., Ismael, M. A., Chamkha, A. J., & Mansour, M. A. (2016). MHD mixed convection of localized heat source/sink in a nanofluid-filled lid-driven square cavity with partial slip. *Journal of the Taiwan Institute of Chemical Engineers*, 68, 173-186.
43. Hassan, M. I., Alzarooni, I. A., & Shatilla, Y. (2017). Heat pipe long term performance using water based nanofluid. *Cogent Engineering*, 4(1), 1336070.
44. Xuan, Y., & Li, Q. (2003). Investigation on convective heat transfer and flow features of nanofluids. *Journal of Heat transfer*, 125(1), 151-155.
45. Akbar, N. S., Khan, Z. H., & Nadeem, S. (2014). The combined effects of slip and convective boundary conditions on stagnation-point flow of CNT suspended nanofluid over a stretching sheet. *Journal of Molecular Liquids*, 196, 21-25.

46. Falana, A., Ojewale, O. A., & Adeboje, T. B. (2016). Effect of Brownian motion and thermophoresis on a nonlinearly stretching permeable sheet in a nanofluid. *Advances in Nanoparticles*, 5(01), 123.
47. Khan, W. A., & Pop, I. (2010). Boundary-layer flow of a nanofluid past a stretching sheet. *International journal of heat and mass transfer*, 53(11-12), 2477-2483.
48. Hayat, T., & Nadeem, S. (2017). Heat transfer enhancement with Ag–CuO/water hybrid nanofluid. *Results in Physics*, 7, 2317-2324.
49. Hassani, M., Tabar, M. M., Nematı, H., Domairry, G., & Noori, F. (2011). An analytical solution for boundary layer flow of a nanofluid past a stretching sheet. *International Journal of Thermal Sciences*, 50(11), 2256-2263.
50. Ibrahim, W., Shankar, B., & Nandeppanavar, M. M. (2013). MHD stagnation point flow and heat transfer due to nanofluid towards a stretching sheet. *International Journal of Heat and Mass Transfer*, 56(1-2), 1-9.
51. Nadeem, S., & Lee, C. (2012). Boundary layer flow of nanofluid over an exponentially stretching surface. *Nanoscale Research Letters*, 7(1), 94.
52. Rana, P., & Bhargava, R. (2012). Flow and heat transfer of a nanofluid over a nonlinearly stretching sheet: a numerical study. *Communications in Nonlinear Science and Numerical Simulation*, 17(1), 212-226.
53. Haq, R. U., Nadeem, S., Akbar, N. S., & Khan, Z. H. (2015). Buoyancy and radiation effect on stagnation point flow of micropolar nanofluid along a vertically convective stretching surface. *IEEE Transactions on Nanotechnology*, 14(1), 42-50.
54. Saleh, S. H. M., Arifin, N. M., Nazar, R., & Pop, I. (2017). Unsteady Micropolar Fluid over a Permeable Curved Stretching Shrinking Surface. *Mathematical Problems in Engineering*, 2017.
55. Pop, I., Mohamed Isa, S. S. P., Arifin, N. M., Nazar, R., Bachok, N., & Ali, F. M. (2016). Unsteady viscous MHD flow over a permeable curved stretching/shrinking sheet. *International Journal of Numerical Methods for Heat & Fluid Flow*, 26(8), 2370-2392.
56. Arifin, N. M., Isa, S. S. P. M., Nazar, R., Bachok, N., Ali, F. M., & Pop, I. (2015). UNSTEADY BOUNDARY LAYER FLOW OVER A PERMEABLE CURVED

STRETCHING/SHRINKING SURFACE. In ICHMT DIGITAL LIBRARY ONLINE. Begel House Inc..

57. Roşca, N. C., & Pop, I. (2015). Unsteady boundary layer flow over a permeable curved stretching/shrinking surface. *European Journal of Mechanics-B/Fluids*, 51, 61-67.
58. Maxwell, J. C. (1881). *A treatise on electricity and magnetism* (Vol. 1). Clarendon press.
59. Hamilton, R. L., & Crosser, O. K. (1962). Thermal conductivity of heterogeneous two-component systems. *Industrial & Engineering chemistry fundamentals*, 1(3), 187-191.
60. Yamada, E., & Ota, T. (1980). Effective thermal conductivity of dispersed materials. *Effektive Wärmeleitfähigkeit in dispersen Systemen. Wärme-und Stoffübertragung*, 13(1-2), 27-37.
61. Zhang, X., Gu, H., & Fujii, M. (2007). Effective thermal conductivity and thermal diffusivity of nanofluids containing spherical and cylindrical nanoparticles. *Experimental Thermal and Fluid Science*, 31(6), 593-599.
62. Xue, Q. Z. (2005). Model for thermal conductivity of carbon nanotube-based composites. *Physica B: Condensed Matter*, 368(1-4), 302-307.
63. Ellahi, R., Hassan, M., & Zeeshan, A. (2016). Aggregation effects on water base Al₂O₃—nanofluid over permeable wedge in mixed convection. *Asia-Pacific Journal of Chemical Engineering*, 11(2), 179-186.
64. Esfahani, J. A., Akbarzadeh, M., Rashidi, S., Rosen, M. A., & Ellahi, R. (2017). Influences of wavy wall and nanoparticles on entropy generation over heat exchanger plat. *International Journal of Heat and Mass Transfer*, 109, 1162-1171.
65. Atlas, M., Haq, R. U., & Mekkaoui, T. (2016). Active and zero flux of nanoparticles between a squeezing channel with thermal radiation effects. *Journal of Molecular Liquids*, 223, 289-298.
66. Labropulu, F., & Chinichian, M. (2004). Unsteady oscillatory stagnation-point flow of a viscoelastic fluid. *International journal of engineering science*, 42(7), 625-633.

67. Takemitsu, N., & Yaso, O. M. (1979). Unsteady stagnation-point flow impinging obliquely on an oscillating flat plate. *Journal of the Physical Society of Japan*, 47(4), 1347-1353.
68. Liao, S. (2003). *Beyond perturbation: introduction to the homotopy analysis method*. CRC press.
69. Ariel, P. D. (1994). Hiemenz flow in hydromagnetics. *Acta Mechanica*, 103(1-4), 31-43.
70. Grosan, T., Pop, I., Revnic, C., & Ingham, D. B. (2009). Magnetohydrodynamic oblique stagnation-point flow. *Meccanica*, 44(5), 565.
71. Javed, T., Ghaffari, A., & Ahmad, H. (2015). Numerical study of unsteady MHD oblique stagnation point flow with heat transfer over an oscillating flat plate. *Canadian Journal of Physics*, 93(10), 1138-1143.
72. Mutuku-Njane, W. N. (2014). *Analysis of hydromagnetic boundary layer flow and heat transfer of nanofluids* (Doctoral dissertation, Cape Peninsula University of Technology).
73. Borrelli, A., Giantesio, G., & Patria, M. C. (2012). MHD oblique stagnation-point flow of a Newtonian fluid. *Zeitschrift für angewandte Mathematik und Physik*, 63(2), 271-294.
74. Jena, S. K., & Mathur, M. N. (1981). Similarity solutions for laminar free convection flow of a thermomicro-polar fluid past a non-isothermal vertical flat plate. *International Journal of Engineering Science*, 19(11), 1431-1439.
75. Guram, G. S., & Smith, A. C. (1980). Stagnation flows of micropolar fluids with strong and weak interactions. *Computers & Mathematics with Applications*, 6(2), 213-233.
76. Rup, K., & Drózdź, A. (2013). The effect of reduced heat transfer in a micropolar fluid in natural convection. *Archives of Thermodynamics*, 34(3), 45-59.
77. Mohammadein, A. A., & Subba Reddy Gorla, R. (2001). Heat transfer in a micropolar fluid over a stretching sheet with viscous dissipation and internal heat generation. *International Journal of Numerical Methods for Heat & Fluid Flow*, 11(1), 50-58.

78. Mehmood, R., Nadeem, S., & Masood, S. (2016). Effects of transverse magnetic field on a rotating micropolar fluid between parallel plates with heat transfer. *Journal of Magnetism and Magnetic Materials*, 401, 1006-1014.
79. Khan, A. U., Nadeem, S., & Hussain, S. T. (2016). Phase flow study of MHD nanofluid with slip effects on oscillatory oblique stagnation point flow in view of inclined magnetic field. *Journal of Molecular Liquids*, 224, 1210-1219.
80. Yu, W., & Choi, S. U. S. (2003). The role of interfacial layers in the enhanced thermal conductivity of nanofluids: a renovated Maxwell model. *Journal of Nanoparticle Research*, 5(1-2), 167-171.
81. Jiang, H., Xu, Q., Huang, C., & Shi, L. (2015). The role of interfacial nanolayer in the enhanced thermal conductivity of carbon nanotube-based nanofluids. *Applied Physics A*, 118(1), 197-205.
82. Mukhopadhyay, S., & Andersson, H. I. (2009). Effects of slip and heat transfer analysis of flow over an unsteady stretching surface. *Heat and Mass Transfer*, 45(11), 1447-1452.
83. Roşca, A. V., & Pop, I. (2013). Flow and heat transfer over a vertical permeable stretching/shrinking sheet with a second order slip. *International Journal of Heat and Mass Transfer*, 60, 355-364.
84. Nazar, R., Jaradat, M., Arifin, N., & Pop, I. (2011). Stagnation-point flow past a shrinking sheet in a nanofluid. *Open Physics*, 9(5), 1195-1202.
85. Mutuku-Njane, W. N. (2014). Analysis of hydromagnetic boundary layer flow and heat transfer of nanofluids (Doctoral dissertation, Cape Peninsula University of Technology).